# Numerical Experimentation and Analysis of Quantum Turbulence in Superfluid Helium II

Lucy Kathleen Sherwin-Robson

Thesis submitted for the degree of
Doctor of Philosophy


*School of Mathematics & Statistics*
*Newcastle University*
*Newcastle upon Tyne*
*United Kingdom*

October 2016

*I'd like to dedicate this thesis to my Dad, Keith 'Joe Beans' Sherwin.*
*I'm so grateful for all his help and support during the composing of this work, and I forgive his falling asleep on more than one occasion during the endless proof readings.*

*All my Love.*

**Acknowledgements**

I would like to thank my supervisors Carlo Barenghi and Andrew Baggaley for leading me so skilfully in to the mind boggling world of quantum turbulence and helping me explore there before leading me safely out in to the world of classical physics to carry on the rest of my life with my cherished PhD. Thank you so much guys!

**Abstract**

The study of turbulence in superfluid Helium II suggests that at least in part the rules of classical turbulence are obeyed. The question posed is, whether the tangles of quantised vorticity that represent turbulence in a superfluid are directly analogous to the swirls and eddies found in turbulent classical fluids. A cornerstone of classical turbulence has been the evidence of the Kolmogorov scaling and this has been observed in some experimental studies of superfluid turbulence. Here we contrast quantum turbulence in various scenarios to further our understanding and confidence in such modelling as well as to search for evidence of any adherence to Kolmogorov.

In all numerical simulations presented here turbulence in the superfluid is driven by motions of the normal fluid. My work approaches the superfluid turbulence through three distinct normal fluid models. In most physical experiments with superfluid helium, turbulence is generated in two ways. Firstly, thermally (by applying a heat flux, as in thermal counterflow) and we model this by using a uniform normal fluid. Secondly, mechanically (by stirring the liquid) and we model this in one of two ways; either a synthetic turbulence using a kinematic simulations (KS) flow or with a frozen snapshot from a direct numerical simulation (DNS).

We determine the difference between thermally and mechanically driven quantum turbulence. Using the kinematic simulations model we find that in the latter the energy is concentrated at the large scales, the spectrum obeys Kolmogorov scaling, vortex lines have small curvature, and the presence of coherent vortex structures induces vortex reconnections at small angles. In contrast, when we employ our uniform normal fluid we find the energy is concentrated at the mesoscales, the curvature is larger, the vorticity field is featureless and reconnections occur at larger angles. Our results suggest a method to experimentally detect the presence of superfluid vortex bundles.

We show that vortex tangles with the same vortex line density have different energy spectra, depending on the driving normal fluid, and identify the spectral signature of two forms of superfluid turbulence: Kolmogorov tangles and Vinen tangles. By decomposing the superfluid velocity field into local and nonlocal contributions, we find that in Vinen tangles the motion of vortex lines depends mainly on the local curvature, whereas in Kolmogorov tangles the long-range vortex interaction is dominant and leads to the formation of clustering of lines, in analogy to the 'worms' of classical turbulence.

Finally, we compute the frequency spectrum of superfluid vortex density fluctuations for tangles of the same vortex line density, but which are driven by two different normal fluid models. Taking our measurements in a sufficiently small cube to eliminate any filtering effect, we observe the $f^{-5/3}$ that has been experimentally observed within the Kolmogorov tangles whereas for the Vinen tangles we find a flat and featureless spectrum.

# Contents

# List of Figures

# List of Tables

# Chapter 1

# Introduction

## 1.1 Classical Turbulence

A Formula 1 car built with a supreme understanding of combustion engine technology and the fullest appreciation of how to make the stickiest rubber tyres would be completely ineffective without a fundamental understanding of turbulence. In our world virtually everything that moves creates turbulence. Some systems are designed to overcome turbulence, some to harness turbulence, but an understanding of turbulence is key to much of man's interaction with his home planet. What allows a Formula 1 car to travel at speeds up to 230 mph and yet not take to the skies like a plane is the designers exploitation of turbulent flows.

With the advent of satellite imaging we can now observe large scale turbulent flows such as those generated by hurricanes and note perhaps their similarity to the flow of water disappearing out of the sink. The range of scales for these turbulent events is huge and the forces acting within them range from barely enough to move a bubble to large enough to bring down a building. How could we predict the movement of a hurricane and protect ourselves from it, how could we use the force of moving water to deliver us power? These questions are addressed daily by engineers, mathematicians and physicists.

Even at the cutting edge of research and design with turbulent flows, the understanding is far from complete and in spite of the significant resources spent on the matter each year only the tiniest advances are made. The basic law defining turbulent flows - the Navier-Stokes Equation, the basis of which was first formulated in 1845 [Navier, 1822; Stokes, 1845] - is well understood but the wind tunnel and not the computer still reigns supreme.

From the early pictorial representations of turbulent flows such as those famously depicted by Leonardo da Vinci (dated between 1508 and 1513), right through to the present time, we consider turbulence as a set of swirls of varying sizes, the larger appearing to propagate the smaller. We term these elements 'eddies' or 'vortices'. Turbulent flows are typically chaotic in nature and lacking any form of symmetry. The velocity field within a turbulent flow can vary greatly in both time and space creating a very unpredictable system.

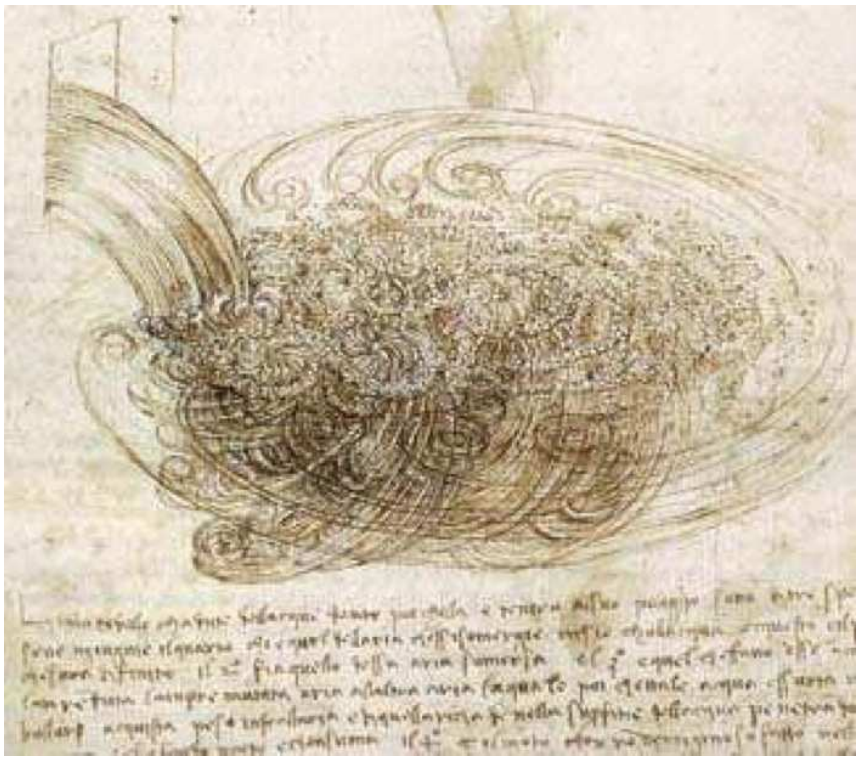

Figure 1.1: Leonardo da Vinci's sketch of turbulence. Image taken from [Frisch, 1995]

Within such a complex system we are able to create models based on a concept of a mean flow with an additional fluctuating component - this is known as the Reynolds decomposition (more on this on page 8). Modelling in this way allows the emergence of near-universal statistical characteristics, whereby we can begin to describe flows in terms of these averaged properties. Within fully developed turbulence (found in everyday life) there is a broad spectrum of eddy sizes and timescales for these eddies to either break down or dissipate. It is this combination of massive length scales and widely varying time scales, which means numerical simulations of realistic and useful flows are, to all intents and purposes, impossible with the current computing power available, and indeed any computing power likely to be coming available in the near future.

In 1922 L. F. Richardson [Richardson, 1922] adapted The Siphonaptera nursery rhyme to produce:

*"Big whirls have little whirls;*
*That feed on their velocity;*
*And little whirls have lesser whirls;*
*And so on to viscosity"*

This poem nicely describes what is known as the Richardson Cascade in turbulence. This is where instabilities within the flow give rise to the creation of large eddies which then dissipate their energy into the creation of smaller eddies. Hence we have a 'cascade' of energy through the eddies from large to small scales. It is the inertial forces, and not viscosity, that are responsible for the cascade until the point where the eddies are reduced to a size where their Reynolds number (the ratio of the magnitudes of inertial force (per unit mass) and viscous force (per unit mass)) is of order unity. At this point viscosity drives the cascade to extinction and it is at this scale that all the kinetic energy of the system is dissipated as heat.

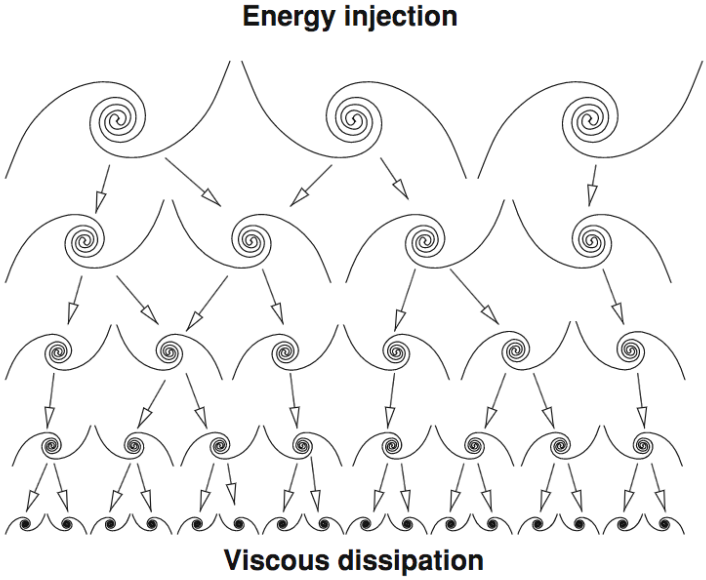


Figure 1.2: Visualisation of Richardson's cascade. Image taken from [Nazarenko, 2011]

Feynman asserted that 'turbulence is the most important unsolved problem of classical physics' [Feynman *et al.*, 1964], and there are a great many reasons why it remains

unsolved. Along with those already highlighted, we encounter yet more problems when we try to define what an 'eddie' actually is, and how it breaks down.

In trying to understand and model turbulence we are forced to deal with the Navier-Stokes equation. Strictly speaking this equation describes the behaviour of all incompressible flows ($\nabla \cdot \mathbf{v} = 0$). For dealing with laminar flows within a pipe it is quite the useful tool, however when dealing with turbulent flows it presents quite the obstacle. If we look at the equation itself

$$\rho \left[ \frac{\partial \mathbf{v}}{\partial t} + (\mathbf{v} \cdot \nabla)\mathbf{v} \right] = -\nabla P + \mu \nabla^2 \mathbf{v} + \mathbf{F}, \tag{1.1}$$

where $\rho$ is the fluid density, $\mathbf{v}$ is the velocity vector, $P$ is the fluid pressure, $\mu$ is the viscosity of the fluid (a measure of the relative difficulty of displacing the fluid by an external force), and $\mathbf{F}$ is the 'body force' an example of which could be gravity. It is the nonlinearity of this equation that makes both the analytic process and the numerical modelling of it so complex and computationally expensive.

In observing the decay of a turbulent system it is this same nonlinear element of the Navier-Stokes that drives the flow through ever smaller scales. If we consider the following 1D velocity field $v = \sin(kx)$ and examine the effect of putting this through the nonlinearity (also in 1D) we find:

$$\begin{aligned} v\frac{\partial v}{\partial x} &= \sin(kx)\frac{\partial}{\partial x}(\sin(kx)) && (1.2)\\ &= \sin(kx)k\cos(kx) && (1.3)\\ &= \frac{k}{2}\sin(2kx). && (1.4) \end{aligned}$$

So clearly this nonlinearity has taken in a flow of one scale and produced a flow half the size since $\sin(2kx)$ varies over length scales half the size of $\sin(kx)$.

We have already discussed how turbulence within a flow manifests itself on a wide range of scales. If we now seek to give these scales some form of mathematical definition we note the following categories; the *'Energy containing eddies'* (or *'Injection range'*) contain the largest eddies within our flow and the typical scale of these eddies $L$ is referred to as the integral scale; most of the energy within the flow is contained here. Next we have the *'Universal equilibrium range'* where the motions of the flow are independent of the motions of the large scale flow, then we have the *'Inertial subrange'* which contains a range of scales away from both the largest and smallest scales where viscous effects are of

little importance. Finally we have the *'Dissipation Range'* which holds the smallest eddies within our flow and it is here where viscous effects take hold and dissipate our energy, the typical scale of eddies within this grouping $\eta$ is known as the Kolmogorov microscale.

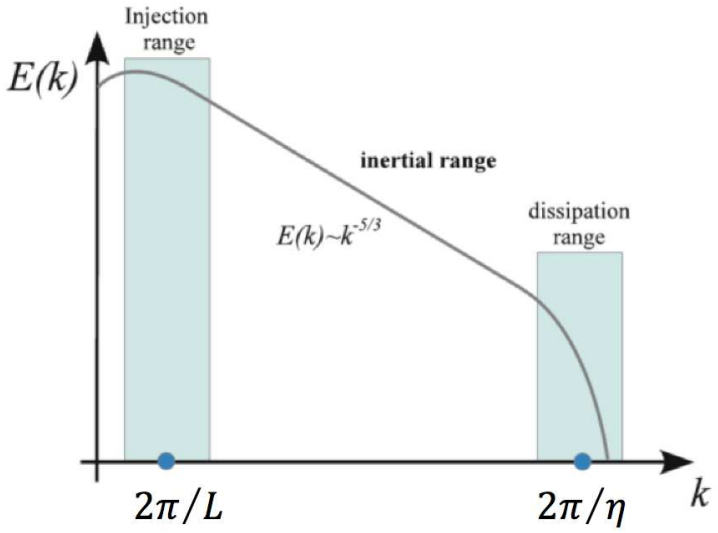


Figure 1.3: Visualisation of the scales within a turbulent flow and their energy containment[1]. Image adapted from [Gnedin *et al.*, 2015]

In order to gain a clearer understanding of the consequences of the Navier-Stokes Equation, we need to know a little more about the concept of the Reynolds number. We have already noted that it is the ratio of the magnitudes of inertial force (per unit mass) and viscous force (per unit mass) but we have not yet given it mathematical meaning. If we say that $U$ is a typical velocity within the flow and that the integral scale $L$ is the characteristic length scale of the flow we can then say that the order of the magnitude of the inertial force $(\mathbf{v} \cdot \nabla)\mathbf{v}$ is $U^2/L$ and the order of magnitude of the viscous force $\nu\nabla^2\mathbf{v}$ is $\nu U/L^2$. Therefore the ratio of the two quantities is $(U^2/L)/(\nu U/L^2)$ which gives us the Reynolds number as:

$$\mathrm{Re} = \frac{UL}{\nu}. \tag{1.5}$$

It is worth noting that experiments indicate that eddies of this scale will 'break-up' on a timescale of the order $\tau = L/U$. We can now introduce the Reynolds number in to the Navier-Stokes equation by using the following dimensionless variables (using the background pressure $P_0$)

[1]For clarity it should be noted that we use wavenumbers $k$ as another way to describe length scales $r$. They are related by $k = 2\pi/r$.

$$\mathbf{x}' = \frac{\mathbf{x}}{L} \ , \ \mathbf{v}' = \frac{\mathbf{v}}{U} \ , \ t' = \frac{tU}{L} \ , \ P' = \frac{P - P_0}{\rho U^2}, \tag{1.6}$$

and substituting them in to the Navier-Stokes equation (Eqn. 1.1) to obtain:

$$\rho \left[ \frac{\partial \mathbf{v}}{\partial t} + (\mathbf{v} \cdot \nabla)\mathbf{v} \right] = -\nabla P + \frac{1}{\mathrm{Re}} \nabla^2 \mathbf{v}. \tag{1.7}$$

This is the dimensionless Navier-Stokes equation (note we have dropped the primes from the new variables which feature in this equation and we neglect any body forces). From this it can be understood that the Reynolds number is a key determinant on the magnitude of the viscous term within the equation.

As mentioned earlier, the Navier-Stokes equation does have solutions and indeed in 1941 Kolmogorov derived one of the limited number of 'exact' results [Kolmogorov, 1941], however in order to achieve this he allowed himself the assumption of a homogeneous and isotropic flow which means the flow has no preferred direction of motion nor does it differ from one area to the next. Following the approach of Frisch [Frisch, 1995] we use dimensional analysis to derive the results.

Kolmogorov's $1^{st}$ similarity hypothesis was that the statistical properties of the small scale motions, $\eta$ within the flow are uniquely determined by the energy dissipation, $\epsilon$ and the viscosity of the fluid, $\nu$.

$$\eta \backsim \nu^{\alpha} \epsilon^{\beta}. \tag{1.8}$$

The dimensions of these quantities in SI units are $[\eta] = \mathrm{m}$, $[\nu] = \mathrm{m}^2/\mathrm{s}$, and $[\epsilon] = \mathrm{m}^2/\mathrm{s}^3$. Thus dimensional analysis yields:

$$\mathrm{m} = \left( \frac{\mathrm{m}^2}{\mathrm{s}} \right)^{\alpha} \left( \frac{\mathrm{m}^2}{\mathrm{s}^3} \right)^{\beta} \Rightarrow 1 = 2\alpha + 2\beta, \tag{1.9}$$

$$0 = -\alpha - 3\beta. \tag{1.10}$$

This gives us $\alpha = 3/4$ and $\beta = -1/4$ and we obtain our first scaling law:

$$\eta \backsim \left( \frac{\nu^3}{\epsilon} \right)^{1/4}. \tag{1.11}$$

We now turn our attention to the large scale motions of the flow. We note firstly that the kinetic energy density is defined to be $(1/2)\rho|\mathbf{v}|^2$, and secondly (from earlier) that the typical decay timescale of these motions is of order $L/U$. From these we can therefore say

that the rate of loss of kinetic energy within our flow is $\backsim U^2/(L/U) = U^3/L$. This loss of kinetic energy is what drives the cascade and so the rate of flow of energy into the cascade is given by $U^3/L$. Therefore in statistically steady turbulence - where the rate of flow of energy in to the cascade is balanced by the rate at which viscosity dissipates energy - we can define the rate of viscous energy dissipation as:

$$\epsilon \backsim \frac{U^3}{L}. \tag{1.12}$$

Taking these together we can form a relation between the largest and smallest scale motions of our flow:-

$$\eta \backsim \left(\frac{\nu^3}{\epsilon}\right)^{1/4} = \left(\frac{\nu^3}{U^3/L}\right)^{1/4} = \left(\frac{L^4\nu^3}{U^3L^3}\right)^{1/4} = L\left(\frac{\nu}{UL}\right)^{3/4} = L(\mathrm{Re})^{-3/4}. \tag{1.13}$$

We now move on to Kolmogorov's $2^{nd}$ similarity hypothesis in which he asserts that within the inertial subrange of the flow, where viscosity is irrelevant, only the length scale $\ell$ under consideration (where $\ell = 2\pi/k$ and $k$ is the wavenumber) and the rate of energy dissipation, $\epsilon$ determine the statistical properties at a given scale.

A highly significant statistical property of turbulence is the energy spectrum. We recall that the kinetic energy density is defined as $(1/2)\rho|\mathbf{v}|^2$, using this we define the energy spectrum $E(k)$ which is the total energy per unit mass contained at each scale $2\pi/k$, per logarithmic interval of $k$ as:

$$\int_0^\infty E(k)dk = \frac{1}{2}\langle \mathbf{v}^2 \rangle, \tag{1.14}$$

where the angular brackets represent an averaging of the velocity. The dimension of the wavenumber $k$ is $[1/m]$ and hence the dimension of the energy spectrum is:

$$[E(k)] = \frac{m^2/s^2}{1/m} = \frac{m^3}{s^2}. \tag{1.15}$$

Now from Kolmogorov's $2^{nd}$ similarity hypothesis we are able to state

$$E(k) \backsim \epsilon^\delta k^\gamma. \tag{1.16}$$

Once again deploying dimensional analysis, we derive:

$$\frac{m^3}{s^2} = \left(\frac{m^2}{s^3}\right)^{\delta}\left(\frac{1}{m}\right)^{\gamma} \Rightarrow 3 = 2\delta - \gamma \tag{1.17}$$

$$2 = 3\delta, \tag{1.18}$$

which gives us $\delta = 2/3$ and $\gamma = -5/3$, thus we have obtained what is arguably Kolmogorov's most famous scaling law:

$$E(k) = C\epsilon^{2/3}k^{-5/3}, \tag{1.19}$$

where $C$ is known as the Kolmogorov constant which is expected to be of order unity. This equation and its implications are a cornerstone of the work in this thesis and will be referred to multiple times throughout.

Although the foregoing mathematics is not and was not intended as a thorough testing and analysis of Navier-Stokes and Kolmogorov's work in this area it does leave us with a clear understanding of some of the complexities faced by mathematicians working in the field of classical turbulence. The last of the issues with the Navier-Stokes Equation that we will address is the 'closure problem'. Put simply, whenever we seek to analytically solve our governing equations, we have by definition more variables to solve for than we have equations to solve them with. We can demonstrate this principle by deploying the Reynolds decomposition within the Navier-Stokes equation in order to obtain the Reynolds equation. In the Reynolds decomposition we can decompose the velocity in to a mean and fluctuating component, such that:-

$$\mathbf{v} = \bar{\mathbf{v}} + \mathbf{v}', \tag{1.20}$$

where $\bar{\mathbf{v}}$ is the mean component and $\mathbf{v}'$ is the fluctuating component. We can likewise decompose both the body force and the pressure of a flow. Writing the Navier-Stokes equation out in suffix notation we have:

$$\rho\left[\frac{\partial v_i}{\partial t} + v_j\frac{\partial v_i}{\partial x_j}\right] = -\frac{\partial P}{\partial x_i} + \rho\nu\nabla^2 v_i + F_i. \tag{1.21}$$

If we now apply the Reynolds decomposition to this equation we obtain:

$$\rho\frac{\partial}{\partial t}(\bar{v_i} + v_i') + \rho(\bar{v_j} + v_j')\frac{\partial}{\partial x_j}(\bar{v_i} + v_i') = -\frac{\partial}{\partial x_i}(\bar{P} + P') + \rho\nu\nabla^2(\bar{v_i} + v_i') + \bar{F_i}. \tag{1.22}$$

By averaging this equation we effect the removal of several terms and ultimately we derive:

$$\rho\frac{\partial}{\partial t}\bar{v_i} + \rho\bar{v_j}\frac{\partial}{\partial x_j}\bar{v_i} + \rho\left\langle v_j'\frac{\partial}{\partial x_j}v_i'\right\rangle = -\frac{\partial}{\partial x_i}\bar{P} + \rho\nu\nabla^2\bar{v_i} + \bar{F_i}. \tag{1.23}$$

This is comparable to the Navier-Stokes equation for the mean flow but has the additional term $\rho\langle v_j'\partial/\partial x_j(v_i')\rangle$ representing the effect of the turbulent fluctuations on the mean flow. We can rewrite this term as:-

$$\rho\left\langle v_j'\frac{\partial}{\partial x_j}v_i'\right\rangle = \frac{\partial}{\partial x_j}\langle\rho v_i'v_j'\rangle, \tag{1.24}$$

where $-\langle\rho v_i'v_j'\rangle$ is defined as the Reynolds Stress. Substituting this back in to equation 1.24 and rearranging gives us:

$$\rho\frac{\partial}{\partial t}\bar{v_i} + \rho\bar{v_j}\frac{\partial}{\partial x_j}\bar{v_i} = -\frac{\partial}{\partial x_j}\langle\rho v_i'v_j'\rangle - \frac{\partial\bar{P}}{\partial x_i} + \rho\nu\nabla^2\bar{v_i} + \bar{F_i}. \tag{1.25}$$

This is the Reynolds equation, and if the Reynolds stress is known the equation can be solved to find the mean flow. However, if the Reynolds stress is not known and we attempt to evolve the equation numerically we find that,

$$\frac{\partial}{\partial t}(-\langle\rho v_i'v_j'\rangle) \text{ depends upon } \langle\rho v_i'v_j'v_k'\rangle, \tag{1.26}$$

and similarly,

$$\frac{\partial}{\partial t}(-\langle\rho v_i'v_j'v_k'\rangle) \text{ depends upon } \langle\rho v_i'v_j'v_k'v_l'\rangle. \tag{1.27}$$

Each request of the Reynolds equation to produce a solution simply results in the production of another problem, and this persists no matter how many iterations we proceed through and Navier-Stokes has no mechanism for overcoming this closure problem. A great deal of effort has been concentrated on this issue but if progress is to be made then we need extra assumptions that can be reasonably made to allow us to model the closure.

Whilst the Naiver-Stokes Equation is adequate and sufficient for us to describe and understand classical turbulence, there is a liquid environment where the laws of quantum mechanics govern all motion, and not classical physics. At temperatures approaching absolute zero, helium is a liquid that flows without large scale eddies and where energy is not dissipated through viscosity. In modelling this 'superfluid' world we preclude the difficulties of Navier-Stokes and instead take advantage of the peculiar nature of vorticity, although even without the need to solve Navier-Stokes, the world of quantum turbulence is still proving slow to give up its secrets.

Perhaps the most profound effect demonstrated by a superfluid is that vorticity in the

system is constrained to lie on 'vortex filaments' (more of which in section 1.2), and it is around these that the flow circulates. Another notable contrast to classical turbulence is that instead of having eddies of varying strength and size, in a superfluid all the vortices have the exact same strength and core structure (size). Classical fluids are always subject to viscosity and any motion that is induced in the fluid will be dampened to extinction by this viscosity. Superfluids by contrast, are not subject to viscosity and receive no damping effect through this mechanism.

In a non-viscous world, what concept do we have for turbulence? Well, we have our filaments which can be induced to move and in doing so they interact to form vortex tangles. These 'tangles' can be steady chaotic systems which in some cases do exhibit some of the near-universal properties of classical turbulence [Skrbek & Sreenivasan, 2012; Vinen & Niemela, 2002].

The question is; will a deeper understanding of the turbulence found in our 'superfluid' (known as Quantum Turbulence) provide a better understanding of the classical turbulence we are subject to everyday?

## 1.2 From helium I to helium II

We start our counting of time from notable dates: The big bang, the birth of Christ, but for low temperature physicists perhaps counting from 10th July 1908 would be equally valid. At 5.45am on this date, having spent the previous 3 years accumulating sufficient stocks of helium gas, Heike Kamerlingh Onnes (1853 - 1926) and his team at The University of Leiden in Holland started the cooling process designed to liquefy helium for the first time ever.

Onnes had founded his Cryogenics Laboratory in 1904, inviting fellow researchers to join him in the quest to liquefy helium. Onnes was keen to share his efforts with others in the field, this was in contrast perhaps to the approach of James Dewar, who was another key figure in the efforts to liquefy the permanent gases and a long term rival of Onnes. Dewar was known for hiding key parts of his apparatus when presenting his public lectures to the Royal Institute and it is some irony that it was indeed the eponymous Dewar flask[2] that was the key piece of apparatus used by Onnes in his iterative Joule-Thomson cooling

[2]The Dewar flask is a twin walled glass vessel with the inner space evacuated which allows a liquid contained within it to dissipate very little heat through the walls. Dewar sued Thermos for stealing his design and although the court and Thermos acknowledged it was indeed Dewar's invention, his failure to patent this meant he forfeit the right to benefit from its exploitation.

system[3] that finally succeeded in producing liquid helium.

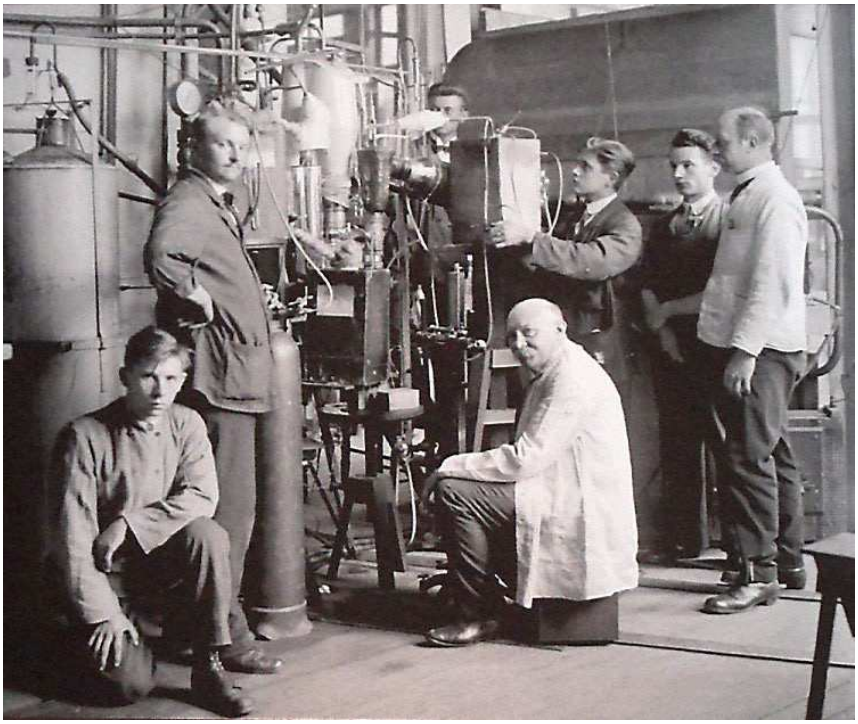

Figure 1.4: Onnes and his blue boys. Image taken from [Bellows, 2014]

Dewar's quest to liquefy the 'final' permanent gas, which began in 1878 was ultimately to be undermined by a seemingly unrelated event which had occurred ten years earlier. In 1868, there had been a total solar eclipse which was observed by, amongst others, Pierre-Jules-Csar Janssen. His examination of the sun's spectrum during the eclipse lead to the discovery of the signature for a new element. On reviewing Janssen's findings, Sir Norman Lockyer concluded that the line on the absorption spectrum representing 587.49 nanometers in wavelength was proof of an element forming part of the sun but not known to exist on earth. Lockyer named this element helium, after the Greek sun god 'Helios'.

In 1895, helium was discovered to exist on Earth by Sir William Ramsay, and so by the time Dewar succeeded in his quest to liquefy hydrogen in 1898, it was no longer the final permanent gas and the recognition he had hoped for was severely blunted. It was to be Onnes whose work in this field was recognised with the award of a Nobel Prize for Physics in 1913 ( *"for his investigations on the properties of matter at low temperatures*

[3]The Joule-Thomson cooling process is one whereby the principles underlying the first law of thermodynamics are employed to provide cooling through the adiabatic expansion of the pre-cooled target gas.

*which led, inter alia, to the production of liquid helium"*).

Onnes' success in 1908 was the end of a long race to liquefy all the permanent gases, a race which spanned almost a century and began with Michael Faraday (1791-1867) in 1823 when he achieved the liquefaction of chlorine [Faraday, 1823]. Although Onnes' triumph marked the end of liquefying permanent gases, it was only the beginning for the study into liquid helium and its bizarre properties ...

It became apparent that the observed properties of this liquid were at odds with any single physical state. In much the same way as scientists had grappled with light exhibiting in some instances properties of particle physics and in others that of a waveform, early theorists had to find an explanation for why this new liquid could sometimes appear to behave as a classical fluid and at others as what we now know as a superfluid.

Liquid helium can exist in two states, helium I and helium II, and the phase diagram on the left of figure 1.5 below attempts to visualise this concept. The area shaded yellow is helium I, a classical fluid, and the area shaded blue is helium II, a superfluid. For comparison, the right of figure 1.5 shows a typical solid-liquid-gas phase diagram where we can see a point (labelled the 'triple point') where all three forms could exist in equilibrium. There is no such corresponding point for helium.

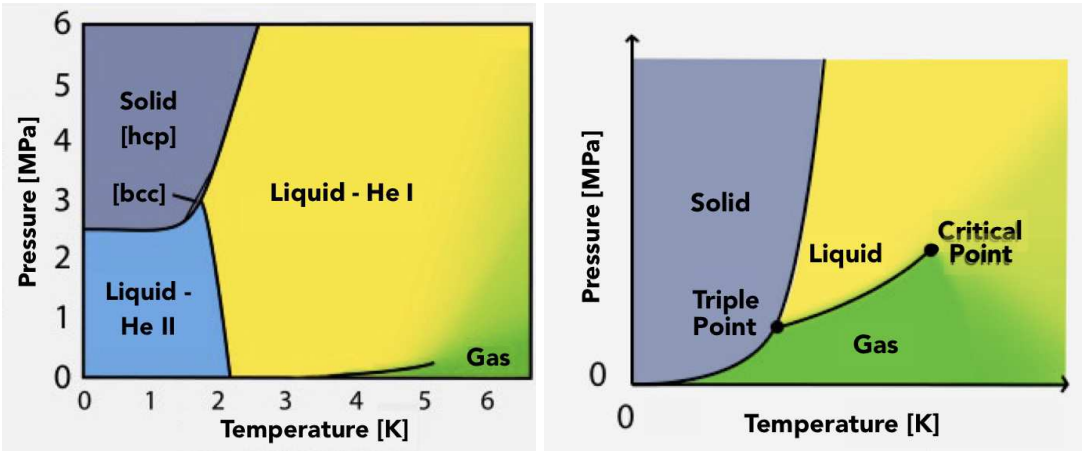


Figure 1.5: Helium phase diagram on the left and a regular solid-liquid-gas phase diagram on the right[4].

[4]Images adapted from http://www.learner.org/courses/physics/unit/text.html?unit=8&secNum=3 and accessed in August 2015.

If the temperature of liquid helium I is reduced, at a temperature of around 2.17 K[5] it undergoes a quite amazing transformation. At this critical temperature, its specific heat undergoes a most unexpected increase which falls away asymmetrically as the cooling passes down through this point. The liquid above 2.17 K is referred to as helium I and the liquid beneath 2.17 K is referred to as helium II.

Helium I is cooled to low temperatures (down to 1 K) by evaporation. This evaporation is achieved by reducing the pressure above the liquid by means of a vacuum pump and the latent heat of vaporisation of the liquid helium effectively cools the remaining liquid. Given the very low specific heat of helium I, a large percentage of the liquid's volume needs to be evaporated to produce a significant cooling. Indeed to take the temperature from 4K down to the lambda point requires the evaporation of one third of the initial volume. Following helium's phase transformation at the lambda point, the new liquid has some astonishing properties; for example the thermal conductivity of 'superfluid' helium II is of the order of 1,000,000 times greater than that of helium I and even 100 times greater than copper or silver.

In 1938 Tisza [Tisza, 1938] suggested that helium II was best represented as a degenerate Bose-Einstein gas (BEC) whereby the fluid exists in two fluid fractions, one a classical fluid and the other a superfluid, where the atoms exist in their 'ground' state (lowest energy level). This concept was also noted by Lev Landau [Landau, 1941] who ultimately came up with his own two fluid model which was not based on any notion of a BEC, for which he was to receive a Nobel Prize in 1962. The two fluid components are coupled by a mutual friction [Donnelly, 1991], the proportions of which alter with temperature (as shown in figure 1.6), and as we approach absolute zero the superfluid component tends to dominate the mix. These two fluid components have markedly different properties and behaviours.

The superfluid component is entirely inviscid which can be demonstrated experimentally by lifting a container full of helium II out of a surrounding larger mass using a vessel with a microporous ceramic base. This container will normally hold liquid helium without leakage through the base, this being inhibited by the viscosity of the fluid. Once past the transition point the now superfluid helium II will pass through this ceramic base in a clear demonstration of a superflow.

The superfluid component has another intriguing characteristic, which is that it has zero entropy. This too can be demonstrated experimentally by immersing one end of a

[5]This temperature is known as the critical temperature or lambda point.

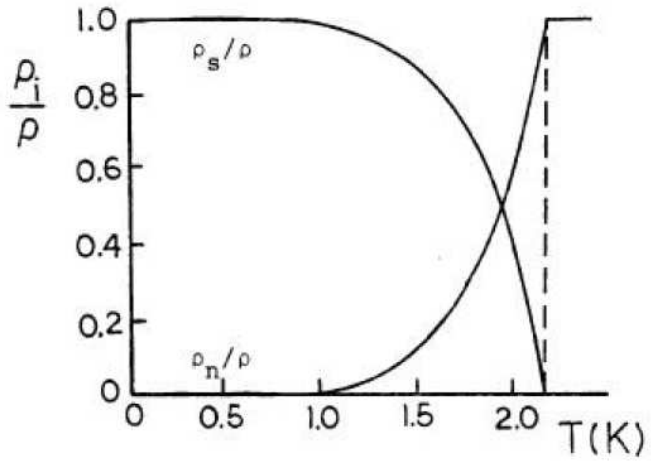


Figure 1.6: Composition of helium II, where $\rho_s$ is the density of the superfluid component, $\rho_n$ is the density of the normal fluid component and $\rho$ is the total fluid density i.e. $\rho = \rho_s + \rho_n$. Image taken from [Codoluto & Dykhoff, 2014]

specially designed double open ended tube into helium II. The end in the helium has been formed into a bulb packed with just about the finest material known to man - jeweller's rouge - held in place with cotton bungs above and below. The interstitial spaces between this medium are such that no viscous fluid could pass through and any flow through it must thereby be a superflow. When this bulb is warmed by an external light source falling upon it, a flow is induced from the helium II through the rouge into the free space above (subject only to the saturated vapour pressure of helium II). The flow of helium through this bulb is one from a colder region to a warmer region. This appears to be in defiance of the second law of thermodynamics. The flow cannot be a thermal flow, and cannot involve the transfer of heat energy. This effect, known as the fountain effect, demonstrates that the superfluid component of helium II has zero entropy.

## 1.3 Quantised vortices

A final intriguing attribute of the superfluid component of helium II is the quantisation of the circulation. The circulation $\Gamma$ is given by:-

$$\Gamma = \oint \mathbf{v}_s \cdot \mathrm{d}\ell, \tag{1.28}$$

where $\mathbf{v}_s$ is the superfluid velocity. The superfluid component of He II represents a condensate where all the particles occupy the lowest energy level i.e. are in the ground state. This

condensate's wavefunction $\Psi$ can be given by $\Psi(\mathbf{r},t) = R(\mathbf{r},t)\mathrm{e}^{iS(\mathbf{r},t)}$ under the Madelung transform, where $R(\mathbf{r},t)$ and $S(\mathbf{r},t)$ represent the amplitude and phase distributions respectively. If we now consider following a closed path $C$, the integrated change in the phase will be:

$$\Delta S = \oint_C \nabla S \cdot \mathrm{d}\ell. \tag{1.29}$$

As we are following a closed path, the end point is the same as the starting point and since that the wavefunction must be single-valued, it follows that,

$$\Delta S = 2\pi q, \tag{1.30}$$

where $q$ is an integer. Where $q \neq 0$ this means that there must be a phase defect within our region, whereby the phase can take any value from 0 to $2\pi$. In order that there should be no such phase singularity the density, $\rho_s$, on this line will need to be zero. Such lines are therefore quantised vortices. Noting that the phase distribution defines the fluids velocity through the following equation,

$$\mathbf{v}_s = (\hbar/m)\nabla S, \tag{1.31}$$

where $\hbar$ is Planck's constant and $m$ is the mass of a helium atom. If we combine this with Equation 1.28 we can say that the circulation about $C$ is given by,

$$\Gamma = \oint \mathbf{v}_s \cdot \mathrm{d}\ell = q\left(\frac{h}{m}\right). \tag{1.32}$$

Which is to say that the circulation is quantised by the ratio of Plank's constant over the mass of a helium atom which is known as the quantum of circulation and denoted $\kappa$.

From Equation 1.31 it follows that the superfluid flow is irrotational, and from this you could conclude that there is no vorticity within the superfluid. However, Equation 1.32 allows for non-zero circulation. For both of these statements to be satisfied, we need a hollow region close to the singularity with nothing inside it such that the superfluid density is zero. By assuming this, the superfluid velocity is undefined within the core and incompressibility can still be satisfied outside this core region. Hence we are left with hollow-core vortices where the circulation of the fluid is constrained to lie on thin lines of fixed core size $a_0$ (approximately 1 Angstrom in diameter) and circulation.

This phenomenon was first predicted by Onsager in 1948 [Onsager, 1948] and then further developed by Feynman in 1955 [Feynman, 1955*b*] and it was first observed experimentally in 1961 by Vinen [Vinen, 1961]. Developments in experimental techniques

have lead to the visualisation of vortices within helium II [Packard, 1972; Guo *et al.*, 2014].

Vortices can be induced in both classical fluids and superfluids. In superfluids these vortices are nucleated when the superfluid is rotated or when the superfluid flow exceeds a critical velocity (the speed of sound in He II at the given temperature). These filaments of vorticity will often tend to have inherent instabilities and will eventually collide. In such collisions these filaments meet at a node point where their direction of rotation and relative velocities are resolved in what is commonly termed a reconnection.

The net effect of the motion and interaction of these vortices is to create a tangle of vortices. These tangles are what we term Quantum Turbulence and it is the investigation of this via numerical modelling that is the basis of my thesis.

## 1.4 Quantum Turbulence

The term 'Quantum Turbulence' was first coined by R. J. Donnelly in a symposium dedicated to the memory of classical turbulence genius, G. I. Taylor in 1986. Though it's accepted that Donnelly imparted the name to this concept, its roots were firmly established in the work of Feynman [Feynman, 1955*b*] as early as 1955 and soon after experimentally demonstrated by Vinen in 1957 [Vinen, 1957*b*, 1958, 1957*c*,*a*].

Turbulence is perhaps best described as the non-linear complex movement of any fluid (liquid or gas) whereby the velocity and pressure fields are subjected to rapid variations both spatially and temporally, where rotation is observed and unless sustained by an external energy source, turbulence will quickly decay by means of an energy cascade from large scale motions to ever smaller scales until eventually viscosity kicks in and dissipates the energy.

This cascade of energy is described as a Richardson Cascade and when Richardson himself sought to describe it in 1922 he produced his adapted Siphonaptera referred to earlier in this chapter. This clearly describes 'little whirls' being created by the 'big whirls' and not big whirls breaking up into little whirls, however this has often been misconstrued. A clear description of the cascade has recently been given by Paoletti and Lathrop [Paoletti & Lathrop, 2011] whereby they say *"one should not picture large vortices or eddies spawning smaller ones, given that this has never been observed. Rather, the correct picture is that large eddies (small k) interact with one another, producing small-scale structures (large k) with high strain and shear that dissipate energy"*.

In helium II we have two interpenetrating fluid components, a normal fluid and a superfluid, which are coupled by a mutual friction and which each have their own velocity fields $\mathbf{v}_n$ and $\mathbf{v}_s$ and temperature-dependent densities $\rho_n$ and $\rho_s$ respectively. Turbulence can be induced and observed in both of the fluid forms. The normal 'classical' fluid will have continuous swirls and eddies whereas the superfluid component has turbulence built from a tangle of discrete quantised vortices.

Figure 1.7: Visualisation of a superfluid vortex tangle from one of our numerical simulations.

When viewed at suitable coarse-grained scales the aggregated movement of these superfluid tangles can be very closely analogous to classical turbulence, although the driving interactions and mechanisms for dissipation of the effects are very different. The relative movement of the two fluids and the nature of their turbulence will act as triggers for the propagations of further turbulence in each of their counterpart fluids. These effects are investigated and described in more detail in later chapters.

## 1.5 Experiments in Quantum Turbulence

Once the case for the two fluid nature of liquid helium II had been accepted, early studies tended to concentrate on thermally driven experiments known as counterflow [Vinen, 1957*b*, 1958, 1957*c*,*a*]. Following the ground breaking work of Donnelly, Tabeling and their co-workers [Maurer & Tabeling, 1998; Stalp *et al.*, 1999; Skrbek *et al.*, 2000] attention shifted to mechanically driven experiments where comparisons with classical turbulence

are more readily accessible.

As counterflow relies completely on the two fluid nature of helium II there is no equivalent experimentation on pure classical fluids. Where superfluid turbulence is incited by mechanical means then many of the methods used in the study of classical fluids can cross over nicely in to the quantum world as in the use of small Pitot tubes to measure pressure head fluctuations [Maurer & Tabeling, 1998] and its ramifications.

A fundamental outcome of experimentation in classical fluids is the ability to visualise the results. Such visualisations are assisted by means of dyes and tracer particles. Given the scale of the vortices which we are trying to detect (a vortex core is of order 1 Angstrom) and evaluate within superfluid helium there is a clear difficulty, for instance in having tracer particles where they would ideally need to be of a lesser magnitude than the manifestation they are trying to demonstrate and not themselves modify the quantum turbulence. The physical environment that needs to be maintained for low temperature experimentation makes visualisation extremely difficult and therefore detection and measurement tend to be the order of the day.

### 1.5.1 Thermally Driven Turbulence

In order to study the nature of superfluid helium II it is necessary to change its natural equilibrium state. A key technique known as thermal counterflow has provided a means by which controlled movement and turbulence of the superfluid can be established.

For a more thorough analysis of the work done in this area Tough carried out a comprehensive review of the published material in 1982 [Tough, 1982] and Donnelly carried out a further such review in 1998 [Donnelly, 1999].

The basic principle is to contain helium II in a closed end tube fitted with a heater at the closed end and the whole apparatus immersed in a helium bath as shown in Figure 1.8.

When heat flux is applied, counterflow is established within the tube. This counterflow develops as heat is picked up by the superfluid being drawn toward the heat source, thus transforming it in to normal fluid and this then flowing away from the heat source. At small values of the heat flux the established counterflow will be laminar. Above critical heat flux values the superfluid and normal fluid components of the counterflow become turbulent.

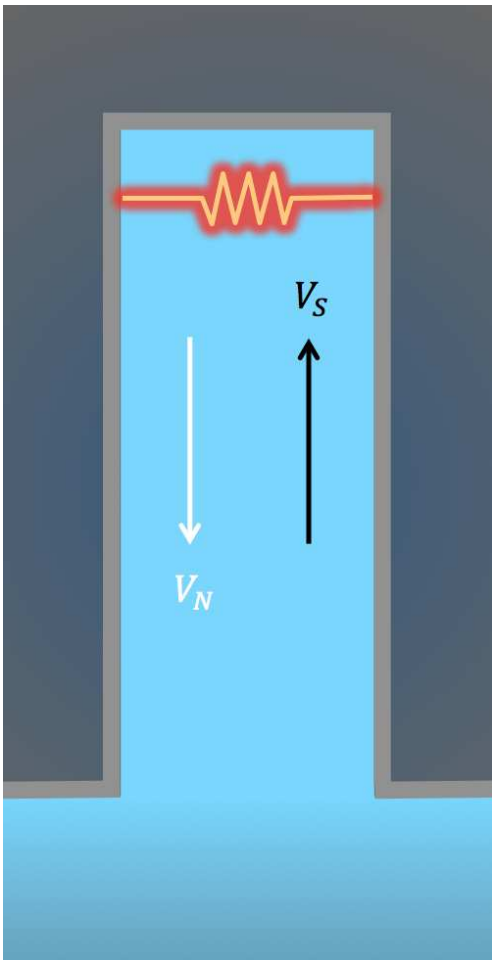


Figure 1.8: Sketch of the experimental setup used to investigate thermal counterflow.

In 1957-1958 W. F. Vinen published a series of four papers in the Proceedings of the Royal Society A [Vinen, 1957*b*, 1958, 1957*c*,*a*]. These papers detailed Vinen's findings from his pioneering experiments with counterflow turbulence. Through the extensive experimentation which was to form the basis of these papers Vinen was able to obtain accurate measures of many of the quantities (amongst others) described above as well as develop a phenomenological model for the turbulence he was investigating.

Using the results from his experiments along with the intuitive assumption that the decay of superfluid tangles could be modelled using a classical Kolmogorov cascade, Vinen developed the Vinen Equation which seeks to define a model for the dynamics of superfluid vortices.

$$\frac{dL}{dt} = \chi_1 \frac{B}{2} \frac{\rho_n}{\rho} \mathbf{v}_{ns} L^{3/2} - \frac{\chi_2 \kappa}{2\pi} L^2, \tag{1.33}$$

where $B$ is the mutual friction coefficient, $\mathbf{v}_{ns}$ is the counterflow velocity, $\rho$ is the total fluid density, $\rho_n$ is the normal fluid density, $\kappa$ is the quantum of circulation and $\chi_1$ and $\chi_2$ are phenomenological constants. In 1988, Schwarz published findings of his research in this area [Schwarz, 1988] but in deriving his analogous equation he uses the laws of vortex dynamics to derive values for $\chi_1$ and $\chi_2$.

In Tough's 1982 review of the large amount of published data he concluded that counterflow turbulence could be classified in to a number of states [Tough, 1982]. The first state, TI, is now generally thought to be when the heat flux is great enough to induce turbulence in the superfluid component but not so great as to also induce turbulence in the normal fluid component. The next state, TII, is when the heat flux is increased to the point whereby the normal fluid becomes turbulent alongside the superfluid. Tough identified a third state, TIII, which is for high-aspect-ratio channels only and has similar properties to TII.

### 1.5.2 Mechanically Driven Turbulence

Routine validation of studies into turbulence has required the search for and discovery of inter alia Kolmogorov scaling (as previously derived). With experiments in classical turbulence we now routinely expect to find Kolmogorov scaling and where it might not be found we look for errors in the modeling rather than accepting its absence.

Quantum turbulence at observable scales bears no visual resemblance to our classical turbulence and yet through modeling and more latterly physical experiment, the following Kolmogorov scaling is indeed found to be present,

$$E(k) = C\epsilon^{2/3}k^{-5/3}. \tag{1.34}$$

Paoletti [Paoletti & Lathrop, 2011], following arguments originally proffered by Kozik and Svistinov [Kozik & Svistunov, 2004, 2005, 2008*a*, 2009, 2008*b*], usefully describes the mechanism for energy dissipation within a superfluid as $T \to 0$ as *"(a) Bundles of nearly parallel quantized vortices form through interactions with the normal fluid that tend to align them. These bundles produce large-scale motions similar to small wavenumber (large spatial extent) eddies in classical fluids. (b) Energy is transmitted to larger k via reconnection between individual vortices [...] (c) Reconnection events trigger polychromatic helical Kelvin waves on the vortex lines. (d) The Kelvin waves interact nonlinearly, producing even larger wavenumbers until they lose energy to phonon emission, which radiates energy to the boundaries. Aspects of the quantum turbulent cascade remain controversial, and this is an active area of research and debate"*. The figure below is a representation of this

decay mechanism clearly identifying the various stages of the dissipation.

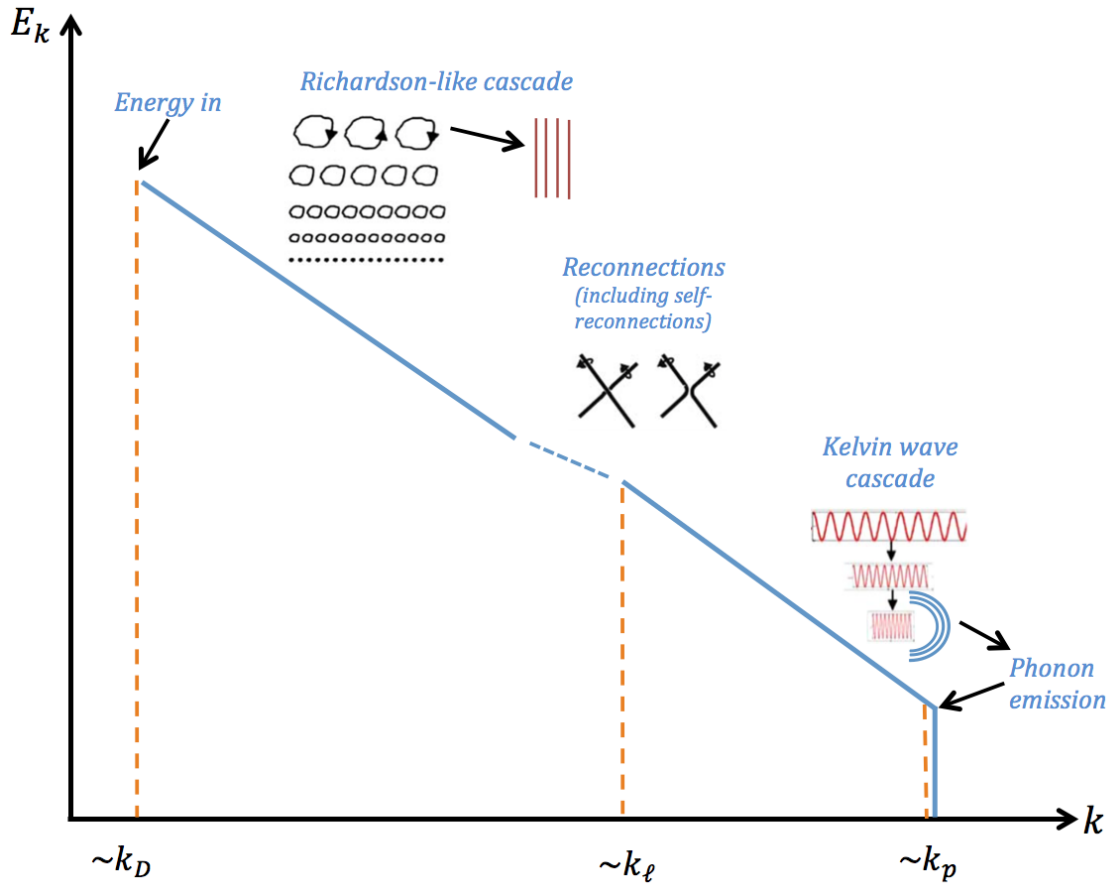


Figure 1.9: Schematic (log-log) of the superfluid energy dissipation. At small wave numbers $k$, the system exhibits a classical Kolmogorov energy cascade due to the interaction of the vortices forming near parallel bundles giving rise to large scale motions ($k_D$). At scales smaller than that of the intervortex spacing ($k_\ell$), quantum effects become important and processes like reconnections (including self-reconnections), and the Kelvin wave cascade dominate the dissipative scaling up to the point where phonon emission ($k_p$) ends the decay. (Some of the sketch elements are adapted from [Vinen, 2006])

At high temperatures where the normal fluid component plays an active role in the superfluid turbulence, it is mutual friction and not phonon emission which is the main dissipative mechanism.

The link between these two forms of turbulence is a fascination that continues to drive research. Two landmark pieces of research have been carried out in this area, firstly by Maurer and Tabeling [Maurer & Tabeling, 1998] looking at Kolmogorov spectra at a range of temperatures and secondly by Salort and Roche [Salort *et al.*, 2010] looking at Kolmogorov spectra in a greater range of experimental set-ups.

Looking at Maurer and Tabeling's 'Local investigation of superfluid turbulence' from 1998 [Maurer & Tabeling, 1998], using the experimental set-up utilising two counter-rotating disks as illustrated in figure 1.10 they set out to measure local pressure fluctuations using a small total-head tube as shown. The outer containment vessel contains the liquid helium with a space above it such that the pressure may be varied to achieve a change in temperature of the contained helium. The whole electromechanical apparatus is immersed in the liquid helium with special DC motors designed to operate at low temperature and to drive the counter-rotating disks each with their four attached paddles measuring 1mm thick by 3cm wide by 3.8cm long at a constant 6Hz.

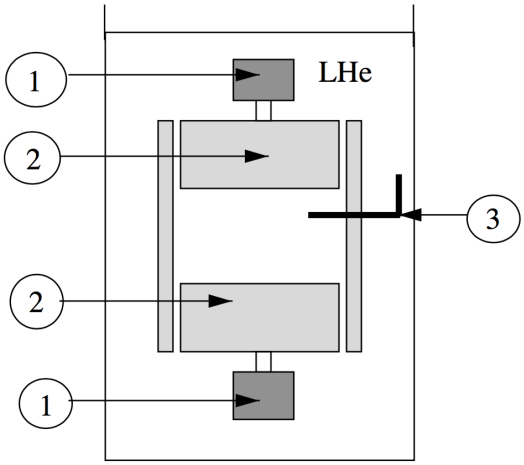


Figure 1.10: Schematic of the experimental set-up of Maurer and Tabeling, 1: DC motor, 2: Propellor/Disk, 3: Probe. Figure taken from [Maurer & Tabeling, 1998].

The probe actually provides pressure readings and these are shown on the left of Figure 1.11 for the three temperatures sampled. Using a Fourier transform the spectra for the energy was derived and is shown on the right of Figure 1.11.

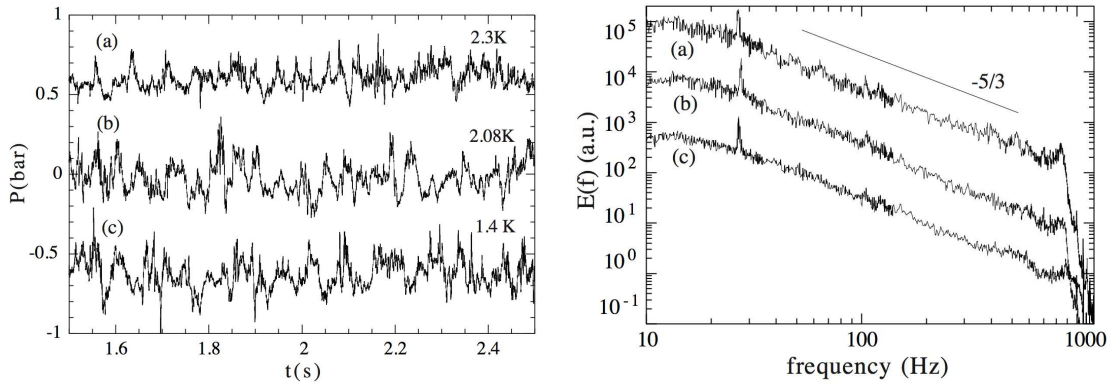


Figure 1.11: Left: time-series obtained by Maurer and Tabeling, Right: energy spectra obtained by Maurer and Tabeling. For both panels the three traces are at the following temperatures; (a) $2.3K$, (b) $2.08K$ and (c) $1.4K$. Figure taken from [Maurer & Tabeling, 1998].

On both the left and right hand panels of Figure 1.11 we see three distinct traces (a), (b) and (c), these traces represent three distinct signals taken at three different temperatures. Trace (a) is taken at 2.3K when the helium is 100% normal fluid (helium I). Trace (b) is taken at 2.08K where the normal fluid component still constitutes 95% of the mix. Finally, trace (c) is taken at 1.4K where the normal fluid component now constitutes less than 10% of the mix.

It should be noted that on the right hand panel of Figure 1.11 the peak around 25Hz is a reading induced by the driving frequency of the disks. Likewise the peak at around 900Hz is a function of the inner containment vessel, which is necessarily open to the outside liquid helium, producing an organ pipe frequency. The results shown, when studied between 30 and 600Hz show a clear power law corresponding to the Kolmogorov '-5/3' scaling. The traces are virtually indistinguishable regardless of the proportion of superfluid present.

In summing up their findings Maurer and Tabeling state: *"The existence of a Kolmogorov-like regime below $T_\lambda$ reveals a striking similarity between ordinary and superfluid turbulence. It also underlines the ubiquity of the cascade process, which does not seem to be sensitive to the precise way how the energy is dissipated at small scales, in agreement with the Kolmogorov picture."*. Following their work the scientific community now had the 'What' and the search for the 'Why' began.

Picking up the baton laid down by Maurer and Tabeling in 1998, Salort and Roche set about providing the first experimental confirmation of the 1998 results as well as extending the range of experimental set-ups over which the confirmation data was gathered.

Turbulent flows were created in two very different physical environments (see Figure 1.12) and with two types of flow (grid turbulence and wake turbulence) in the TSF (Torsional Stall Flutter) wind tunnel and a single flow known as chunk turbulence in the NEEL wind tunnel (an apparatus especially designed by the experimenters at the NEEL Institute in Grenoble).

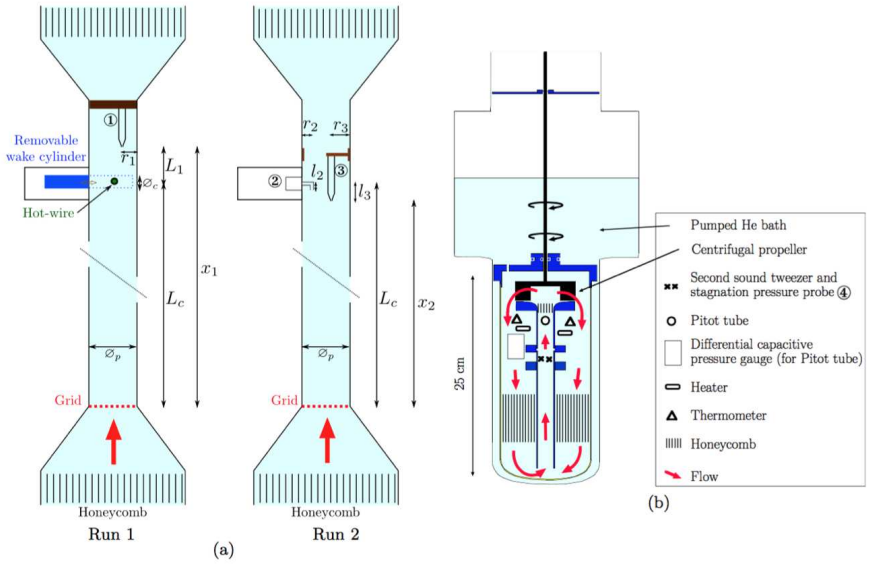


Figure 1.12: Schematic of the experimental set-up of Roche and Salort, (a) TSF wind tunnel: Schematics of the test section and the probe locations for runs 1 and 2. For run 1, a removable cylinder can be inserted across the flow at a distance $L_c$ downstream the grid. It was originally designed to protect a hot-wire during the transient of the system. The stagnation pressure probe 1, located at a distance $L_c + L_1$ downstream the grid can either measure grid turbulence when the cylinder is removed or wake turbulence when the cylinder is inserted in the flow. Probe 1 was not positioned on the pipe axis to avoid the wake of the hot-wire. For run 2, two stagnation pressure probes (2 and 3) are available. (b) NEEL wind tunnel: Schematics and picture of the test section and location of stagnation pressure probe 4. Figure and caption taken from [Salort *et al.*, 2010].

The two flows studied in the TSF apparatus produced quite different results and in analysing their results from the Wake Turbulence Flow, the experimenters postulated that the absence of Kolmogorov scaling was similar to results obtained in classical turbulence when measuring spectra in strongly inhomogeneous flows.

The grid turbulence model was chosen as results for this type of flow in classical fluids are well understood and correlations (if observed in superfluid flows) could be readily compared. They tested their set-up at a range of temperatures (from 2.6K corresponding to 100% normal fluid down to 1.7K corresponding to 24% normal fluid component) and a range of driving velocities (from 0.4m/s to 5m/s) and found that they do indeed see a

Kolmogorov scaling for all realisations of the flow as shown in Figure 1.13 (left).

Using their custom designed NEEL wind tunnel, fixing the temperature of the helium II to 1.55K (around 86% superfluid) and deploying a range of driving speeds (from 0.25 - 1.3 m/s), once again the experimenters were able to demonstrate Kolmogorov scaling, see Figure 1.13 (right).

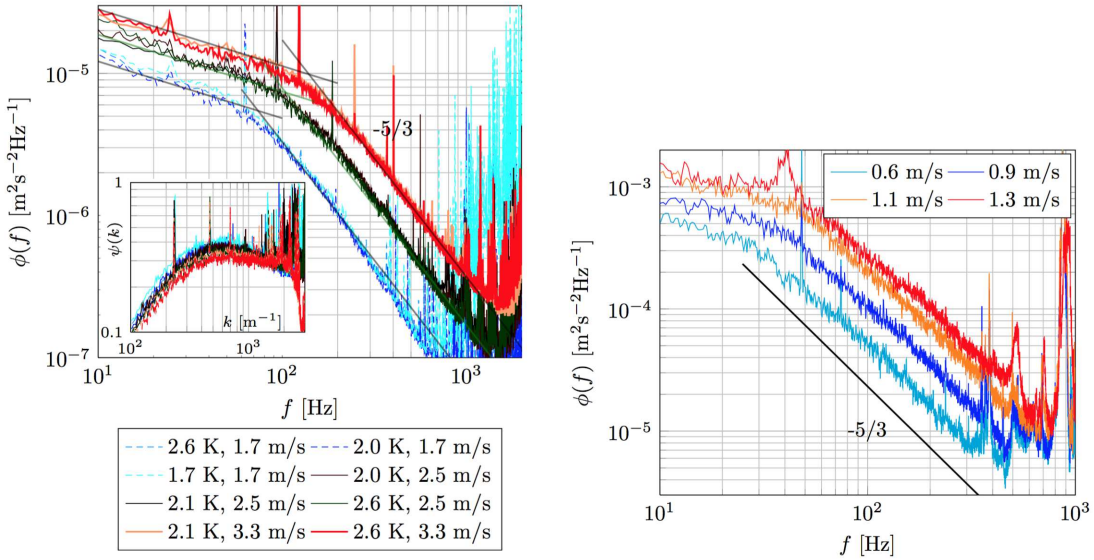


Figure 1.13: Left: Velocity spectra obtained for various temperatures and driving speeds by Roche and Salort using the TSF Wind Tunnel, Right: Velocity spectra obtained at $1.5K$ for various driving speeds by Roche and Salort using the NEELs Wind Tunnel. Figure taken from [Salort *et al.*, 2010].

Salort and Roche were able for the first time to experimentally validate the results obtained by Maurer and Tabeling, and Kolmogorov scaling in superfluid turbulent flows is now accepted as a real phenomenon.

### 1.5.3 Visualisation of Quantum Turbulence

If things are hard to measure and view in the 'normal' world then they are almost impossible to measure and view in our very specialist quantum world. Much effort is currently devoted to devise techniques that allow us to visualise mechanisms where even tracer particles of more than a few atoms are already larger than the system to be imaged or measured.

A recent publication in PNAS [Guo *et al.*, 2014] provided a useful overview of the latest techniques being used in the superfluid helium world. There are three principle techniques currently being used, two are adaptations from the field of classical fluid dynamics: PIV,

and PTV and a third which utilises a unique property of helium atoms to create a direct visualisation of atoms within the superfluid itself.

PIV (particle image velocimetry) is an aggregate method for tracking an array of tracer particles, while PTV (particle tracking velocimetry) seeks to track individual tracer particles. The third technique, known as '$He_2^*$ Fluorescence Imaging Technique' creates triplet molecules within the superfluid which themselves act as tracer particles.

PIV is a somewhat broad brush approach to imaging and has been successfully used with micron-sized solid particles to obtain averaged measurements within a section of fluid [Zhang & Van Sciver, 2005*a*; Zhang *et al.*, 2004; Zhang & Van Sciver, 2005*b*].

PTV allows our focus to be refined down to resolutions where individual vortex lines can be imaged [Bewley *et al.*, 2006]. Furthermore PTV has allowed us to observe reconnections of superfluid vortices for the first time ever [Paoletti *et al.*, 2010], as shown in Figure 1.14 below.

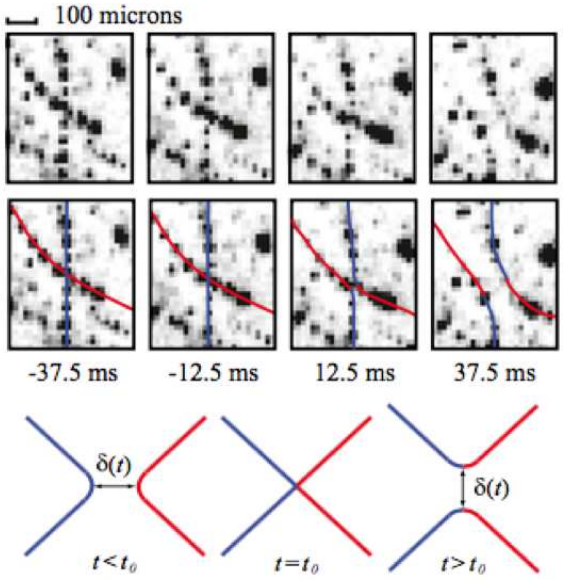


Figure 1.14: Image showing experimental evidence of vortex reconnection using PTV. Figure taken from [Guo *et al.*, 2014].

Researchers at Charles University in Prague have recently used PTV with solid deuterium particles as tracers to study velocity and acceleration statistics within steady state thermal counterflow in helium II [La Mantia *et al.*, 2013, 2012; La Mantia & Skrbek, 2014]. They found that at length scales smaller than the typical intervortex spacing they

see non-classical (quantum) statistics for the velocities and accelerations, however if they looked at scales larger than the intervortex spacing then they observe classical statistics. It seems that where Kolmogorov scaling leads, other classical fluid effects follow and in this research the particle acceleration statistics at times mirror their classical counterparts.

The exact nature of the normal fluid flow in counterflow has long exercised researchers in the field. The technique of $He_2^*$ fluorescence imaging developed at Florida State University has allowed researchers to create tracer particles within helium II which at high T are bound to the normal fluid and which allow for visualising only the normal fluid component of the thermal counterflow [Benderskii *et al.*, 1999] (at low temperatures these tracer particles would become trapped on the vortex cores and allow direct visualisation of the superfluid voritces).

The figure below shows on the left a thin line (80$\mu$m) of fluoresced tri-atomic helium molecules in our helium II with no heat flux applied. The middle snapshot shows a similar tracer 900 ms after creation in a laminar flow resultant from a mild heat flux of 10 mW/cm$^2$. The rightmost panel shows an initially straight tracer line a mere 15 ms later in what is clearly a turbulent flow resultant from a heat flux of 215 mW/cm$^2$.

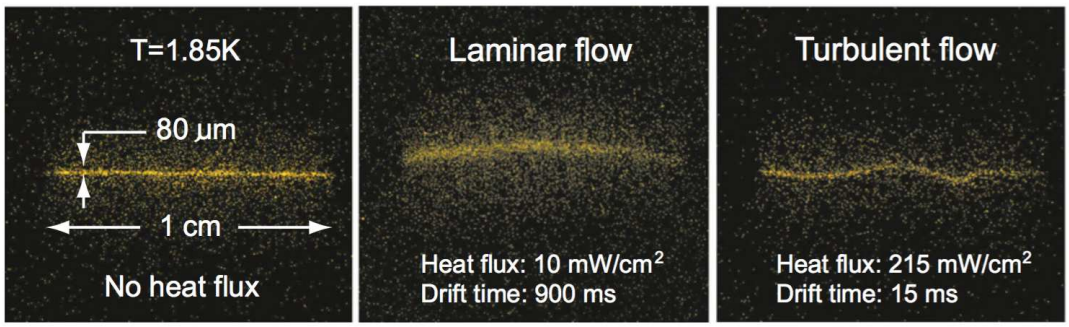


Figure 1.15: Images of fluorescing tracer lines of $He_2^*$. Figure taken from [Guo *et al.*, 2014].

Clearly, the once impenetrable world of quantum turbulence is slowly being opened up to human gaze and will doubtless create a launch pad for even further study.

## 1.6 Publications Arising

The research for my thesis has resulted in the publication of two papers and a further paper in preparation. The publications arising from my research are included as chapters 4 and 5 as follows:

Chapter 4: - Baggaley *et al.* [2012*d*]

Chapter 5: - Sherwin-Robson *et al.* [2015]

# Chapter 2

# Numerical method

Time and money being no object it would be sensible to carry out most experiments into superfluid turbulence in a real physical environment. However, the physical constraints of experimental setup are such that the costs are generally prohibitive and the setup times for a given experiment too long to allow this to be the only means by which we investigate the matter. While the experimentalists wrestle with their pressure vessels, vacuums and microscopic probes, mathematicians can numerically investigate the properties of superfluids (including some not currently accessible in experiments) and thus assist the experimentalists.

Mathematicians take a number of approaches to computationally represent the physical world and to establish and test the rules that govern it. Following on from the pioneering work of Schwarz [Schwarz, 1985], we model superfluid vortices as space curves $\mathbf{s} = \mathbf{s}(\xi, t)$ of infinitesimal thickness (where $t$ is time and $\xi$ is arc length).

## 2.1 The Schwarz Equation

Since its introduction in 1985 [Schwarz, 1985] the Vortex Filament Model (VFM) which utilises the Schwarz Equation, whereby we model superfluid vortex lines as space curves $\mathbf{s}(\xi, t)$ (where $t$ is time and $\xi$ is arc length) of infinitesimal thickness with circulation $\kappa = 9.97 \times 10^{-4}$ cm$^2$/s has become the de-facto standard for modelling vortex filaments in superfluids [Adachi *et al.*, 2010; Baggaley & Barenghi, 2012; Hanninen & Baggaley, 2014]. Though the mathematics involved can tend towards the complex, the underlying principles adopted by Schwarz have an elegant simplicity. The key forces deemed to be acting on the vortex filaments are the Magnus force (arising from a flow past a rotating body) and the drag force (arising from the interaction of the vortices with the normal fluid). Resolving these forces gives rise to the equation of motion for a vortex point:-

$$\frac{d\mathbf{s}}{dt} = \mathbf{v} = \mathbf{v}_s + \alpha\mathbf{s}' \times (\mathbf{v}_n^{ext} - \mathbf{v}_s) - \alpha'\mathbf{s}' \times [\mathbf{s}' \times (\mathbf{v}_n^{ext} - \mathbf{v}_s)]. \tag{2.1}$$

This is the Schwarz Equation where $\alpha$ and $\alpha'$ are temperature-dependent friction coefficients [Barenghi *et al.*, 1983; Donnelly & Barenghi, 1998], $\mathbf{v}_s$ is the superfluid velocity, $\mathbf{v}_n$ is the normal fluid velocity, and a prime denotes a derivative with respect to arc length (hence $\mathbf{s}' = d\mathbf{s}/d\xi$ is the local unit tangent vector, and $C = |\mathbf{s}''|$ is the local curvature; the radius of curvature, $R = 1/C$, is the radius of the osculating circle at the point $\mathbf{s}$).

### 2.1.1 The Magnus Force

The eponymous Magnus force is one which was described by the german physicist Heinrich Gustav Magnus, after Sir Isaac Newton's earlier observations. It is intended to explain the deviation from the 'normal' path of a rotating body. Although Magnus postulated the effect to be the result of the roughness of the outer skin of the rotating object and the viscosity of the medium through which it was travelling, such forces would be too small to explain the size of deviations observed.

Our filament within a uniform flow in 2-dimensions is represented in figure 2.1. We consider our filament to be a circular body with radius $a_0$, which has a clockwise circulation $\kappa$ around it, sat in a uniform flow of velocity $U$ from the left. Where the circulation opposes the flow at the 6 o'clock position then the velocity of flow is reduced and the pressure on the filament is increased at this point, conversely, where the circulation is aligned with the flow at the 12 o'clock position then the velocity of the flow is increased resulting in an area of low pressure on the filament at this point. This pressure differential gives rise to a resultant force $\mathbf{F}_m$ acting on our filament tending to move it upwards in a direction perpendicular to the flow. This is akin to the aerofoil lift principle, well understood in classical mechanics.

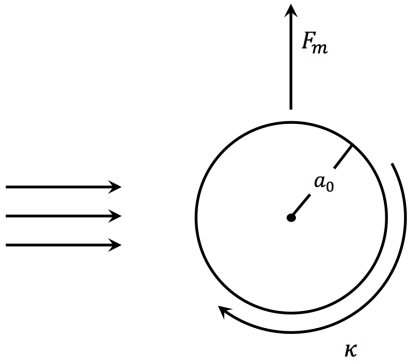


Figure 2.1: Visualisation of Magnus Force in 2D

In our 3D superfluid simulations, the Magnus force acting on the vortex filaments is given by:

$$\mathbf{F}_m = \rho_s \kappa \mathbf{s}' \times (\mathbf{v} - \mathbf{v}_s), \tag{2.2}$$

where $\rho_s$ is the superfluid density and $\kappa$ is the circulation.

### 2.1.2 The Drag Force

Although vortex lines are an manifestation of the superfluid, nonetheless other than at very low temperatures ($T < 0.7$K) they exist in a space where there is also a normal fluid and the vortex interaction with this fluid results in mutual friction forces at their interface.

If we consider our vortex filament as a rectilinear tube orientated along the z-axis, then all drag forces acting upon it act in a plane perpendicular to the tangent $\mathbf{s}'$ which can be resolved in to two components, one in the x direction and one in the y direction.

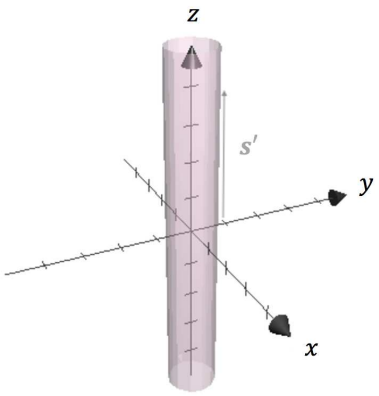


Figure 2.2: Visualisation of Drag Force

It is generally believed that the drag force is a result of the collisions between excitations such as rotons and the vortices. This gives rise to a drag force of the form:

$$\mathbf{F}_d = -\gamma_0 \mathbf{s}' \times [\mathbf{s}' \times (\mathbf{v}_n - \mathbf{v})] + \gamma_0' \mathbf{s}' \times (\mathbf{v}_n - \mathbf{v}), \tag{2.3}$$

where $\gamma_0$ and $\gamma_0'$ are one set of temperature dependent friction coefficients. It is accepted that the scale of these interactions is directly related to the relative velocities of the superfluid component $\mathbf{v}_s$ and the normal fluid component $\mathbf{v}_n$. Following Donnelly [Donnelly [1991]-chapter 3] we can now express the drag force as:

$$\mathbf{F}_d = -\alpha \rho_s \kappa \mathbf{s}' \times [\mathbf{s}' \times (\mathbf{v}_n - \mathbf{v}_s)] - \alpha' \rho_s \kappa \mathbf{s}' \times (\mathbf{v}_n - \mathbf{v}_s), \tag{2.4}$$

where $\alpha$ and $\alpha'$ are another set of temperature dependent friction coefficients which are related to the experimentally determined Hall-Vinen parameters $\mathcal{B}$ and $\mathcal{B}'$ by $\alpha = \mathcal{B}\rho_n/2\rho$ and $\alpha' = \mathcal{B}'\rho_n/2\rho$. The relationship between $\alpha$, $\alpha'$ and $\gamma_0$, $\gamma_0'$ is given by:

$$\gamma_0 = \frac{\rho_s\kappa\alpha}{(1-\alpha')^2+\alpha^2}, \tag{2.5}$$

$$\gamma_0' = \frac{\rho_s\kappa(\alpha^2-\alpha'+\alpha'^2)}{(1-\alpha')^2+\alpha^2}. \tag{2.6}$$

### 2.1.3 Resolving the forces

Now that we have the forces which act up on our vortex (neglecting inertia) we can use Newton's Second Law $\mathbf{F} = m\mathbf{a}$ to formulate our equation of motion. Given that the radius of the vortex core is in the order of 1 Angstrom, we can effectively assume the mass of the vortex to be 0, and hence the total force must be zero.

$$\mathbf{F} = 0, \tag{2.7}$$

$$\Rightarrow \mathbf{F}_d + \mathbf{F}_m = 0. \tag{2.8}$$

Substituting our values for $\mathbf{F}_m$ and $\mathbf{F}_d$ from above gives:

$$\rho_s\kappa\mathbf{s}'\times(\mathbf{v}-\mathbf{v}_s) - \alpha\rho_s\kappa\mathbf{s}'\times[\mathbf{s}'\times(\mathbf{v}_n-\mathbf{v}_s)] - \alpha'\rho_s\kappa\mathbf{s}'\times(\mathbf{v}_n-\mathbf{v}_s) = 0, \tag{2.9}$$

$$\rho_s\kappa\mathbf{s}'\times[(\mathbf{v}-\mathbf{v}_s) - \alpha\mathbf{s}'\times(\mathbf{v}_n-\mathbf{v}_s) - \alpha'(\mathbf{v}_n-\mathbf{v}_s)] = 0. \tag{2.10}$$

The above means that the terms in the square brackets must now either be in the direction of $\mathbf{s}'$ or be zero. If we assume the latter we obtain:

$$\mathbf{v} = \mathbf{v}_s + \alpha\mathbf{s}'\times(\mathbf{v}_n-\mathbf{v}_s) + \alpha'(\mathbf{v}_n-\mathbf{v}_s), \tag{2.11}$$

which can be rewritten as:

$$\mathbf{v} = \mathbf{v}_s + \alpha\mathbf{s}'\times(\mathbf{v}_n-\mathbf{v}_s) - \alpha'\mathbf{s}'\times[\mathbf{s}'\times(\mathbf{v}_n-\mathbf{v}_s)]. \tag{2.12}$$

The above simplification from equation 2.11 to equation 2.12 was carried out using the

following:

$$\mathbf{s}' \times [\mathbf{s}' \times (\mathbf{v}_n - \mathbf{v}_s)] = (\mathbf{s}' \cdot (\mathbf{v}_n - \mathbf{v}_s))\mathbf{s}' - (\mathbf{s}' \cdot \mathbf{s}')(\mathbf{v}_n - \mathbf{v}_s), \tag{2.13a}$$

$$= (\mathbf{s}' \cdot (\mathbf{v}_n - \mathbf{v}_s))\mathbf{s}' - (\mathbf{v}_n - \mathbf{v}_s), \qquad \mathbf{s}' \cdot \mathbf{s}' = 1 \tag{2.13b}$$

$$= -(\mathbf{v}_n - \mathbf{v}_s); \quad \mathbf{s}' \cdot (\mathbf{v}_n - \mathbf{v}_s) = 0 \text{ (orthogonal vectors).} \tag{2.13c}$$

## 2.2 Modelling the Superfluid Velocity

The superfluid velocity $\mathbf{v}_s$ consists of two components such that: $\mathbf{v}_s = \mathbf{v}_s^{ext} + \mathbf{v}_s^{self}$. The former $\mathbf{v}_s^{ext}$ represents any externally applied superflow; the latter $\mathbf{v}_s^{self}$ the self-induced velocity at the point $\mathbf{s}$. There are two methods for evaluating the self-induced component of the superfluid velocity, these being; The Biot-Savart Law or the simpler though usually less accurate Local Induction Approximation (LIA).

### 2.2.1 Biot-Savart

For a classical, incompressible fluid it has been established [Saffman, 1993] that the velocity field $\mathbf{v}$ is determined by the instantaneous distribution of vorticity $\boldsymbol{\omega}$ via the Biot-Savart law:

$$\mathbf{v}(\mathbf{x}) = \frac{1}{4\pi} \int \frac{\boldsymbol{\omega}(\mathbf{x}') \times (\mathbf{x} - \mathbf{x}')}{|\mathbf{x} - \mathbf{x}'|^3} d^3\mathbf{x}', \tag{2.14}$$

where the integral extends over the entire flow.

In a superfluid, the self-induced velocity $\mathbf{v}_s^{self}$ at the point $\mathbf{s}$, results from Equation 2.14 in the limit of concentrated vorticity:

$$\mathbf{v}_s^{self}(\mathbf{s}) = -\frac{\kappa}{4\pi} \oint_{\mathcal{L}} \frac{(\mathbf{s} - \mathbf{r})}{|\mathbf{s} - \mathbf{r}|^3} \times \mathbf{dr}, \tag{2.15}$$

where the line integral extends over the entire vortex configuration $\mathcal{L}$ (for a full derivation of this see Appendix A).

A clear problem with equation 2.15 is that as $\mathbf{r} \to \mathbf{s}$ the integral diverges and when $\mathbf{r} = \mathbf{s}$ the integral is singular. Schwarz addressed himself to this, but noted that although a similar problem existed in regard to classical hydrodynamics, no proposed classical solution would be transferrable to this superfluid environment as the physics of the vortex core is quite different in both situations. Schwarz proposed a solution to the problem [Schwarz, 1985] whereby the self induced velocity $\mathbf{v}_s^{self}$ is decomposed into two components; a local velocity $\mathbf{v}_s^{loc}$ and a nonlocal velocity $\mathbf{v}_s^{non}$ such that $\mathbf{v}_s^{self} = \mathbf{v}_s^{loc} + \mathbf{v}_s^{non}$.

If we now step through Schwarz's analysis of the problem as outlined by Aarts [Aarts, 1993], we begin by noting that the velocity of a superfluid vortex ring has been experimentally observed to obey the velocity of a classical vortex ring [Lamb, 1945; Leonard, 1980; Saffman, 1970], where the velocity is given by:

$$\mathbf{v}_{ring}(\mathbf{s}) = -\frac{\kappa}{4\pi}\oint_{\mathcal{L}_\chi}\frac{(\mathbf{s}-\mathbf{r})}{|\mathbf{s}-\mathbf{r}|^3}\times\mathbf{dr}, \tag{2.16}$$

where $\mathcal{L}_\chi$ denotes the line integral which extends over the vortex configuration but excludes a length $\chi$ (which is of the same order as the core size) from each side of $\mathbf{r}$ such that the integral does not diverge. The parameter $\chi$ is dependent upon the structure of the vortex core; due to the physical nature of superfluid vortices where their density drops to zero within the core, they most closely correlate to the behaviour of classical hollow-core vortices. In a hollow-core vortex $\chi$ is given by:

$$\ln\left(\frac{2\chi}{a_0}\right) = \frac{1}{2}. \tag{2.17}$$

The integral in equation 2.16 can now be analytically solved [Saffman, 1970]. The resulting velocity is dependent upon both the radius of the vortex ring $R_r$ and the vortex core size $a_0$:

$$\mathbf{v}_{ring}(\mathbf{s}) = -\frac{\kappa}{4\pi R_r}\ln\left(\tan\frac{\chi}{4R_r}\right)\mathbf{e}_\perp, \tag{2.18}$$

where $\mathbf{e}_\perp$ is a unit vector perpendicular to the plane of the vortex ring. Given that $a_0 << R_r$ we can employ the approximation $\tan(\chi/4R_r) \approx \chi/4R_r$. This along with Eq. 2.17 gives the velocity of the ring to be:

$$\mathbf{v}_{ring}(\mathbf{s}) = \frac{\kappa}{4\pi}\ln\left(\frac{8R_r}{e^{1/2}a_0}\right)\frac{\mathbf{e}_\perp}{R_r}. \tag{2.19}$$

Now that we have the value for the total velocity of the ring we need to decompose this in to a local contribution and a nonlocal contribution whereby: $\mathbf{v}_{ring} = \mathbf{v}_{ring}^{loc} + \mathbf{v}_{ring}^{non}$. This decomposition is shown in Fig. 2.3

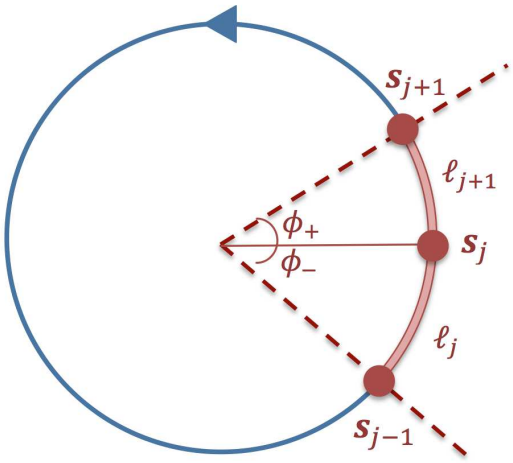


Figure 2.3: The decomposition of a vortex ring in to a local component (red) and a nonlocal component (blue).

Schwarz deals in the first instance with the nonlocal contribution which can be obtained by the integration of equation 2.16 over the path $\mathcal{L}_{non}$ [Lamb, 1945] which excludes the local segment of the ring:

$$\mathbf{v}_{ring}^{non}(\mathbf{s}) = -\frac{\kappa}{4\pi}\oint_{\mathcal{L}_{non}} \frac{(\mathbf{s}-\mathbf{r})}{|\mathbf{s}-\mathbf{r}|^3} \times \mathbf{dr}, \tag{2.20}$$

$$= -\frac{\kappa}{8\pi R_r} \ln\left[\tan(\phi_+/4)\tan(\phi_-/4)\right] \mathbf{e}_\perp. \tag{2.21}$$

where $\phi_+$ and $\phi_-$ are angles related to the size of the local contribution (as seen in figure 2.3). If we now once again use our approximation to tan we can simplify the expression for the nonlocal contribution. This can then be subtracted from the total velocity of the ring to yield the expression for the local contribution:

$$\mathbf{v}_{ring}^{loc}(\mathbf{s}) = \frac{\kappa}{4\pi R_r} \ln\left(\frac{2\sqrt{\ell_j \ell_{j+1}}}{e^{1/2} a_0}\right) \mathbf{e}_\perp, \tag{2.22}$$

where $\ell_j$ and $\ell_{j+1}$ are the arc lengths of the curves between the point $\mathbf{s}_j$ and the adjacent points $\mathbf{s}_{j-1}$ and $\mathbf{s}_{j+1}$ along the vortex. We now have the local velocity of our ring provided $R >> \ell >> a_0$. As the local term is not dependent upon the remainder of the vortex, the self induced velocity of a given vortex structure can be calculated using this for the local component. To do this in a more general case we will require an expression for the vector $\mathbf{e}_\perp$. In deriving this expression it is useful to note the following set of mutually perpendicular vectors $\mathbf{s}'$, $\mathbf{s}''$ and $\mathbf{s}' \times \mathbf{s}''$ (remembering that a prime denotes the derivative with respect to the arc length $\xi$ therefore $\mathbf{s}' = \frac{\mathrm{d}\mathbf{s}}{\mathrm{d}\xi}$ and $\mathbf{s}'' = \frac{\mathrm{d}^2\mathbf{s}}{\mathrm{d}\xi^2}$), as seen below in figure

2.4:-

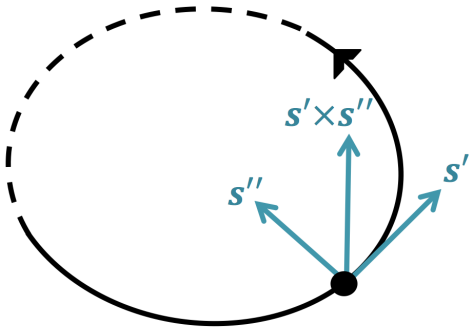


Figure 2.4: Illustration of the set of mutually perpendicular vectors; the tangent $\mathbf{s}'$, the principal normal $\mathbf{s}''$ and the binormal $\mathbf{s}' \times \mathbf{s}''$.

The tangent vector $\mathbf{s}'$ is a unit vector and therefore $|\mathbf{s}'| = 1$. The length of the principal normal is the inverse of the local radius of curvature $R$ and is therefore $|\mathbf{s}''| = R^{-1}$. Given the lengths of the first two vectors we can obtain the length of the binormal vector $\mathbf{s}' \times \mathbf{s}''$ which is given by $|\mathbf{s}' \times \mathbf{s}''| = R^{-1}$. Using these equations we can form an expression for $\mathbf{e}_\perp$:

$$\mathbf{e}_\perp = R\, \mathbf{s}' \times \mathbf{s}''. \tag{2.23}$$

If we now substitute the above expression in to equation 2.22 we can obtain a generalised expression for the local component of the velocity of a vortex:

$$\mathbf{v}_s^{loc}(\mathbf{s}) = \frac{\kappa}{4\pi} \ln\left(\frac{2\sqrt{\ell_j \ell_{j+1}}}{e^{1/2} a_0}\right) \mathbf{s}' \times \mathbf{s}''. \tag{2.24}$$

Finally, we can now form the complete expression for the total self induced velocity of a vortex:-

$$\mathbf{v}_s^{self}(\mathbf{s}_j) = \mathbf{v}_s^{loc}(\mathbf{s}_j) + \mathbf{v}_s^{non}(\mathbf{s}_j) = \frac{\kappa}{4\pi} \ln\left(\frac{2\sqrt{\ell_j \ell_{j+1}}}{e^{1/2} a_0}\right) \mathbf{s}_j' \times \mathbf{s}_j'' + \frac{\kappa}{4\pi} \oint_{\mathcal{L}'} \frac{(\mathbf{s}_j - \mathbf{r})}{|\mathbf{s}_j - \mathbf{r}|^3} \times \mathbf{dr}, \tag{2.25}$$

where $\mathcal{L}'$ is the original vortex configuration $\mathcal{L}$ but now without the section between $\mathbf{s}_{j-1}$ and $\mathbf{s}_{j+1}$. The superfluid vortex core radius $a_0 \approx 10^{-8}$ cm now acts as a cut-off parameter.

### 2.2.2 Local Induction Approximation (LIA)

The concept of the Local Induction Approximation was advanced by Schwarz [Schwarz, 1985] to overcome the computational overhead of a full Biot-Savart modelling. Schwarz offers:

$$\mathbf{v}_s^{self}(\mathbf{s}_j) \simeq \frac{\kappa}{4\pi}\, \mathbf{s}_j{}' \times \mathbf{s}_j{}''\, ln\left(\frac{R}{a_0}\right), \tag{2.26}$$

which provides a first order approximation to the self induced velocity given by the Biot-Savart Law. For a full derivation of this methodology please see Appendix B.

It should be noted, that more recent studies of the LIA [Adachi *et al.*, 2010] have lead to the conclusion that it is not sufficient to address the relative complexity of quantum turbulence, as it cannot capture large-scale classical-like flows.

## 2.3 Basic structure of the code

In the remainder of this chapter I will run through the code I have used to model my superfluid world, namely 'qvort'. This fortran code has been developed by Dr. Andrew Baggaley and adapted and further developed by me in the course of my research. I will begin with the basic structure of the code and then I will move on to some of the more complex concepts and detail how they are implemented.

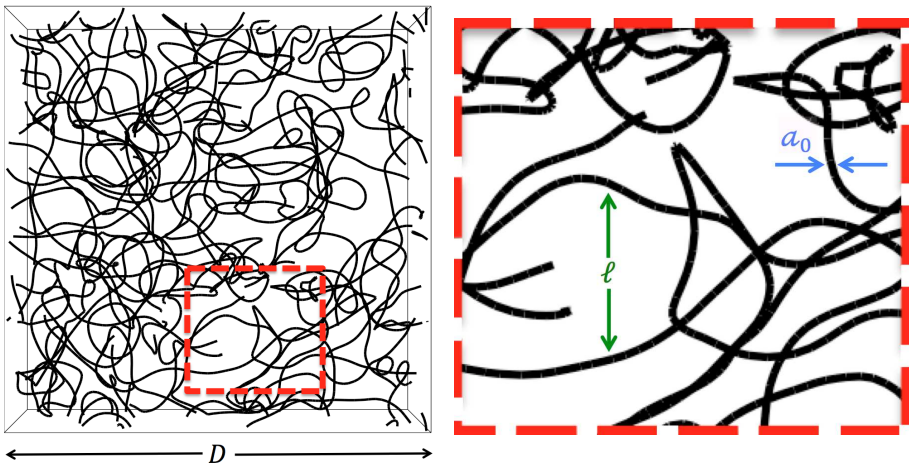


Figure 2.5: Left: A numerically generated view of superfluid turbulence, where $D$ represents the size of the numerical cube. Right: The highlighted section from the left panel is enlarged to highlight some key dimensions within our superfluid tangle.

On the left of Figure 2.5 we have a snapshot of a numerically created 3D cube containing our representation of superfluid turbulence. On the right we highlight two key dimensions which are fundamental to our model; $a_0$ is the vortex core size which in our model of superfluid Helium II is given to be $a_0 = 8.244023 \times 10^{-9}$cm [Barenghi *et al.*, 1983], $\ell$ is the typical distance between any two vortices known as the inter-vortex spacing and within our simulations it will typically be in the range of $10^{-3} < \ell < 10^{-2}$cm.

Initially we numerically discretise the vortex lines into a large number of vortex points $\mathbf{s}_j$ where $j = 1, \ldots, P$. The code uses this concept to populate its numerical domains.

The initial conditions for a single simulation under which my domain is populated requires the number of vortex points $P$ to be defined. This number will however vary as each simulation progresses due to the need to maintain both a minimum and a maximum distance between the vortex points as the vortices are advected in the flow.

### 2.3.1 Key parameters - physical space and time frame

**Physical Space**

Although the code could work with large parameters for the defined space, in practice the larger the space the greater the computational effort required and the longer the runs take to simulate a passage in real time. Even at a physical size of a mere 1 mm$^3$, at the highest resolutions and at zero temperature, one second of real time can take 3 months to run on a relatively high powered desktop computer.

The key physical parameters are ...

- $D\ (cm)$ - **the computational box size:**
  My research has restricted itself to periodic domains representing a real world space of 1 mm$^3$. The choice of this space size allows me to adequately deal with the number of calculations required to calculate and represent the various interactions between, essentially, the vortex points in this space. Experimental physicists conduct their investigations in spaces ranging from the 1 mm$^3$ in Lancaster [Bradley *et al.*, 2011] through to 4.5 cm$^3$ in Manchester [Walmsley & Golov, 2008] and more recently attempts are being made to create an actual 1 m$^3$ space [Saint-Michel *et al.*, 2014].
- $\delta$ - **the numerical resolution:**
  This determines the limits to the proximity of any two neighbouring vortex points. No two adjacent points are allowed to be further apart than $\delta$ or closer together than $\delta/2$. The choice of $\delta$ needs to be sufficiently small such that the necessary fine

details in the domain can be resolved. Smaller is better but also computationaly more expensive and inevitably this value is a trade-off. A good utilitarian value is $1.6 \times 10^{-3}$cm.

- $\alpha$ & $\alpha'$ - **the mutual friction coefficients**:
  The values of these two friction coefficients define the temperature at which the simulation is running. They are bound pairs looked up from tables for any given temperature, and are themselves derived from the Hall-Vinen parameters $\mathcal{B}$ and $\mathcal{B}'$ [Hall & Vinen, 1956] where $\alpha = \rho_n \mathcal{B}/2\rho$ and $\alpha' = \rho_n \mathcal{B}'/2\rho$ which are experimentally measured values [Donnelly & Barenghi, 1998].

### Time Frame

For each simulation we need to define the total time that the physical world will be modelled over. We input the time as a given number of time intervals:

- $\Delta t$ $(s)$ - **the size of each time interval:**
  This is the temporal equivalent of *the numerical resolution* ($\delta$ above). This needs to be small enough to allow the simulation to pick up the slightest of changes and yet not so small as to 'choke' the computer with the amount of steps required. Once again small is best but large is fastest, however there are constraints to the maximum size and where sufficient detail cannot be resolved with a given choice of $\Delta t$, the code will abort the run and report the applicable maximum time interval allowable based on the following argument.

  The fastest motions within our domain are those which occur on the smallest scale. From above we know the smallest scale within our code is $\delta/2$ and so a Kelvin wave on this scale has a wavenumber of $k_{max} = 4\pi/\delta$. Along a straight vortex the long wave approximation ($ka_0 \ll 1$) to the angular frequency of a Kelvin wave is given by [Barenghi *et al.*, 1985]:

$$\omega \approx -\frac{\kappa k^2}{4\pi}[\ln 2/(ka_0) - \gamma], \tag{2.27}$$

  where $\gamma = 0.5772$ is Euler's constant. Given $k = k_{max}$ above we derive the timescale for the fastest motions to be:

$$(\omega_{max})^{-1} \approx \frac{\pi(\delta/2)^2}{4\kappa \ln(\delta/(2\pi a_0) - \gamma)}. \tag{2.28}$$

  Based on the above a suitable choice for the maximum time interval would be defined

by:

$$\Delta t < \frac{(\delta/2)^2}{\kappa \log(\delta/2\pi a_0)}. \tag{2.29}$$

At temperatures above absolute zero the damping effect of mutual friction means that this restriction can be used for mere guidance rather than absolute adherence.

- $N$ - **the number of time intervals:**
  Simple arithmetic provides us this value given our time interval and our desired real world simulation time.

### 2.3.2 Data storage

To understand how a simulation works it is important to know how the data is stored. For each vortex point $\mathbf{s}_j$ (where $j = 1, \ldots, P$) we store the following information (amongst others)...

- The position, stored as a 3 element array - $\mathbf{s}_j$
- The velocity, stored as a 3 element array - $\mathbf{v}_j$
- The array index of the vortex point in front, stored as an integer number - $f_j$
- The position of of the vortex point in front, stored as a 3 element array - $\mathbf{s}_{j+1}$
- The array index of the vortex point behind, stored as an integer number - $b_j$
- The position of the vortex point behind, stored as a 3 element array - $\mathbf{s}_{j-1}$
- The position of of the vortex point 2 in front, stored as a 3 element array - $\mathbf{s}_{j+2}$
- The position of the vortex point 2 behind, stored as a 3 element array - $\mathbf{s}_{j-2}$
- The velocity at the previous time-step, stored as a 3 element array - $\mathbf{v}_j^{n-1}$
- The velocity at the time-step 2 previous, stored as a 3 element array - $\mathbf{v}_j^{n-2}$

The above information is essential for orientating the vortices, for calculating the velocities, for calculating the new vortex point positions and for calculating and reporting diagnostics such as the curvature information.

Below is a simple visualisation of a vortex ring with a nominal 20 vortex points. The actual shape of these rings can be anything and the number of vortex points is in a range from 5 upwards (5 is the minimum due to the higher order derivatives we use for the spatial derivatives which require 2 points either side of any given point).

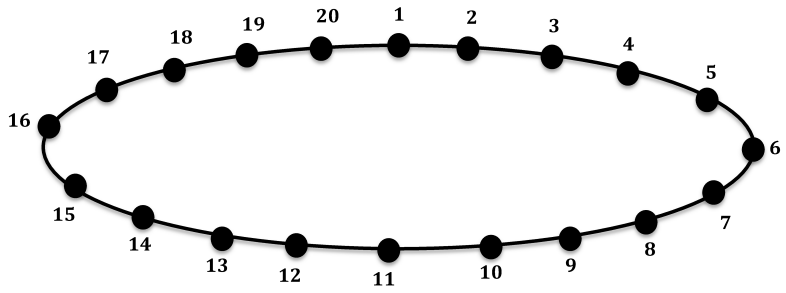


Figure 2.6: Visualisation of vortex point numbering

Below is the same visualisation with added data to represent when the code is addressing itself to vortex point $j$.

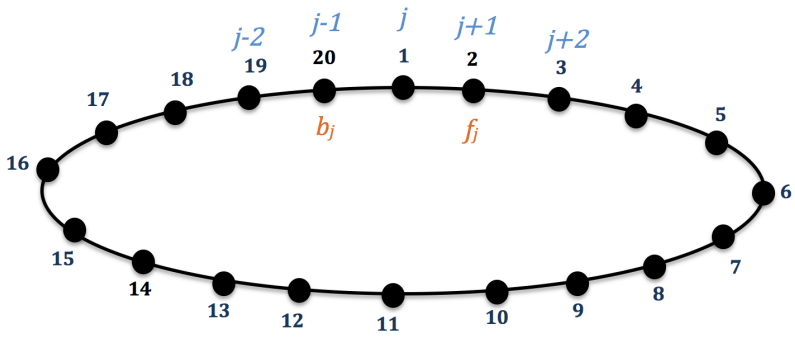


Figure 2.7: Visualisation of vortex point index numbering

The table below is a snapshot of part of the data

| $j$ | $s_{j,x}$ | $s_{j,y}$ | $s_{j,z}$ | $f_j$ | $b_j$ | ... |
|---|---|---|---|---|---|---|
| 1 | 2 | 0 | 0 | 2 | 20 | |
| 2 | 1.9 | 0.6 | 0 | 3 | 1 | |
| ⋮ | | | | | | |
| 19 | 1.6 | -1.2 | 0 | 20 | 18 | |
| 20 | 1.9 | -0.6 | 0 | 1 | 19 | |

### 2.3.3 A walk through the code

Qvort itself is a hugely complex and intricate code and in this section I have identified the key steps required to perform a simulation. The following algorithm represents an overview of the procedure we step through in the code:-

```
Setup or read in initial condition ;
for each time step n = 1 to N do
    for each vortex point j do
        Calculate the superfluid velocity v_{s_j} ;
        Calculate the normal fluid velocity v_n ;
        Combine velocities in Schwarz equation ;
    end
    for each vortex point j do
        Calculate the new position of j using Adams-Bashforth ;
    end
    Re-mesh by inserting vortex points if they have moved more than δ apart ;
    Reconnect vortex points where necessary ;
    Re-mesh by removing vortex points if they have become closer than δ/2 away ;
    Enforce periodic boundary conditions ;
    Increment the time t = t + dt ;
end
```

**Algorithm 1:** Basic steps taken within the code. Note: In this and all subsequent algorithms the coloured text is used to identify mathematical equations and the black text explains methodolgy.

Each of these steps warrants a section of its own in order to appreciate what calculations are required.

## 2.4 Time-stepping

The code uses a fixed time-interval $\Delta t$ with a prescribed number of iterations $N$. We utilise the $3^{rd}$ order Adams-Bashforth method to re-position the vortex points at each iteration. This method requires that for the calculation of the new position $\mathbf{s}_j^{n+1}$ for a given vortex point $\mathbf{s}_j^n$ (where $n$ refers to the time, i.e. $t_n = n\Delta t$ where $n = 0, 1, \ldots, N$.), the velocity from the two previous time intervals $\mathbf{v}_j^{n-1}$ and $\mathbf{v}_j^{n-2}$ are known.

This clearly gives rise to two exception conditions which have to be addressed, these being the very first step where there is no previous data available and the second step where we only have the velocity from the first step.

- First Step:
  For the initial time-step the lower order Euler Scheme is used whereby only the

current position and velocity of a vortex point are required to calculate the new position, the recursion formula for this is given by:

$$\mathbf{s}_j^{n+1} = \mathbf{s}^n + \Delta t \mathbf{v}_j^n. \tag{2.30}$$

- Second Step:
  When we encounter the difficulty on the second time around the time-stepping loop, in this instance a lower order Adams-Bashforth scheme is implemented where the recursion formula takes the form:

$$\mathbf{s}_j^{n+1} = \mathbf{s}_j^n + \frac{\Delta t}{2}(3\mathbf{v}_j^n - \mathbf{v}_j^{n-1}). \tag{2.31}$$

- Third and all subsequent steps:
  Once we have two previous velocities stored for a point we can move on to use the $3^{rd}$ order Adams-Bashforth method:-

$$\mathbf{s}_j^{n+1} = \mathbf{s}_j^n + \frac{\Delta t}{12}(23\mathbf{v}_j^n - 16\mathbf{v}_j^{n-1} + 5\mathbf{v}_j^{n-2}). \tag{2.32}$$

This can be derived in the following way. We begin with an equation of the form $\mathbf{s}' = \mathbf{v}(t, \mathbf{s})$ where we wish to know the value of $\mathbf{s}$ at the next time-step i.e.

$$\mathbf{s}(t_{n+1}) = \mathbf{s}(t_n) + \int_{t_n}^{t_{n+1}} \mathbf{s}'(t)dt, \tag{2.33}$$

$$= \mathbf{s}(t_n) + \int_{t_n}^{t_{n+1}} \mathbf{v}(t, \mathbf{s})dt. \tag{2.34}$$

To perform this integration we use a Lagrangian interpolation polynomial $p(t)$ where $p$ is a good approximation to $\mathbf{v}$. An interpolant polynomial of degree $d-1$ will incur an error of order $d$ and therefore when we substitute $p$ in to our integral the Adams-Bashforth method will be of order $d$. So for the 3-step Adams-Bashforth method we require an interpolant of degree 2 which passes through $\mathbf{v}^n$, $\mathbf{v}^{n-1}$ and $\mathbf{v}^{n-2}$. As a result we now need only consider the following equation which can be solved directly:

$$\mathbf{s}(t_{n+1}) = \mathbf{s}(t_n) + \int_{t_n}^{t_{n+1}} p(t)dt, \tag{2.35}$$

where

$$p(t) = \sum_{i=0}^{2} \mathbf{v}^{n-i}\ell_i \tag{2.36}$$

$$= \mathbf{v}^n\ell_0 + \mathbf{v}^{n-1}\ell_1 + \mathbf{v}^{n-2}\ell_2, \tag{2.37}$$

where $\ell_i$ are Lagrange basis polynomials defined in the following way:

$$\ell_i = \prod_{\substack{0\leq m\leq 2\\ m\neq i}} \frac{t - t_{n-m}}{t_i - t_{n-m}}. \tag{2.38}$$

Substituting this back in to $p$ gives:

$$p(t) = \mathbf{v}^n \frac{t-t_{n-1}}{t_n - t_{n-1}}\frac{t-t_{n-2}}{t_n - t_{n-2}} + \mathbf{v}^{n-1}\frac{t-t_n}{t_{n-1}-t_n}\frac{t-t_{n-2}}{t_{n-1}-t_{n-2}} + \mathbf{v}^{n-2}\frac{t-t_n}{t_{n-2}-t_n}\frac{t-t_{n-1}}{t_{n-2}-t_{n-1}}. \tag{2.39}$$

Now since $t_n$, $t_{n-1}$, and $t_{n-2}$ are all equally spaced we can say $t_n - t_{n-1} = t_{n-1} - t_{n-2} = \Delta t$, this gives:-

$$p(t) = \mathbf{v}^n \frac{t-t_{n-1}}{\Delta t}\frac{t-t_{n-2}}{2\Delta t} + \mathbf{v}^{n-1}\frac{t-t_n}{-\Delta t}\frac{t-t_{n-2}}{\Delta t} + \mathbf{v}^{n-2}\frac{t-t_n}{-2\Delta t}\frac{t-t_{n-1}}{-\Delta t} \tag{2.40}$$

$$= \frac{\mathbf{v}^n}{2\Delta t^2}(t-t_{n-1})(t-t_{n-2}) - \frac{\mathbf{v}^{n-1}}{\Delta t^2}(t-t_n)(t-t_{n-2}) + \frac{\mathbf{v}^{n-2}}{2\Delta t^2}(t-t_n)(t-t_{n-1}). \tag{2.41}$$

Substituting $p$ back in to our integral and splitting the integral out gives:

$$\begin{aligned}\int_{t_n}^{t_{n+1}} p(t)dt =& \frac{\mathbf{v}^n}{2\Delta t^2}\int_{t_n}^{t_{n+1}}(t-t_{n-1})(t-t_{n-2})dt - \frac{\mathbf{v}^{n-1}}{\Delta t^2}\int_{t_n}^{t_{n+1}}(t-t_n)(t-t_{n-2})dt \\ &+ \frac{\mathbf{v}^{n-2}}{2\Delta t^2}\int_{t_n}^{t_{n+1}}(t-t_n)(t-t_{n-1})dt.\end{aligned} \tag{2.42}$$

Each integral can now be evaluated in turn ...

$$\frac{\mathbf{v}^n}{2\Delta t^2}\int_{t_n}^{t_{n+1}}(t-t_{n-1})(t-t_{n-2})dt = \frac{\mathbf{v}^n}{2\Delta t^2}\left(\frac{23}{6}\Delta t^3\right) = \frac{23\Delta t}{12}\mathbf{v}^n, \tag{2.43}$$

$$-\frac{\mathbf{v}^{n-1}}{\Delta t^2}\int_{t_n}^{t_{n+1}}(t-t_n)(t-t_{n-2})dt = -\frac{\mathbf{v}^{n-1}}{\Delta t^2}\left(\frac{4}{3}\Delta t^3\right) = \frac{-4\Delta t}{3}\mathbf{v}^{n-1}, \tag{2.44}$$

$$\frac{\mathbf{v}^{n-2}}{2\Delta t^2}\int_{t_n}^{t_{n+1}}(t-t_n)(t-t_{n-1})dt = \frac{\mathbf{v}^{n-2}}{2\Delta t^2}\left(\frac{5}{6}\Delta t^3\right) = \frac{5\Delta t}{12}\mathbf{v}^{n-2}. \tag{2.45}$$

Finally, substituting all of these solutions back in gives us our final recursion equation:

$$\mathbf{s}^{n+1} = \mathbf{s}^n + \frac{\Delta t}{12}(23\mathbf{v}^n - 16\mathbf{v}^{n-1} + 5\mathbf{v}^{n-2}). \tag{2.46}$$

## 2.5 Evaluating the Spatial Derivatives

In order to evaluate the self-induced superfluid velocity at a point $\mathbf{s}_j$ either by means of the fully non-local Biot-Savart calculation or by the Local Induction Approximation, we need to obtain values for the first and second derivates $\mathbf{s}'_j$ and $\mathbf{s}''_j$ with respect to the arc length $\xi$. Given that the distances between adjacent vortex points can vary between $\delta$ and $\delta/2$, we need a method for obtaining the first and second order derivatives, $\mathbf{s}'$ and $\mathbf{s}''$, that is sufficiently accurate for the purpose. It was established by Gamet *et al.* [1999] that using a fourth order finite difference scheme provides the necessary values.

The arc lengths of the necessary pairs of adjacent points are denoted:
$\ell_{j-1} = |\mathbf{s}_{j-1} - \mathbf{s}_{j-2}|$,
$\ell_j \quad = |\mathbf{s}_j - \mathbf{s}_{j-1}|$,
$\ell_{j+1} = |\mathbf{s}_{j+1} - \mathbf{s}_j|$,
$\ell_{j+2} = |\mathbf{s}_{j+2} - \mathbf{s}_{j+1}|$.
Such that the fourth order finite difference scheme gives us the first derivative to be:

$$\mathbf{s}'_j = A_{1j}\mathbf{s}_{j-2} + B_{1j}\mathbf{s}_{j-1} + C_{1j}\mathbf{s}_j + D_{1j}\mathbf{s}_{j+1} + E_{1j}\mathbf{s}_{j+2}, \tag{2.47}$$

where the coefficients $A_{1j}$, $B_{1j}$, $C_{1j}$, $D_{1j}$ and $E_{1j}$ are given by,

$$A_{1j} = \frac{\ell_j\ell_{j+1}^2 + \ell_j\ell_{j+1}\ell_{j+2}}{\ell_{j-1}(\ell_{j-1}+\ell_j)(\ell_{j-1}+\ell_j+\ell_{j+1})(\ell_{j-1}+\ell_j+\ell_{j+1}+\ell_{j+2})}, \tag{2.48}$$

$$B_{1j} = \frac{-\ell_{j-1}\ell_{j+1}^2 - \ell_j\ell_{j+1}^2 - \ell_{j-1}\ell_{j+1}\ell_{j+2} - \ell_j\ell_{j+1}\ell_{j+2}}{\ell_{j-1}\ell_j(\ell_j+\ell_{j+1})(\ell_j+\ell_{j+1}+\ell_{j+2})}, \tag{2.49}$$

$$C_{1j} = -(A_{1j} + B_{1j} + D_{1j} + E_{1j}), \tag{2.50}$$

$$D_{1j} = \frac{\ell_{j-1}\ell_j\ell_{j+1} + \ell_j^2\ell_{j+1} + \ell_{j-1}\ell_j\ell_{j+2} + \ell_j^2\ell_{j+2}}{\ell_{j+1}\ell_{j+2}(\ell_j+\ell_{j+1})(\ell_{j-1}+\ell_j+\ell_{j+1})}, \tag{2.51}$$

$$E_{1j} = \frac{-\ell_{j+1}\ell_j^2 - \ell_{j-1}\ell_j\ell_{j+1}}{\ell_{j+2}(\ell_{j+1}+\ell_{j+2})(\ell_j+\ell_{j+1}+\ell_{j+2})(\ell_{j-1}+\ell_j+\ell_{j+1}+\ell_{j+2})}. \tag{2.52}$$

Similarly the second derivative is defined to be:

$$\mathbf{s}_j'' = A_{2j}\mathbf{s}_{j-2} + B_{2j}\mathbf{s}_{j-1} + C_{2j}\mathbf{s}_j + D_{2j}\mathbf{s}_{j+1} + E_{2j}\mathbf{s}_{j+2}, \tag{2.53}$$

where the coefficients $A_{2j}$, $B_{2j}$, $C_{2j}$, $D_{2j}$ and $E_{2j}$ are given by

$$A_{2j} = \frac{2[-2\ell_j\ell_{j+1} + \ell_{j+1}^2 - \ell_j\ell_{j+2} + \ell_{j+1}\ell_{j+2}]}{\ell_{j-1}(\ell_{j-1}+\ell_j)(\ell_{j-1}+\ell_j+\ell_{j+1})(\ell_{j-1}+\ell_j+\ell_{j+1}+\ell_{j+2})}, \tag{2.54}$$

$$B_{2j} = \frac{2[2\ell_{j-1}\ell_{j+1} + 2\ell_j\ell_{j+1} - \ell_{j+1}^2 + \ell_{j-1}\ell_{j+2} + \ell_j\ell_{j+2} - \ell_{j+1}\ell_{j+2}]}{\ell_{j-1}\ell_j(\ell_j+\ell_{j+1})(\ell_j+\ell_{j+1}+\ell_{j+2})}, \tag{2.55}$$

$$C_{2j} = -(A_{2j} + B_{2j} + D_{2j} + E_{2j}), \tag{2.56}$$

$$D_{2j} = \frac{2[-\ell_{j-1}\ell_j - \ell_j^2 + \ell_{j-1}\ell_{j+1} + 2\ell_j\ell_{j+1} + \ell_{j-1}\ell_{j+2} + 2\ell_j\ell_{j+2}]}{\ell_{j+1}\ell_{j+2}(\ell_j+\ell_{j+1})(\ell_{j-1}+\ell_j+\ell_{j+1})}, \tag{2.57}$$

$$E_{2j} = \frac{2[\ell_{j-1}\ell_j + \ell_j^2 - \ell_{j-1}\ell_{j+1} - 2\ell_j\ell_{j+1}]}{\ell_{j+2}(\ell_{j+1}+\ell_{j+2})(\ell_j+\ell_{j+1}+\ell_{j+2})(\ell_{j-1}+\ell_j+\ell_{j+1}+\ell_{j+2})}. \tag{2.58}$$

Note that if the distances between adjacent vortex points were to be uniformly equal such that $\ell_{j-1} = \ell_j = \ell_{j+1} = \ell_{j+2} = h$, then the above expressions reduce to familiar finite-difference schemes for a uniform mesh:

$$\mathbf{s}_j' = \frac{1}{12h}(\mathbf{s}_{j-2} - 8\mathbf{s}_{j-1} + 8\mathbf{s}_{j+1} - \mathbf{s}_{j+2}) + \mathcal{O}(h^4), \tag{2.59}$$

$$\mathbf{s}_j'' = \frac{1}{12h^2}(-\mathbf{s}_{j-2} + 16\mathbf{s}_{j-1} - 30\mathbf{s}_j + 16\mathbf{s}_{j+1} - \mathbf{s}_{j+2}) + \mathcal{O}(h^4). \tag{2.60}$$

## 2.6 Computing the Superfluid Velocity

If all things were equal, then the Biot-Savart method would be the obvious choice, however there are times when it's prudent to forego the accuracy of Biot-Savart for the speed of the LIA. As a guide the increased effort to compute additional points $P$ in the LIA is linear whereas with Biot-Savart it is quadratic. Whichever approach is adopted we need values for the first and second derivatives $\mathbf{s}_j'$ and $\mathbf{s}_j''$ which are calculated as per the equations described in section 2.5.

### 2.6.1 Computing the Biot-Savart Integral

In section 2.2.1 we derived the fully non-local Biot-Savart equation, however equation 2.25 is not the form which we implement within our code.

Given that our model already represents a vortex curve as a series of suitably small

straight lines we are able to perform the integration of the nonlocal component by splitting the integral into discrete parts which give the contribution to the velocity at the point $\mathbf{s}_j$ from the straight line segment between $\mathbf{s}_i$ and $\mathbf{s}_{i+1}$ to be

$$\mathbf{v}_s^{non}(\mathbf{s}_j)^i = \frac{\kappa}{2\pi(4ac-b^2)}\left(\frac{2c+b}{(a+b+c)^{1/2}} - \frac{b}{a^{1/2}}\right)(\mathbf{s}_i - \mathbf{s}_j) \times (\mathbf{s}_{i+1} - \mathbf{s}_i). \tag{2.61}$$

If we then sum all of these small segments (except those directly connected with $j$) we obtain the total nonlocal velocity at the point $\mathbf{s}_j$:-

$$\mathbf{v}_s^{non}(\mathbf{s}_j) = \sum_i \frac{\kappa}{2\pi(4ac-b^2)}\left(\frac{2c+b}{(a+b+c)^{1/2}} - \frac{b}{a^{1/2}}\right)(\mathbf{s}_i - \mathbf{s}_j) \times (\mathbf{s}_{i+1} - \mathbf{s}_i), \tag{2.62}$$

where $i$ loops over every vortex point except $j$ and its two adjacent points and $a = |\mathbf{s}_j - \mathbf{s}_i|^2$, $b = 2(\mathbf{s}_i - \mathbf{s}_j) \cdot (\mathbf{s}_{i+1} - \mathbf{s}_i)$ and $c = |\mathbf{s}_{i+1} - \mathbf{s}_i|^2$.

We now have an analytical solution of the Biot-Savart integral which can be directly implemented within the code without the need for any form of numerical integration such as Riemann Integration or Trapezoidal Integration. The algorithm below highlights the general process for implementation:-

Calculate first derivative $\mathbf{s}'_j$ ;
Calculate second derivative $\mathbf{s}''_j$ ;
Calculate the local component of the velocity $\mathbf{v}^{loc}_{s_j}$ ;
$\beta = \kappa/(4\pi)\log(2\sqrt{(\mathbf{s}_j - \mathbf{s}_{j+1})(\mathbf{s}_j - \mathbf{s}_{j-1})}/e^{1/2}a_0)$ ;
$\mathbf{v}^{loc}_{s_j} = \beta\ \mathbf{s}'_j \times \mathbf{s}''_j$ ;
**for** *each vortex point* $i$ **do**
  **if** $i$ *is not 'local' to* $j$ $i \neq j, j+1, j-1$ **then**
    Calculate the nonlocal component of the velocity $\mathbf{v}^{non}_{s_j}$ ;
    $a = |\mathbf{s}_j - \mathbf{s}_i|^2$ ;
    $b = 2(\mathbf{s}_i - \mathbf{s}_j)\cdot(\mathbf{s}_{i+1} - \mathbf{s}_i)$ ;
    $c = |\mathbf{s}_{i+1} - \mathbf{s}_i|^2$ ;
    $\mathbf{v}^{non}_{s_j} = \frac{\kappa}{2\pi(4ac-b^2)}\left(\frac{2c+b}{(a+b+c)^{1/2}} - \frac{b}{a^{1/2}}\right)(\mathbf{s}_i - \mathbf{s}_j)\times(\mathbf{s}_{i+1} - \mathbf{s}_i)$ ;
    Combine the local & nonlocal components to form the total superfluid velocity $\mathbf{v}_{s_j}$ ;
    $\mathbf{v}_{s_j} = \mathbf{v}^{loc}_{s_j} + \mathbf{v}^{non}_{s_j}$ ;
  **end**
**end**
**if** *using periodic boundaries* **then**
  Get additional nonlocal velocity from periodic wrap ; `/* See Algorithm 7 */`
**end**

**Algorithm 2:** Procedure for calculating the Biot-Savart velocity

The described methodology and its implementation have been widely reviewed and tested, details of which can be found [Baggaley, 2012; Baggaley & Barenghi, 2011*a*; Hanninen & Baggaley, 2014; Adachi *et al.*, 2010].

### 2.6.2 Computing the Local Induction Approximation

Once it is established that the superfluid velocity is to be calculated using the local induction approximation the following procedure is implemented within the code for vortex point $\mathbf{s}_j$:-

Calculate first derivative $\mathbf{s}'_j$ ;
Calculate second derivative $\mathbf{s}''_j$ ;
Calculate the local radius of curvature ;
$\mathcal{R} = 1/\mathcal{C} = 1/\sqrt{\mathbf{s}''_j \cdot \mathbf{s}''_j}$ ;
Calculate $\beta$ ;
$\beta = \kappa/(4\pi)\log(\mathcal{R}/a_0)$ ;
Calculate LIA velocity ;
$\mathbf{v}_s = \beta\ \mathbf{s}'_j \times \mathbf{s}''_j$ ;

**Algorithm 3:** Procedure for LIA

## 2.7 The Normal Fluid Velocity

There are numerous approaches to the modelling of the normal fluid velocity $\mathbf{v}_n$. Not one is an obvious choice regardless of computational power available, rather they each have their strengths and weaknesses depending on what it is we are trying to model. The two principle models we deploy are Counterflow and a Kinetic Simulation (KS) flow. Typically we use Counterflow when we are modelling physical experimentalists where they use a heat source to drive a 'thermal' flow [Vinen, 1957*b*, 1958, 1957*c*,*a*], KS flow is more suited to model experiments where there is thought to be a 'turbulent' normal fluid such as when the fluid is stirred with a grid [Maurer & Tabeling, 1998; Salort *et al.*, 2010].

The properties of the superfluid tangles ultimately created, are quite different dependent upon the choice of normal fluid modelling. Even where parameters have been chosen so as to produce similar line densities, and average curvatures, when 'viewed' in depth, the structures are vastly different.

### 2.7.1 Counterflow

Where our chosen model is to be counterflow (thermal counterflow which is the most used model in the literature from the pioneering work of Schwarz [1988] to the recent calculations of Tsubota and collaborators [Adachi *et al.*, 2010].) we simulate a flow in our normal fluid arising through convection from a uniformly distributed heat source at one end of our experimental closed channel. We assume our flow to be away from the boundaries of the channel where friction might induce a 'drag' effect which would prevent a uniform cross section of flow being present, although we do not model profiles such as the Poiseuille profile this has been done by others [Baggaley & Laurie, 2015; Yui & Tsubota, 2014]. We need also to be mindful that with an increasing heat flux $\dot{Q}$, the tendency towards turbulence arising within it increases and again produce a non linear cross section of flow

[Melotte & Barenghi, 1998; Guo *et al.*, 2010].

Our model imposes a uniform normal fluid velocity $\mathbf{v}_n^{ext} = V_n\hat{\mathbf{x}}$, this flow being away from the heat source which we designate as being in the x-direction, and proportional to the applied heat flux $V_n = \dot{Q}/(\rho ST)$, where $S$ is the specific entropy and $T$ is the temperature. To conserve mass the superfluid velocity is then given by $\mathbf{v}_s^{ext} = -(\rho_n/\rho_s)V_n\hat{\mathbf{x}}$ in the opposite direction to $\mathbf{v}_s^{ext}$. It is convenient for us to solve our equations of motion (Eqs. (2.1) and (2.15)) in this imposed superflow's reference frame, therefore we ultimately set $\mathbf{v}_s^{ext} = 0$ such that our counterflow velocity is given by $v_{ns} = |\mathbf{v}_n^{ext} - \mathbf{v}_s^{ext}| = \dot{Q}/(\rho_s ST)$.

### 2.7.2 The KS Flow

At the time when the Navier-Stokes Equation was first formulated there was zero computing power to prove it and much less to make use of it. Even today with the ready availability of formidable computing power, we are forced to find ways to approximate the full Navier-Stokes Equation as the time taken to compute the vast number of iterations required to model even the simplest of real world flows is unacceptably long.

To allow the numerical simulation of flows without the computational overhead of a full Navier-Stokes implementation, a numerical model was developed by Fung *et al.* [1992]. This is a Lagrangian model which uses KS to model turbulence. This has since been widely tested and has proven to be in good agreement with other numerical schemes, such as DNS as well as physical experiments [Osborne *et al.*, 2006; Fung & Vassilicos, 1998; Malik & Vassilicos, 1999].

For simulating a KS flow our model builds on the work of Fung and Osborne [Fung *et al.*, 1992; Osborne *et al.*, 2006], and is adapted by Baggaley [Baggaley, 2009] in particular to introduce periodicity. In physical flows we observe large eddies which dissipate through a cascade to smaller eddies and so on. When we seek to model this we model each of the eddy sizes (turbulent modes) separately such that they are mutually independent and none of the modelling is reductive whereby a given size eddy dissipates in to a number of smaller sized eddies.

In our model the flow velocity is built by aggregating blocks of independent turbulent modes which are then each modelled by a Fourier mode. The summation of these independent and randomly orientated Fourier modes prescribes our velocity. At a time $t$ for a given point $\mathbf{x}$ the velocity is given by:

$$\mathbf{v}_n(\mathbf{x},t) = \sum_{n=1}^{N} \left(\mathbf{A}_n \times \mathbf{k}_n \cos(\mathbf{k}_n \cdot \mathbf{x} + \omega_n t) + \mathbf{B}_n \times \mathbf{k}_n \sin(\mathbf{k}_n \cdot \mathbf{x} + \omega_n t)\right), \tag{2.63}$$

where $N$ is the number of Fourier modes and $\omega_n$ is the unsteadiness frequency. The decomposition coefficients $\mathbf{A}_n$ and $\mathbf{B}_n$ correspond to the wave vector $\mathbf{k}_n$ given by

$$\mathbf{k}_n = k_n \hat{\mathbf{k}}_n, \tag{2.64}$$

which is randomly orientated by the assignment of a random unit vector $\hat{\mathbf{k}}_n$. The distribution of the wave numbers is given by

$$k_n = k_1 \left(\frac{k_N}{k_1}\right)^{(n-1)/(N-1)}. \tag{2.65}$$

The principles of our modelling require that the Fourier modes are randomly orientated and that the velocity field satisfies incompressibility. To ensure these criteria are met we independently and randomly select the orientations of $\mathbf{A}_n$ and $\mathbf{B}_n$ under the constraint that they are in a plane at right angles to $\hat{\mathbf{k}}_n$ i.e. $\mathbf{A}_n \cdot \hat{\mathbf{k}}_n = \mathbf{B}_n \cdot \hat{\mathbf{k}}_n = 0$.

A key feature of this model is that we can prescribe the energy spectrum as:

$$E(k) = k^4 (1 + k^2)^{-(2+p/2)} e^{-1/2(k/k_N)^2}. \tag{2.66}$$

In the inertial range (where $1 \ll k \ll k_N$) this equation reduces to $E(k) \propto k^{-p}$ and so clearly if $p = 5/3$ then we will have prescribed the Kolmogorov spectrum. We choose the magnitudes of $\mathbf{A}_n$ and $\mathbf{B}_n$ such that the prescribed energy spectrum is satisfied,

$$|\mathbf{A}_n \times \hat{\mathbf{k}}_n| = A_n, \tag{2.67}$$

$$A_n = B_n = \sqrt{\frac{2E(k_n)\Delta k_n}{3}}, \tag{2.68}$$

where $\Delta k_n$ is given by

$$\Delta k_n = \begin{cases} \dfrac{k_2 - k_1}{2}, & n = 1, \\ \dfrac{k_{n+1} - k_{n-1}}{2}, & 1 < n < N, \\ \dfrac{k_N - k_{N-1}}{2}, & n = N. \end{cases} \tag{2.69}$$

The above ensures that the following is true:

$$\frac{1}{V}\int_V \frac{1}{2}|\mathbf{u}|^2 dV = \int_0^\infty E(k)dk \sim \sum_{n=1}^{N} E(k_n)\Delta k_n. \tag{2.70}$$

To ensure that the flow shall vary over time we introduce a time-dependence through the unsteadiness frequency. For each mode $n$, $\omega_n$ is proportional to the eddy turnover frequency:

$$\omega_n = \sqrt{k_n^3 E(k_n)}. \tag{2.71}$$

In order to force a truly isotropic distribution of the wave vectors we write the unit vector $\hat{\mathbf{k}}_n$ as

$$\hat{\mathbf{k}}_n = \begin{pmatrix} \sqrt{1-\zeta_n^2}\cos\theta_n \\ \sqrt{1-\zeta_n^2}\sin\theta_n \\ \zeta_n \end{pmatrix}, \tag{2.72}$$

where, $\theta_n \in [0, 2\pi)$ and $\zeta_n \in [-1, 1]$, are uniformly distributed random numbers.

## 2.8 Remeshing

At the initial setup we have set the maximum distance that any two points can be apart as $\delta$ (the resolution). This choice of $\delta$ automatically sets the minimum distance that can exist between any two points as $\delta/2$. We need the ability to choose and vary resolutions depending on the needs of the particular simulation. If we wish to see fine detail on small artefacts (such as Kelvin Waves) then we need to set a high resolution i.e. small $\delta$, conversely if the nature of the simulation does not require the observation of fine detail or if indeed such fine detail would not exist (due to friction damping in relatively higher temperature simulation) then we can set a low resolution i.e. a large $\delta$.

Remeshing takes two forms each with distinct methodology; one deals with the insertion of extra points and the other with the removal of surplus points. The code evaluates each in turn in that order.

Firstly we deal with possible insertions:

**for** *each vortex point* $i$ **do**
  Check distance between current point and point in front ;
  $dist_i = \sqrt{(s(x)_i - s(x)_{i+1})^2 + (s(y)_i - s(y)_{i+1})^2 + (s(z)_i - s(z)_{i+1})^2}$ ;
  **if** *distance is greater than resolution* $dist_i > \delta$ **then**
    `/* We need to insert a new vortex point */`
    Get $2^{nd}$ derivative $\mathbf{s}_i''$ ;
    Calculate the curvature $\mathcal{C}$ ;
    $\mathcal{C} = \sqrt{\mathbf{s}_i'' \cdot \mathbf{s}_i''}$ ;
    **if** $\mathcal{C}$ *is above minimum curvature* $\mathcal{C} > 0.00001$ **then**
      Use interpolation including curvature to determine new point's location;
      $\mathcal{R} = 1/\mathcal{C}$ ; `/* Define the radius of curvature */`
      $\mathbf{s}_{new} = 0.5(\mathbf{s}_i + \mathbf{s}_{i+1}) + (\sqrt{\mathcal{R}^2 - (dist_i/2)^2} - \mathcal{R})\mathcal{R}\ \mathbf{s}''$ ;
    **else**
      `/* Point lies on more or less a straight line */`
      Use linear interpolation to determine new point's location ;
      $\mathbf{s}_{new} = 0.5(\mathbf{s}_i + \mathbf{s}_{i+1})$ ;
    **end**
    Define new point's velocity ;
    $\mathbf{v}_{new} = 0.5(\mathbf{v}_i + \mathbf{v}_{i+1})$ ;
    Set in-front and behind points of new point ;
    $behind_{\mathbf{s}_{new}} = \mathbf{s}_i$ ;
    $front_{\mathbf{s}_{new}} = \mathbf{s}_{i+1}$ ;
    Set new point as behind previous in-front ;
    $behind_{\mathbf{s}_{i+1}} = \mathbf{s}_{new}$ ;
    Set new point as in-front current point ;
    $front_{\mathbf{s}_i} = \mathbf{s}_{new}$ ;
  **end**
**end**

**Algorithm 4:** Procedure for Inserting a vortex point

Now we deal with possible removals:

**for** *each vortex point* $i$ **do**
  Check distance between current point and the point 2 in front ;
  $dist_{ii} = \sqrt{(s(x)_i - s(x)_{i+2})^2 + (s(y)_i - s(y)_{i+2})^2 + (s(z)_i - s(z)_{i+2})^2}$ ;
  **if** *distance is less than resolution* **then**
    `/* We must remove the point in front */`
    Set in-front of current point to be location of point 2 ahead ;
    $front_{\mathbf{s}_i} = \mathbf{s}_{i+2}$ ;
    Set behind of point 2 ahead to be current point ;
    $behind_{\mathbf{s}_{i+2}} = \mathbf{s}_i$ ;
    Clear the particle in front ;
  **end**
**end**

**Algorithm 5:** Procedure for Removing a vortex point

## 2.9 Reconnections

The systems we are trying to model have energy loss even at very low temperatures where there is no mutual friction between the vortices and the normal fluid. One mechanism for this loss is through the transformation of kinetic energy into acoustic energy during reconnections [Leadbeater *et al.*, 2001] but we also have losses through the elimination of small vortex rings and through phonon emissions.

It is impractical for us to model directly these energy loses, however all our reconnections result in a loss of line length and we use this loss to simulate the real world energy loss. We use our line length as a proxy for energy in the system as it is known that the energy is proportional to the length for a straight vortex and therefore we assume that the energy in our vortices is the length multiplied by the energy per unit length.

It has been shown experimentally that reconnections occur naturally when vortices come sufficiently close together [Paoletti *et al.*, 2010]. This is further borne out in microscopic models such as those based on the GPE [Koplik & Levine, 1993; Tebbs *et al.*, 2011; Kerr, 2011; Kursa *et al.*, 2011], however our reconnections must be 'hand made'. Inspired by the early work of Schwarz [1988] there are now numerous algorithms seeking to deal with the issue of reconnection. The principle candidates are examined in this study [Baggaley, 2012]. Our code implements the following...

For the determination of a reconnection there are three criteria to be evaluated.

- Closeness test
- Orientation test
- Line length reduction test

**for** *each vortex point* $i$ **do**
  Establish the closest point $j$ which is not either the point in front or behind ;
  **if** *distance between* $i$ *&* $j$ *is less than* $\delta/2$ **then**
    /* $i$ & $j$ pass the closeness test */
    Determine the relative orientation $\phi$ of $i$ and $j$ ;
    $\mathbf{s}'_i \cdot \mathbf{s}'_j = \phi$ ;
    **if** $i$ *and* $j$ *are not parallel(ish)* $\cos(\phi) < 0.9$ **then**
      /* $i$ & $j$ pass the orientation test */
      Check current line length before proposed reconnection ;
      Check what the line length would be after proposed reconnection ;
      **if** *length after is less than length before* **then**
        /* $i$ & $j$ pass line length test $\Rightarrow$ so will now reconnect $i$ & $j$ */
        Perform reconnection by reassigning relevant in front and behind values ;
        $front_{\mathbf{s}_{j-1}} = \mathbf{s}_{i+1}$ ;
        $behind_{\mathbf{s}_{i+1}} = \mathbf{s}_{j-1}$ ;
        $front_{\mathbf{s}_i} = \mathbf{s}_j$ ;
        $behind_{\mathbf{s}_j} = \mathbf{s}_i$ ;
        Check if either resultant loop is 5 points or less and if so remove ;
      **end**
    **end**
  **end**
**end**

**Algorithm 6:** Procedure for Reconnections

A schematic for this reconnection algorithm can be seen in Figure. 2.8.

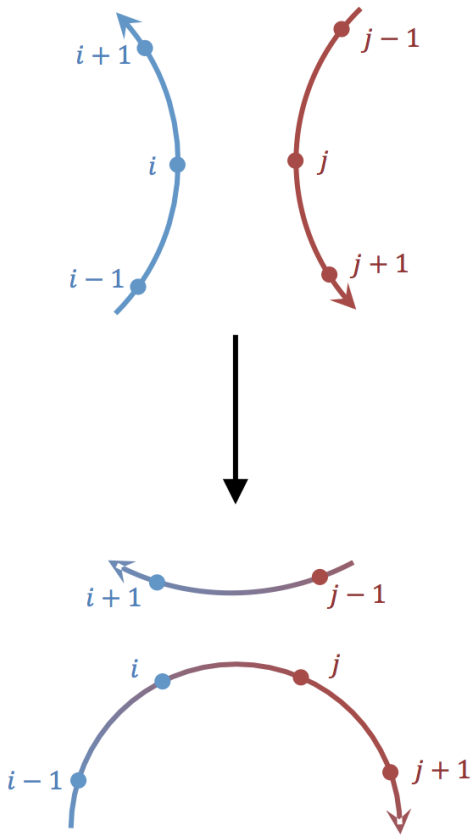


Figure 2.8: Reconnection visualisation. Once points $i$ and $j$ have been approved for reconnection (meet all criteria) the top is the topology of the vortices before the reconnection and the bottom is the topology after.

## 2.10 Periodic Boundaries

If we are to run the code with periodic boundaries, then when calculating the vortex point velocities we need to introduce the concept of 'Periodic Wrapping'. In essence this wrapping defines and limits the space frame within which we need to consider the effects on objects in the 'root cell' (the computational domain at the core of the wrapping) of all relevant other vortex points. This wrapping is achieved by fully enclosing the root cell with replications of itself known as copies on all its sides and corners.

The possibilities for the translation of the root cell whilst still retaining a minimum single point contact with itself is determined by a number of shifts of the root cell in cartesian space. In each of the 3 directions the box can shift by either $\pm D$ or not at all, this means there are 3 choices for each direction which gives 27 possible shifts all of which

must be accounted for except the null shift as this would result in a double counting of the root cell. This gives us a total of 26 copies surrounding the 1 original root cell. This also ensures that the minimum dimension of 'enclosure' of any point in the original root cell is the box size $D$, for the computational integrity of this model it is assumed that the nonlocal effects vortex points beyond size D distance are so small as to be negligible by either inclusion or omission. The distribution of 'tangles' within the copy cells are deemed to be identical to those in the original root cell.

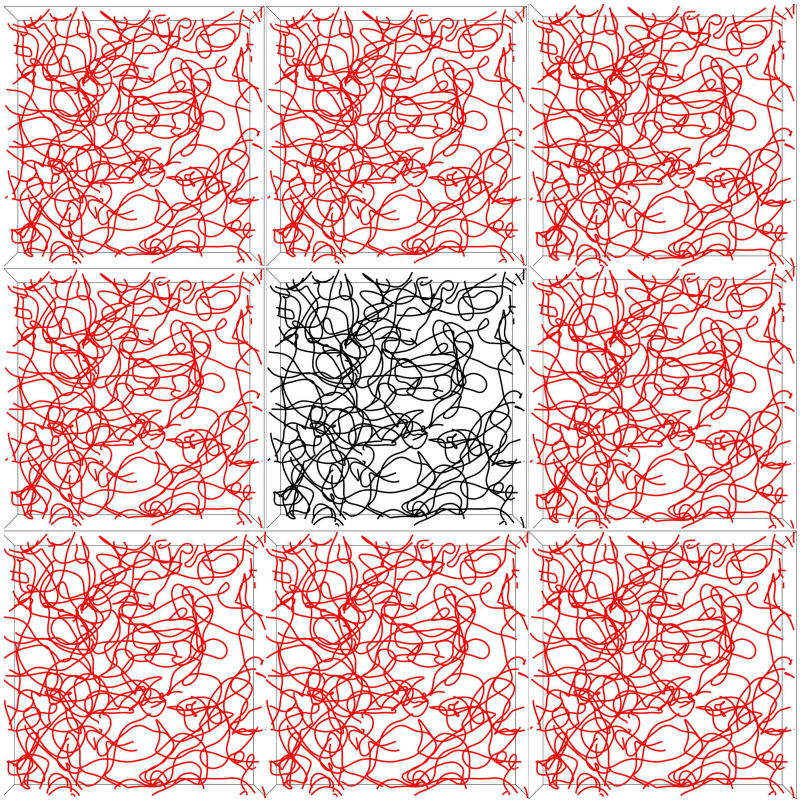

Figure 2.9: Visualisation of periodic wrapping with our original root cell (coloured black) surrounded by the 8 copies (coloured red)

The existence and influence of any vortex point within the 26 copy cell matrix is acknowledged in the mathematical computation of the superfluid velocity of each vortex point.

$$\mathbf{v}_s^{non}(\mathbf{s}_j) = \frac{\kappa}{4\pi} \oint_{\mathcal{L}_\mathcal{P}} \frac{(\mathbf{s}_j - \mathbf{r})}{|\mathbf{s}_j - \mathbf{r}|^3} \times \mathbf{dr} \tag{2.73}$$

Where $\mathcal{L}_\mathcal{P}$ is the vortex configuration within the copy cells. To implement this within the code the following algorithm is applied:-

**for** $r = 1 \dots 26$ **do** `/* where` $\mathbf{h}_r$ `are the 26 possible translations */`
  **for** *each vortex point* $i$ **do**
    Calculate the nonlocal velocity over the 26 copy cells ;
    $a = |\mathbf{s}_j - (\mathbf{s}_i + \mathbf{h}_r)|^2$ ;
    $b = 2((\mathbf{s}_i + \mathbf{h}_r) - \mathbf{s}_j) \cdot (\mathbf{s}_{i+1} - \mathbf{s}_i)$ ;
    $c = |\mathbf{s}_{i+1} - \mathbf{s}_i|^2$ ;
    $\mathbf{v}_{s_j}^{non} = \frac{\kappa}{2\pi(4ac-b^2)} \left( \frac{2c+b}{(a+b+c)^{1/2}} - \frac{b}{a^{1/2}} \right) ((\mathbf{s}_i + \mathbf{h}_r) - \mathbf{s}_j) \times (\mathbf{s}_{i+1} - \mathbf{s}_i)$ ;
    Add this in to the total superfluid velocity ;
    $\mathbf{v}_{s_j} = \mathbf{v}_{s_j}^{loc} + \mathbf{v}_{s_j}^{non}$ ;
  **end**
**end**

**Algorithm 7:** Procedure for calculating the nonlocal velocity component with Biot-Savart using periodic boundaries

For each vortex point $\mathbf{s}_j$ in the root cell, we have now established the Biot-Savart velocity as the combination of its local velocity with the additional influence of all other points in the root cell and its copies.

Our model does not allow the removal of vortex points by physical displacement. That is to say, should a vortex point exit our periodic box at a given time-step then it is

reintroduced on the other side of the box as detailed in Algorithm 8.

**for** *each vortex point* $i$ **do**
  `/* First look at the x-component of the position... */`
  **if** *it is now outside the RHS of the box* - $\mathbf{s}(x)_i > D/2$ **then**
    Reintroduce point on the LHS within our box ;
    $\mathbf{s}(x)_i = \mathbf{s}(x)_i - D$ ;
  **else if** *it is now outside the LHS of the box* - $\mathbf{s}(x)_i < -D/2$ **then**
    Reintroduce point on the RHS within our box ;
    $\mathbf{s}(x)_i = \mathbf{s}(x)_i + D$ ;
  **else**
    Current position is within bounds of box - do nothing ;
  **end**
  `/* Next look at the y-component of the position... */`
  **if** *it is now outside the front of the box* - $\mathbf{s}(y)_i > D/2$ **then**
    Reintroduce point at the back within our box ;
    $\mathbf{s}(y)_i = \mathbf{s}(y)_i - D$ ;
  **else if** *it is now outside the back of the box* - $\mathbf{s}(y)_i < -D/2$ **then**
    Reintroduce point at the front within our box ;
    $\mathbf{s}(y)_i = \mathbf{s}(y)_i + D$ ;
  **else**
    Current position is within bounds of box - do nothing ;
  **end**
  `/* Finally look at the z-component of the position... */`
  **if** *it is now outside the top of the box* - $\mathbf{s}(z)_i > D/2$ **then**
    Reintroduce point at the bottom within our box ;
    $\mathbf{s}(z)_i = \mathbf{s}(z)_i - D$ ;
  **else if** *it is now outside the bottom of the box* - $\mathbf{s}(z)_i < -D/2$ **then**
    Reintroduce point at the top within our box ;
    $\mathbf{s}(z)_i = \mathbf{s}(z)_i + D$ ;
  **else**
    Current position is within bounds of box - do nothing ;
  **end**
**end**

**Algorithm 8:** Procedure for enforcing periodic boundaries

## 2.11 The Tree Method

To calculate the effect a nonlocal vortex point has on our target vortex point requires one cycle of our Biot-Savart code. Clearly with a very high number of particles (possibly exceeding $10^5$) this can require a large number of cycles of the code (of the order $10^5 \times 10^5$). It would be advantageous to find a robust method whereby the number of cycles can be reduced with an acceptable sacrifice in accuracy. Astrophysicists dealing with the infinity of space had similar computational issues in tracking many millions of celestial objects. Barnes & Hut [1986] successfully deployed tree algorithms to reduce the computational load.

The influence of a nonlocal object is directly proportional to its distance away from the target vortex point. There comes a point when these nonlocal vortex points need no longer be considered as individual objects but rather can be treated as a group with other vortex points in their vicinity and the effect on the target can be an averaged value for this group.

If we choose a suitable reference framework whereby this averaging can be successfully implemented then it has been shown [Springel *et al.*, 2005] that tree algorithms can deliver the required accuracy with many fewer computational cycles.

The basic idea behind our tree algorithm is the division of our periodic box into ever smaller subsets of space and at each of these divisions calculating the total circulation and the centre of circulation for these subspaces. If we start with our periodic box, a cube of width $x$ then the first step in our tree algorithm is to divide this space up in to octets, these being cubes whose width is $x/2$. We do our calculations for these 8 cubes for the total circulation, given by

$$\mathbf{s}_\Sigma = \sum_{i=1}^{N_\mathrm{c}} (\mathbf{s}_{i+1} - \mathbf{s}_i). \tag{2.74}$$

where $N_c$ is the total number of points in the cube, and we then calculate the centre of circulation, given by:

$$\bar{\mathbf{s}} = \frac{1}{N_\mathrm{c}} \sum_{i=1}^{N_\mathrm{c}} \mathbf{s}_i. \tag{2.75}$$

Any cube which contains more than one vortex point ($N_c > 1$) will then be subdivided in to 8 smaller cubes of width $x/4$ and the process is repeated until every vortex point is contained within its own cube, at which point we will have completed our octree.

A single vortex point can therefore have a presence in a number of cubes of varying width; when calculating the effect a particular nonlocal vortex point has on our target

we need to decide which is the relevant cube for calculation purposes. We do this by setting a limiting parameter $\theta$ which is the ratio of the cube width $w$ to the distance of the centre of circulation for the cube containing our nonlocal point to the target point $d$ i.e. $\theta = w/d$. The key factor in the successful use of our tree algorithm is the limit to this ratio $\theta_{max}$: too large results in too much averaging and therefore an unacceptable loss in accuracy, too small and we tend to pure Biot-Savart which is computationally unsustainable.

The code is able to efficiently cascade through the tree by the use of pointers from each 'parent' cube to its 8 'child' cubes, and as it does so the cube width $w$ is halved and therefore the likelihood of that cube passing our limit test is doubled.

Only points defined to be 'close' based on our limiter ($w/d < \theta_{max}$) need be individually evaluated, others can be considered as range of single large vortex points which lie at the centre of circulation for each cube. The resultant time for the code to execute the tree's construction is of magnitude $N \log(N)$ (where $N$ is the total number of vortex points) as each point does not need comparing with every other point, such that the tree can comfortably be redrawn for each time-step. For clarity, Figure. 2.10 is a 2 dimensional representation of the grouping and subgrouping of vortex points down to the single vortex point level. Figure 2.11 illustrates how a vortex ring in our periodic cube is eventually contained within smaller cubes built by our octree.

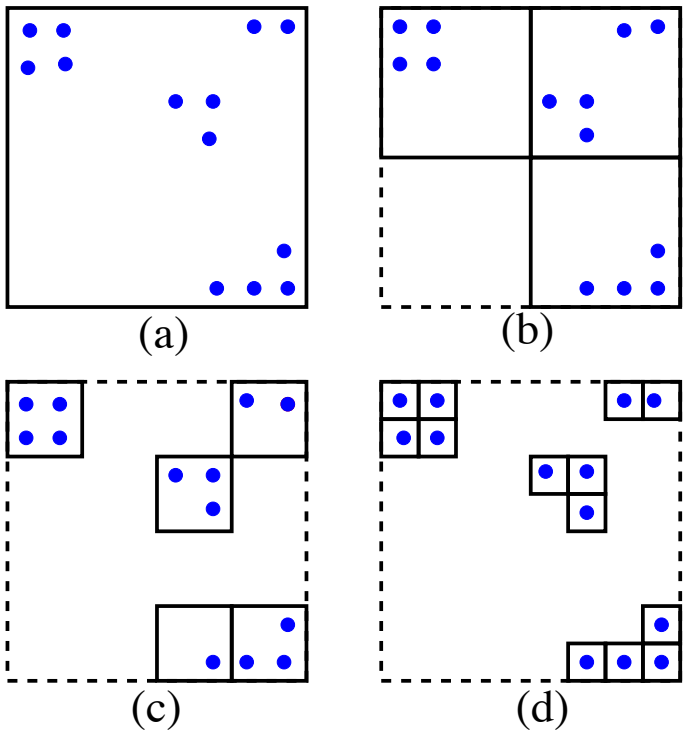


Figure 2.10: Illustration of the tree's construction in 2D. Panel (a) shows our periodic box containing 13 vortex points (in blue), panel (b) represents the effect of our halving the side length of our reference square resulting in four smaller squares, this 'halving' is repeated in panels (c) and (d) by which time we have a single point in each square. Image taken from [Baggaley & Barenghi, 2012].

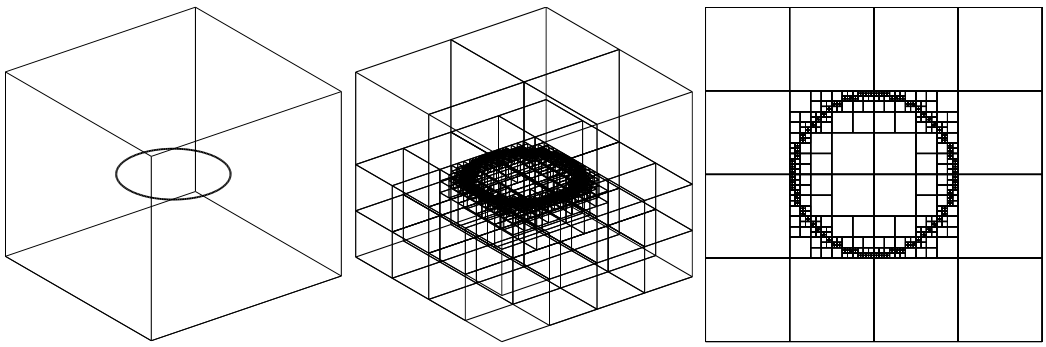

Figure 2.11: From left to right: 3D Illustrations of a vortex ring in our periodic cube and then when it is contained within the tree structure. Finally a 2D slice in the $xy$-plane through the centre of the ring (at $z = 0$) showing the partitioning of vortex points within their own 'cube'. Images taken from [Baggaley & Barenghi, 2012].

## 2.12 Basic Tests of the code

My adopted code has been widely tested and shown to be a very capable vehicle for the simulations I run. However, based on the principle that it's always best to pack your own parachute, I have separately and independently tested the code and I am satisfied the results agree with analytic tests.

### 2.12.1 The velocity of a vortex ring

It is well established [Barenghi & Donnelly, 2009; Donnelly, 1970] that a vortex ring moves with its own self induced velocity $\mathbf{v}_r$:

$$v_r = -\frac{\kappa}{4\pi r}\left[\ln\left(\frac{8r}{a_0}\right) - \frac{1}{2}\right], \tag{2.76}$$

where $\kappa$ is the quantum of circulation, $r$ is the radius of the ring and $a_0$ is the vortex core size.

In order to test this within my code I performed a series of seven simulations - all at zero temperature within a periodic box of size $D = 0.1$cm using the local induction approximation to calculate the self induced velocity of the vortex ring. I would initialise my code with a single vortex ring orientated in the $xy$-plane, each time using a progressively larger radius for the ring. Figure 2.12 highlights the progression of the ring sizes.

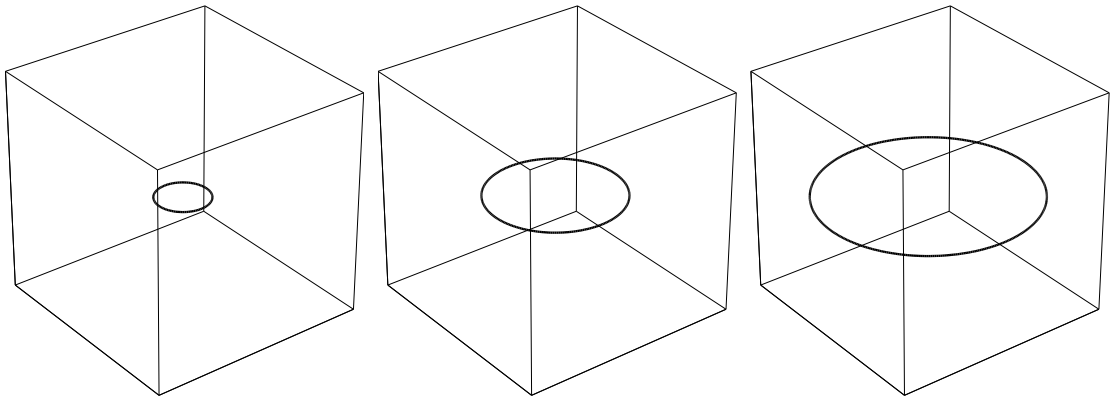

Figure 2.12: Left: The first and smallest vortex ring tested, with a radius $r = 1.19 \times 10^{-2}$cm, Middle: The fourth and 'middle' vortex ring tested, with a radius $r = 2.98 \times 10^{-2}$cm, Right: The last and largest vortex ring tested, with a radius $r = 4.77 \times 10^{-2}$cm.

For each simulation I would take note of the radius and velocity of the ring in order to compare my results with that of the analytical solution above. My results are shown in Figure 2.13.

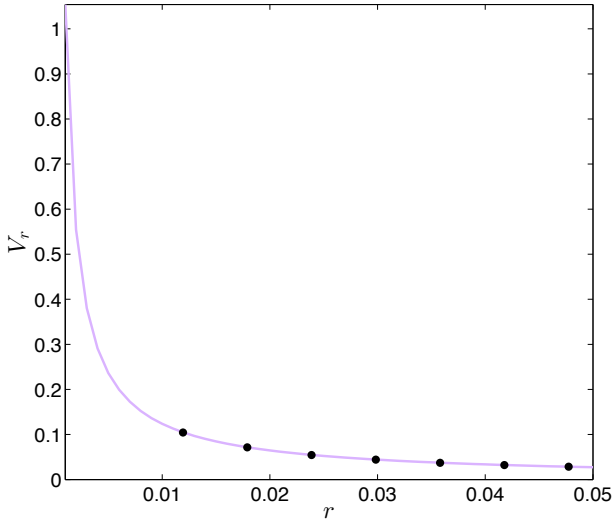


Figure 2.13: Plot of the z-component of the velocity, $V_r$ against the radius of the loop, $r$. The purple line is the expected result from the analytical derivation of the velocity (Eq. 2.76). The back circles are the measured velocities from the seven simulations run in the code.

It is clear from the above figure that my results (black circles) are in excellent agreement with the expected velocity (purple line) of a vortex ring.

### 2.12.2 The Donnelly-Glaberson Instability

As a further check of the integrity of the code, I set about trying to reproduce the known results of a flow past a slightly perturbed vortex (known as the Donnelly-Glaberson Instability).

To begin, we need to derive an analytical expression for the growth of the radius of the perturbations ($\epsilon$) over time so that we can compare this to the results generated within the code.

If we have a vortex line which is orientated in the x-direction and we give it a small helical perturbation (as shown on the left of Figure 2.14) then the position $\mathbf{s}$ along the vortex is given by:

$$\mathbf{s} = (x, \epsilon \cos\phi, \epsilon \sin\phi), \tag{2.77}$$

where $\phi = kx - \omega t$.

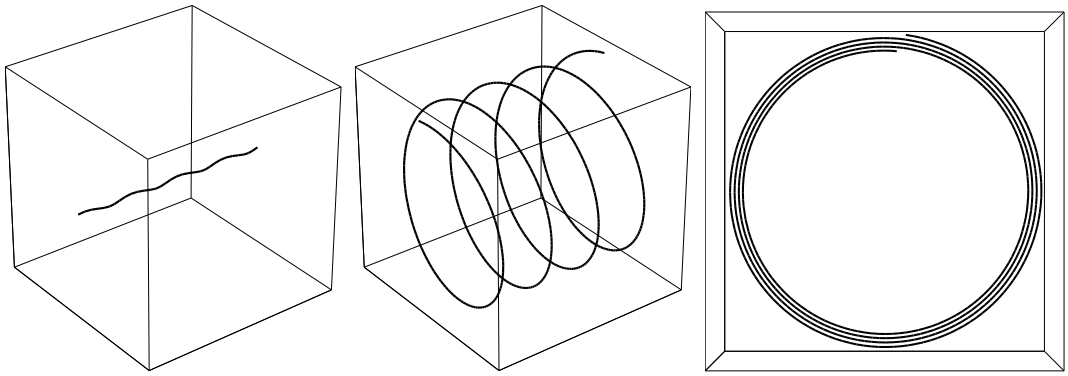

Figure 2.14: Left: Representation of the helix at the start, Middle: Representation of the helix after the perturbations have grown, Right: The grown helix shown in the yz-plane where the radius of the circles is $\epsilon$.

We can now differentiate $\mathbf{s}$ with respect to time to calculate the velocity which is given by $\mathrm{d}\mathbf{s}/\mathrm{dt}$:

$$\frac{\mathrm{d}\mathbf{s}}{\mathrm{d}t} = (0, \epsilon\omega \sin\phi + \frac{\mathrm{d}\epsilon}{\mathrm{d}t}\cos\phi, -\epsilon\omega\cos\phi + \frac{\mathrm{d}\epsilon}{\mathrm{d}t}\sin\phi). \tag{2.78}$$

This expression can be directly compared with the equation of motion we use within the code. If we use the local induction approximation to calculate the superfluid velocity (i.e. $\mathbf{v}_s^{self} = \beta\mathbf{s}' \times \mathbf{s}''$) our approximation for $\mathrm{d}\mathbf{s}/\mathrm{dt}$ will be:-

$$\frac{\mathrm{d}\mathbf{s}}{\mathrm{d}t} = \beta\mathbf{s}' \times \mathbf{s}'' + \alpha\mathbf{s}' \times [\mathbf{v}_n - \beta\mathbf{s}' \times \mathbf{s}'']. \tag{2.79}$$

Now if we substitute our $\mathbf{s}$ from above and assume a uniform flow past the vortex also in the x-direction, such that $\mathbf{v}_n = (V, 0, 0)$ we should be able to obtain an equation for $\mathrm{d}\epsilon/\mathrm{dt}$ and hence gain an expression for $\epsilon$ over time.

To do this we will need expressions for $\mathbf{s}'$ and $\mathbf{s}''$. A prime here denotes a derivative with respect to arc length which we can approximate as a derivative with respect to $x$ and therefore we obtain:

$$\mathbf{s}' = (1, -\epsilon k \sin\phi, \epsilon k \cos\phi), \tag{2.80}$$

$$\mathbf{s}'' = (0, -\epsilon k^2 \cos\phi, -\epsilon k^2 \sin\phi). \tag{2.81}$$

Using the above equations we can now calculate our expression for $\mathrm{d}\mathbf{s}/\mathrm{dt}$ using equation 2.79. To show how this is executed we will split the calculation up in to sections:

$$\mathbf{s}' \times \mathbf{s}'' = \begin{pmatrix} 1 \\ -\epsilon k \sin\phi \\ \epsilon k \cos\phi \end{pmatrix} \times \begin{pmatrix} 0 \\ -\epsilon k^2 \cos\phi \\ -\epsilon k^2 \sin\phi \end{pmatrix} = \begin{pmatrix} \epsilon^2 k^3 \\ \epsilon k^2 \sin\phi \\ -\epsilon k^2 \cos\phi \end{pmatrix}. \tag{2.82}$$

Building this up we have:

$$\begin{aligned} \mathbf{s}' \times (\mathbf{v}_n - \beta \mathbf{s}' \times \mathbf{s}'') &= \begin{pmatrix} 1 \\ -\epsilon k \sin\phi \\ \epsilon k \cos\phi \end{pmatrix} \times \left( \begin{pmatrix} V \\ 0 \\ 0 \end{pmatrix} - \beta \begin{pmatrix} \epsilon^2 k^3 \\ \epsilon k^2 \sin\phi \\ -\epsilon k^2 \cos\phi \end{pmatrix} \right) \\ &= \begin{pmatrix} 0 \\ (V - \beta\epsilon^2 k^3)\epsilon k \cos\phi - \beta\epsilon k^2 \cos\phi \\ (V - \beta\epsilon^2 k^3)\epsilon k \sin\phi - \beta\epsilon k^2 \sin\phi \end{pmatrix}. \end{aligned} \tag{2.83}$$

Linearising this in $\epsilon$ gives us (note by doing this our result will only hold in the limit of small $\epsilon$):

$$\mathbf{s}' \times (\mathbf{v}_n - \beta \mathbf{s}' \times \mathbf{s}'') = \begin{pmatrix} 0 \\ (V - \beta k)\epsilon k \cos\phi \\ (V - \beta k)\epsilon k \sin\phi \end{pmatrix}. \tag{2.84}$$

Hence we finally obtain our expression for $\mathrm{d}\mathbf{s}/\mathrm{d}t$:

$$\frac{\mathrm{d}\mathbf{s}}{\mathrm{d}t} = \beta \mathbf{s}' \times \mathbf{s}'' + \alpha \mathbf{s}' \times (\mathbf{v}_n - \beta \mathbf{s}' \times \mathbf{s}'') = \begin{pmatrix} 0 \\ \beta\epsilon k^2 \sin\phi + (V - \beta k)\alpha\epsilon k \cos\phi \\ \beta\epsilon k^2 \cos\phi + (V - \beta k)\alpha\epsilon k \sin\phi \end{pmatrix}. \tag{2.85}$$

If we now look at only the y-component of $\mathrm{d}\mathbf{s}/\mathrm{d}t$ above and we compare it with the y-component of the analytic solution obtained in equation 2.78 we arrive at:

$$\epsilon\omega \sin\phi + \frac{\mathrm{d}\epsilon}{\mathrm{d}t} \cos\phi = \beta\epsilon k^2 \sin\phi + (V - \beta k)\alpha\epsilon k \cos\phi. \tag{2.86}$$

Now by comparing the coefficients of $\cos\phi$ we obtain:

$$\frac{\mathrm{d}\epsilon}{\mathrm{d}t} = (V - \beta k)\alpha\epsilon k. \tag{2.87}$$

If we now say $\sigma = \alpha k(V - \beta k)$, then we have:

$$\frac{\mathrm{d}\epsilon}{\mathrm{d}t} = \sigma\epsilon \tag{2.88}$$

$$\Rightarrow \int \frac{\mathrm{d}\epsilon}{\epsilon} = \int \sigma \mathrm{d}t \tag{2.89}$$

$$\Rightarrow \ln|\epsilon| = \sigma t + C \tag{2.90}$$

$$\Rightarrow \epsilon = Ae^{\sigma t}. \tag{2.91}$$

So over time we expect $\epsilon$ to grow exponentially governed by the following equation:

$$\epsilon = Ae^{\alpha(Vk-\beta k^2)t}, \tag{2.92}$$

where $A$ is the initial amplitude of our perturbation, $\alpha$ is a temperature dependent friction coefficient, $V$ is the x-component of the normal fluid velocity, and $k$ is the wavenumber. Finally it is this equation which we will check our simulation results are in good agreement with.

To compare this result with the code, I setup a simulation in a periodic box of size $D = 0.05$cm with a numerical resolution of $\delta = 0.0005$cm and a time-step of $dt = 2\times10^{-6}$s, using the local induction approximation to calculate the self-induced superfluid velocity, with a normal fluid flow (in the x-direction only) of speed $V = 1$m/s. I then fix the value of $\beta$ to be $\beta = 1.3 \times 10^{-2}$, and set $\alpha = 1$ (and also $\alpha' = 0$), the initial condition is a single line orientated in the x-direction (shown on the left of figure 2.14).

I then let this simulation evolve over time, monitoring the radius of the perturbation $\epsilon$ in the yz-plane where $\epsilon = \left\langle \sqrt{s_y^2 + s_z^2} \right\rangle$ and the results for this are shown below in Figure 2.15.

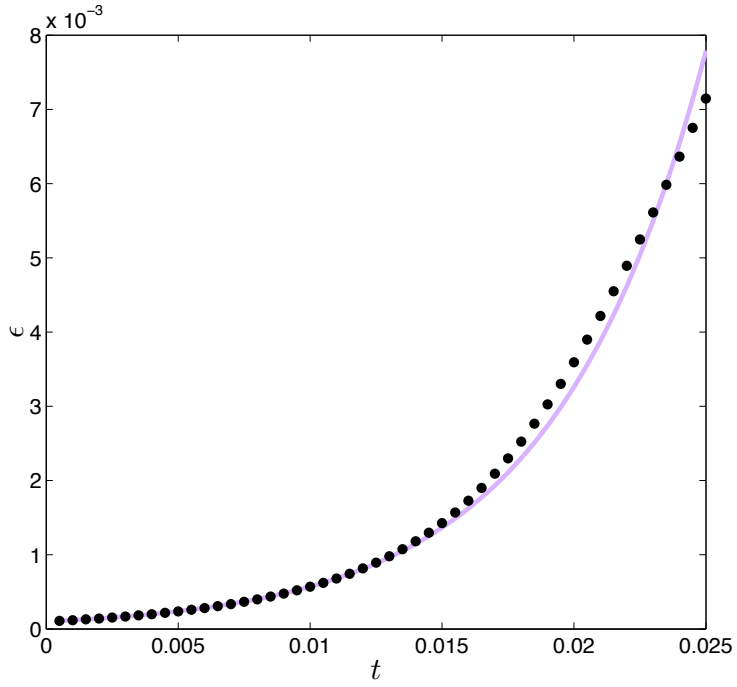


Figure 2.15: Plot of time against the radius of the perturbation, $\epsilon$. The purple line is the expected result from the analytical derivation of the velocity. The black dots are the measured velocities from the time-series run in the code.

Looking at Figure 2.15, the correlation between my results and those of the analytical solution. It is clear that values and trends are closely aligned showing that the code is behaving in accordance with expectation.

# Chapter 3

# Thermally and mechanically driven quantum turbulence in helium II

## 3.1 Background

Recent work [Skrbek & Sreenivasan, 2012; Vinen & Niemela, 2002] has highlighted similarities between the turbulence of superfluid helium II (quantum turbulence) and the turbulence of ordinary (classical) fluids. In particular, experimental [Maurer & Tabeling, 1998; Salort *et al.*, 2010] (as discussed in section 1.5.2) and theoretical [Nore *et al.*, 1997; Araki *et al.*, 2002; Kobayashi & Tsubota, 2005; Sasa *et al.*, 2011; Baggaley & Barenghi, 2011*b*; Baggaley *et al.*, 2012*b*; Lvov *et al.*, 2006] studies have established that the distribution of the superfluid kinetic energy over the length scales (energy spectrum) obeys the same $k^{-5/3}$ Kolmogorov scaling of ordinary turbulence [Frisch, 1995] where $k$ is the wavenumber. The similarity is remarkable because helium II is unlike an ordinary fluid: firstly, it has a two-fluid nature, consisting of a viscous normal fluid component and an inviscid superfluid component coupled by a mutual friction [Donnelly, 1991]; secondly, superfluid vorticity is not a continuous field (as in an ordinary fluid) but is restricted to discrete vortex filaments around which the circulation is fixed to the ratio of Planck's constant and the mass of one helium atom.

As previously addressed in section 1.5, for most experiments, turbulence in helium II is excited mechanically (by stirring the helium with grids [Stalp *et al.*, 1999; Zmeev *et al.*, 2015] or propellers [Smith *et al.*, 1993; Maurer & Tabeling, 1998; Salort *et al.*, 2010] or forcing it along pipes [Walstrom *et al.*, 1988]), or thermally (by the application of a heat flux [Vinen, 1957*b*, 1958, 1957*c*,*a*; Tough, 1982]). The simplest, most studied form of

thermal stirring (to which hereafter we restrict our work) is called thermal counterflow (for more detail see section 1.5.1). Other forms of heat transfer (e.g. pure superflow) and other techniques to generate turbulence (e.g. ultrasound [Schwarz & Smith, 1981], ion injection and spin-downs [Walmsley & Golov, 2008]) are either less studied, or refer to the low temperature limit (below 1 K), or have a special character (rotating turbulence, turbulent fronts, the Kibble-Zurek mechanism, etc.), thus they are not our interest here, and nor are the special methods used to model them. For these aspects we refer the reader to a recent review by Tsubota & Halperin [2009].

The aim of this work is to clarify the difference between thermally-excited counterflow turbulence and mechanically-excited turbulence in helium II. For simplicity, we are concerned only with statistically steady state turbulence away from boundaries (thus ignoring the important problems of turbulence decay and flow profiles), and at the relatively high temperatures, where mutual friction is the dominant dissipative mechanism.

Following the methods laid out in Chapter 2 we set up to investigate thermally-driven turbulence using our counterflow model and mechanically-driven turbulence using our KS flow model. All simulations in this chapter are computed within a periodic box of size $D = 0.1$, and using a tree-method with a critical opening angle of $\theta = 0.4$. We then compute the energy spectrum of counterflow turbulence, compare it to the spectrum of mechanically-driven turbulence, and test the idea which has been proposed in the literature that "counterflow turbulence has only one length scale", meaning the average intervortex distance (section 3.2). We also find that thermally- and mechanically-induced turbulence differ with respect to curvature (section 3.3), the presence of coherent structures (section 3.4) and vortex reconnection statistics. The last result suggests a method to detect experimentally the existence of superfluid vortex bundles (section 3.5). Section 3.6 summarises the conclusions.

It must be stressed that our models have a limitation: the normal fluid is prescribed rather than computed self-consistently. The inclusion of the back-reaction of the superfluid vortices onto the normal fluid would require the numerical solution of the Navier-Stokes equation for the normal fluid (suitably modified by the inclusion of a mutual friction term), alongside the time evolution of the superfluid vortices. However, a dynamically self-consistent model would be very complex and computationally expensive, and one could not easily explore parameter space and the effects of changing numerical resolution and initial conditions. This approach was attempted for a single vortex ring [Kivotides *et al.*, 2000], but in the case of turbulence, this approach has so far been limited to the initial growth of a cloud of vortex lines [Kivotides, 2011] and subsequently to the decay of

turbulence [Kivotides, 2015].

## 3.2 Energy spectrum

We choose temperature $T = 1.9$ K (at which $\alpha = 0.206$ and $\alpha' = 0.0083$) which is typical of experiments and allows direct comparison with previous work, and numerical resolution $\Delta\xi = 0.0016$ cm. First we calculate thermally-induced turbulent vortex tangles at increasing values of $v_{ns}$.

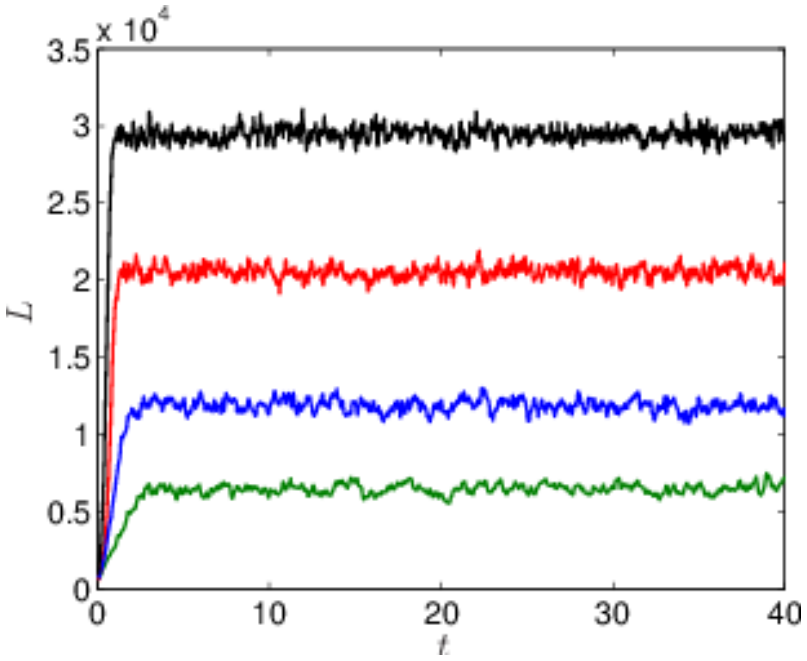


Figure 3.1: Thermally-induced turbulence. The evolution of the vortex line density $L$ (cm$^{-2}$) vs time $t$ (s) at counterflow velocities (from top to bottom) $v_{ns} = 1.25$ cm/s (black), 1.0 cm/s (red), 0.75 cm/s (blue), and 0.55 cm/s (green). Note: this colour scheme is utilised throughout all figures in this chapter.

We find that, after an initial transient, the vortex line density $L$ (vortex length per unit volume) saturates to a statistically steady state (see Fig. 3.1) of density $L = \gamma^2 v_{ns}^2$ which is independent of the details of the initial condition (various vortex loops configurations were tried). Fig. 3.2 (top) shows a snapshot of such vortex tangle.

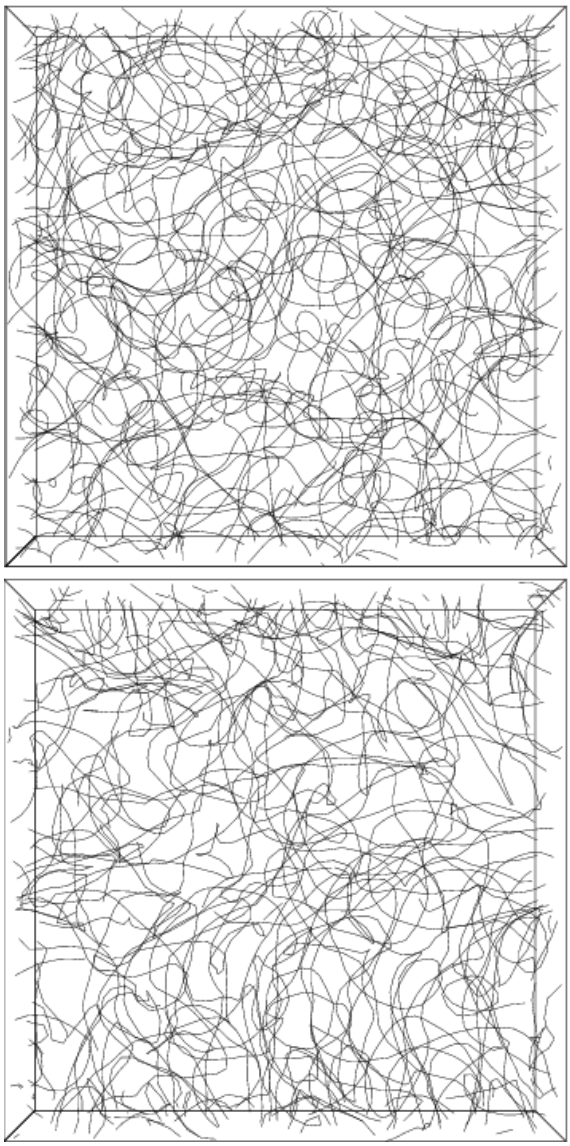

Figure 3.2: Snapshots of vortex tangles ($y, z$ projections). Top: thermally-driven by counterflow ($v_{ns} = 0.75$ cm/s, $L \approx 12000$ cm$^{-2}$); bottom: mechanically-driven ($Re = 208$, $L \approx 12000$ cm$^{-2}$)

Our vortex line densities agree with previous work; for example, taking $T = 1.9$ K we obtain $\gamma \approx 137$ s/cm$^2$ which compares well to $\gamma \approx 140$ and 133 obtained in the numerical simulations of Adachi *et al.* [2010] and in the experiments of Childers and Tough [1976] respectively.

To analyse our results we Fourier-transform the superfluid velocity and compute the energy spectrum $E_k$. If the turbulence is isotropic, $E_k$ is defined by

$$E = \frac{1}{V}\int_V \frac{1}{2}\mathbf{v}_s^2 dV = \int_0^\infty E_k dk, \tag{3.1}$$

where $V$ is volume, $k = |\mathbf{k}|$, and $\mathbf{k}$ is the three-dimensional wavenumber. However, it is well known [Schwarz, 1988; Adachi *et al.*, 2010] that counterflow turbulence is flattened on the $(y, z)$ plane perpendicular to the direction $(x)$ of the heat flux. For example, if $L_x$, $L_y$ and $L_z$ are the vortex lengths (per unit volume) projected in the $x$, $y$ and $z$-direction, at $v_{ns} = 1.25$ cm/s we have $L_x/L = 0.34 < L_y/L = 0.55 = L_z/L$. It is therefore better to distinguish between parallel and perpendicular superfluid energy spectra, $E_\parallel$ and $E_\perp$, calculated replacing $|\mathbf{v}_s^2| = v_{sx}^2 + v_{sy}^2 + v_{sz}^2$ in Eq. (3.1) with $3v_{sx}^2$ and $(3/2)(v_{sy}^2 + v_{sz}^2)$ respectively. Fig. 3.3 (left) shows $E_\perp$ for various $v_{ns}$ plotted in the range $k_D = 2\pi/D \leq k_\perp \leq k_{\Delta\xi} = 2\pi/\Delta\xi$ (where $k_\perp$ is the perpendicular wavevector); the vertical lines mark the wavenumbers $k_\ell = 2\pi/\ell$ corresponding to the average intervortex spacing, $\ell \approx L^{-1/2}$. It is apparent that the perpendicular energy spectrum $E_\perp$ has a broad peak in the mesoscales at intermediate wavenumbers $k_D < k < k_\ell$. At larger $k$ the spectrum follows the typical $k^{-1}$ scaling of smooth isolated vortex lines as expected. The parallel spectrum $E_\parallel$ vs $k_\parallel$ (where $k_\parallel$ is the parallel wavevector) exhibits similar features, see Fig. 3.3 (right). Plotting $E_\perp$ and $E_\parallel$ vs $k$ rather than $k_\perp$ and $k_\parallel$ yields similar results. We note that the counterflow energy spectrum, which we measure, is qualitatively similar to the spectrum shown by Nemirovskii, Tsubota and Araki [Nemirovskii *et al.*, 2002] in their Fig.2.

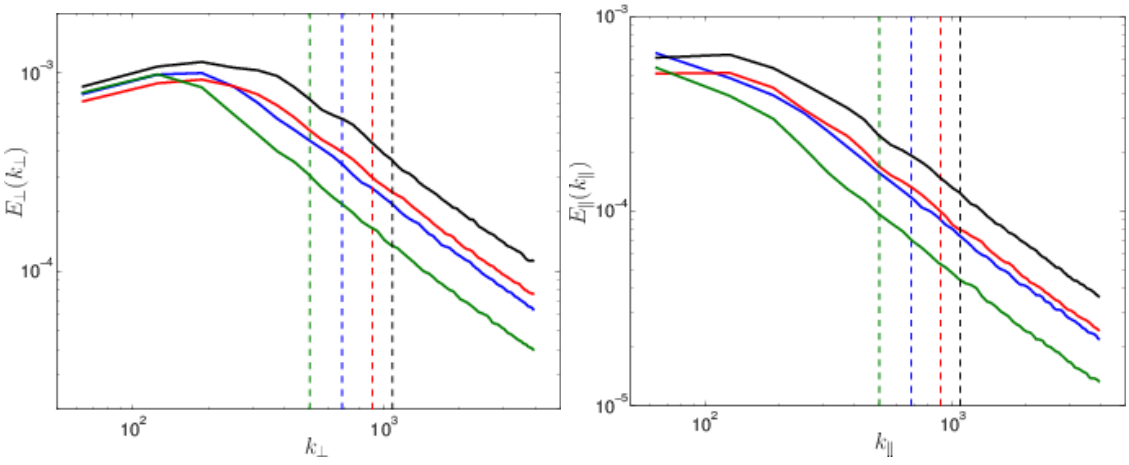


Figure 3.3: Counterflow turbulence. Left: the perpendicular energy spectrum $E_\perp(k_\perp)$ (arbitrary units) vs wavenumber $k_\perp$ (cm$^{-1}$). Right: the parallel energy spectrum $E_\parallel(k_\parallel)$ (arbitrary units) vs wavenumber $k_\parallel$ (cm$^{-1}$). The vertical lines mark $k_\ell$ at increasing $v_{ns}$ from right to left.

Proceeding in analogy to what we did for counterflow turbulence, we start from an arbitrary seeding initial condition, drive the vortex tangle with the synthetic turbulent

flow of Eq. (2.63), and let $L$ grow and saturate to a statistical steady state of turbulence which does not depend on the initial condition (the time behaviour of $L$ is similar to Fig. 3.1). A snapshot of this mechanically-driven tangle is shown in Fig. 3.2 (bottom). We then compute the superfluid energy spectrum. In agreement with previous experimental [Maurer & Tabeling, 1998; Salort *et al.*, 2010] and theoretical [Baggaley & Barenghi, 2011*b*; Lvov *et al.*, 2006] work, we find that the energy is concentrated at the largest scales, $k \approx k_D$, and that $E_k \sim k^{-5/3}$ for small $k$ (see Fig. 3.4).

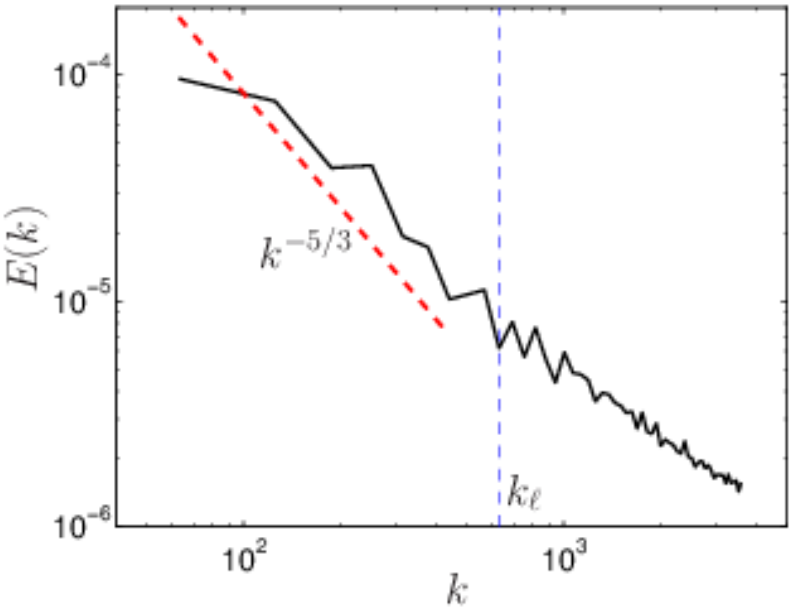


Figure 3.4: Mechanically-induced turbulence. Energy spectrum $E_k$ (arbitrary units) vs wavenumber $k$ ($\mathrm{cm}^{-1}$) of vortex tangle driven by the synthetic turbulent flow of Eq. (2.63) with $M = 188$ modes. The vertical dashed blue line marks $k_\ell$. The dashed red line shows the $k^{-5/3}$ Kolmogorov scaling. The effective Reynolds number of the normal fluid is $Re = (k_M/k_1)^{4/3} = 208$, defined by the condition that the dissipation time equals the eddy turnover time at $k_M$.

We conclude that there is a remarkable spectral difference between thermally-driven turbulence and mechanically-driven turbulence. Whereas in the former the turbulent kinetic energy is concentrated at intermediate length scales, in the latter most of the energy is at the largest scales, as in classical ordinary turbulence.

An argument is often made in the literature that counterflow turbulence has only one characteristic length scale, the intervortex distance $\ell$: it is apparent from Fig. 3.3 that $E_k$ does not have a sharp peak at $k \approx k_\ell = 2\pi/\ell$ (indicated by the vertical lines), but rather a broad maximum at smaller wavenumbers in the mesoscale region $k_D < k \leq k_\ell$. The traditional argument, although quantitatively wrong, is thus qualitatively correct.

## 3.3 Curvature

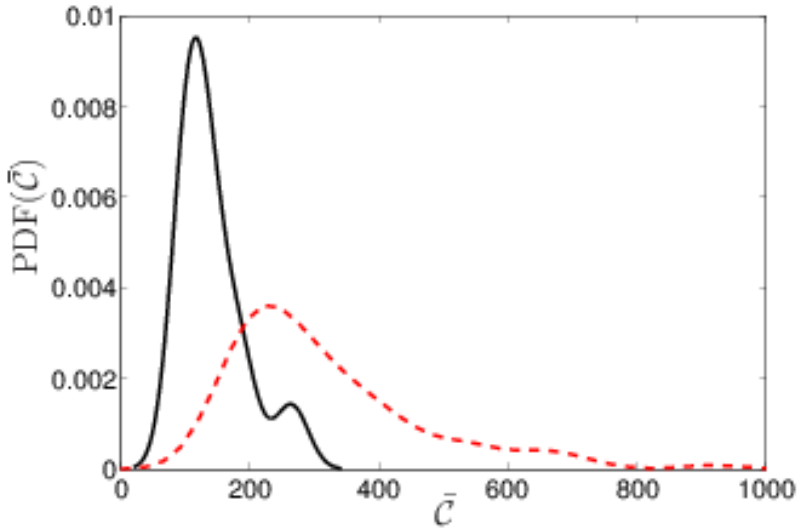


Figure 3.5: Probability density function (PDF) of the mean curvature per vortex loop $\bar{C}$ (cm$^{-1}$) . Solid black line: mechanically-driven turbulence; dashed red line: thermally-driven turbulence. Notice the larger curvatures present in thermally-driven turbulence.

If we look carefully at the vortex tangles shown in Fig. 3.2, we notice that the thermally-driven tangle (top) contains relatively more closed loops, and the mechanically-driven tangle (bottom) contains relatively more long vortices which extend throughout the periodic computational domain. We sample the curvature $C = |\mathbf{s}''|$ along each vortex loop and construct the probability density function (PDF) of the mean curvature $\bar{C}$ of each distinct loop. Fig. 3.5 shows the result. We notice that mechanically-driven turbulence contains smaller curvatures (that is, larger radii of curvature $R = 1/C$) than thermally-driven turbulence; indeed, for the latter PDF($\bar{C}$) has a maximum at $\bar{C} \approx 250$ cm$^{-1}$ in correspondence of the maximum of the energy spectrum shown in Fig. 3.3.

As an additional numerical experiment, we compute the energy spectra of configurations of circular vortex rings placed randomly in the periodic box of size $D$ as a function of the rings' radius $R$. We find that if $R \geq D$ (in which case rings are "folded" into broken arches by the periodic boundary conditions) most of the energy is concentrated at the largest length scales, whereas if $R < D$ the energy spectrum peaks at intermediate scales, in analogy with the counterflow spectrum.

## 3.4 Coherent structures

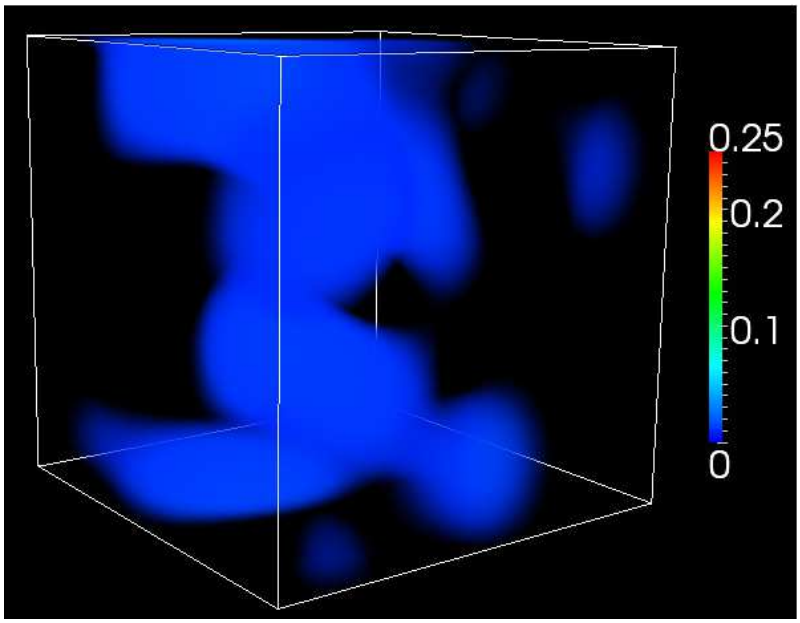


Figure 3.6: Smoothed vorticity $|\boldsymbol{\omega}|$ sustained by a constant $\mathbf{v}_n^{ext}$ (thermally-driven turbulence).

We also notice another difference between the two forms of turbulence. If we convolve the vortex filaments with a Gaussian kernel and define a smoothed vorticity field $\boldsymbol{\omega}_s$ (the details of the procedure are described in Ref. [Baggaley *et al.*, 2012*b*]), it becomes apparent - see Fig. 3.6 - that the thermally-induced tangle (sustained by the uniform $\mathbf{v}_n^{ext}$) is essentially featureless, whereas the mechanically-induced tangle (sustained by the turbulent $\mathbf{v}_n^{ext}$) contains "vortical worms", or regions of concentrated vorticity - see Fig. 3.7. This result is consistent with the observation of "worms" in two other related turbulent flows: ordinary viscous turbulence [Frisch, 1995] and pure superfluid turbulence at $T = 0$ without the normal fluid [Baggaley *et al.*, 2012*b*]; both flows satisfy the Kolmogorov $k^{-5/3}$ scaling.

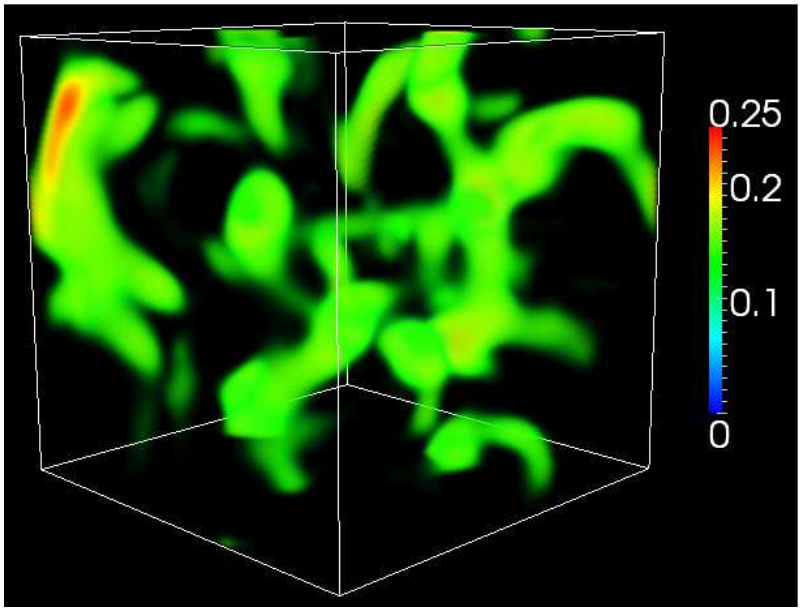


Figure 3.7: Smoothed vorticity $|\boldsymbol{\omega}|$ sustained by a turbulent $\mathbf{v}_n^{ext}$ (mechanically-driven turbulence). Notice the intense vortical regions compared to Fig. 3.6 which is plotted on the same scale.

It is known from previous work that if intense regions of normal fluid vorticity are imposed, such as Gaussian vortex tubes [Samuels, 1993], ABC flows [Barenghi *et al.*, 1997] or worms [Kivotides, 2006; Morris *et al.*, 2008], these structures will induce (via the friction force) similar structures in the superfluid vortex lines. Our synthetic turbulent flow $\mathbf{v}_n^{ext}$, although not completely featureless on its own, contains only weak vortex structures, much smaller [Fung *et al.*, 1992] than the vortical worms arising from direct numerical simulations of the Navier-Stokes equation. Therefore the observation of superfluid vortex bundles driven by the synthetic turbulent flow $\mathbf{v}_n^{ext}$ of Eq. (2.63) must be an underestimate of the strength of these bundles. If we solved the Navier-Stokes equation for the normal fluid (rather than imposing $\mathbf{v}_n^{ext}$), the normal fluid's worms would probably "imprint" vortex bundles in the superfluid, besides the bundles which arise naturally in the superfluid as a consequence of Euler dynamics [Baggaley *et al.*, 2012*b*].

A tentative explanation of the observation that the vortex configuration is rather homogeneous for thermally-driven turbulence and inhomogeneous for mechanically-driven turbulence is that in the former (assuming, as we do, a uniform normal flow) the growth rate of the Donnelly-Glaberson (DG) instability (which transforms normal fluid's energy into superfluid vortex length) is the same everywhere, whereas in the latter it changes with time and space.

The DG mechanism is the following [Tsubota *et al.*, 2004]. If it is large enough, the

component $V$ of the normal fluid velocity along a vortex line can destabilise a (helical) Kelvin wave of given wavenumber $k$. In this case, the Kelvin wave grows with amplitude $\mathcal{A}(t) = \mathcal{A}(0)e^{\sigma t}$, where $A(0)$ is the initial amplitude of the helix and

$$\sigma(k) = \alpha(kV - \nu' k^2), \tag{3.2}$$

is the growth rate, $\nu' = \kappa\mathcal{L}_1/(4\pi) \approx \kappa$, and $\mathcal{L}_1 = \ln[1/(ka_0)]$. The growth of the Kelvin wave, however, may be interrupted by a vortex reconnection which "breaks" the vortex line. It is known that vortex reconnections play an essential role in the turbulence [Feynman, 1955*a*; Schwarz, 1988; Nemirovskii, 2008]. Therefore, it is prudent to assess the effect of reconnections on the DG instability.

Consider mechanically-driven turbulence in a statistically steady state at $T = 1.9$ K ($\alpha = 0.206$) driven by the rms normal fluid velocity $V \approx 0.93$ cm/s, with average vortex length $\Lambda \approx 11.5$ cm, vortex line density $L \approx 1.15 \times 10^4$ cm$^{-2}$, and intervortex spacing $\ell \approx 9.3 \times 10^{-3}$ cm, and thermally-driven turbulence at the same temperature with $V = 0.75$ cm/s, $\Lambda \approx 11.88$ cm, $L \approx 1.19 \times 10^4$ cm$^{-2}$, and $\ell \approx 9.2 \times 10^{-3}$. The average number $\zeta$ of vortex reconnections per unit time is monitored during the numerical calculations; we obtain $\zeta \approx 4370$ and 7386 s$^{-1}$ for mechanically and thermally driven turbulence, respectively (in reasonable agreement with the estimate $\zeta \approx (2/3)\kappa L^{5/2} \approx 9500$ s$^{-1}$, for a homogeneous isotropic tangle, of Barenghi & Samuels [Barenghi & Samuels, 2004]).

The mode which undergoes the most rapid DG instability has wavenumber $k_{\max} = V/(2\nu')$ and growth rate $\sigma_{\max} = \alpha V^2/(4\nu')$, corresponding to the length scale $d_{\max} = 2\pi/k_{\max}$. In both mechanically-driven and thermally-driven cases this length scale ($d_{\max} = 0.015$ and 0.017 cm respectively) is larger than the average distance between vortices $\ell$, and so not suitable for our analysis. We therefore perform an analysis for Kelvin waves with a wavelength and a wavenumber equal to $\ell$ and $k_\ell = 2\pi/\ell$, respectively; we assume that such waves are the lowest frequency waves in our system. The growth rate of such a waves is $\sigma_{DG} = \sigma(k_\ell)$, where $\sigma(k)$ is defined in Eq. (3.2).

The reconnection rate $\zeta$ computed during the simulations is a statistical property of the vortex tangle as a whole. However we can compute a reconnection frequency for a wavenumber and wave amplitude by scaling the total reconnection rate by the fraction of the total vortex length that a given wavelength takes. In such a manner we define

$$\sigma_r(\mathcal{A}) = \frac{\zeta}{\Lambda}\int_0^\ell \left[1 + (\mathcal{A}k_\ell)^2\cos^2(k_\ell x)\right]^{-1/2} dx. \tag{3.3}$$

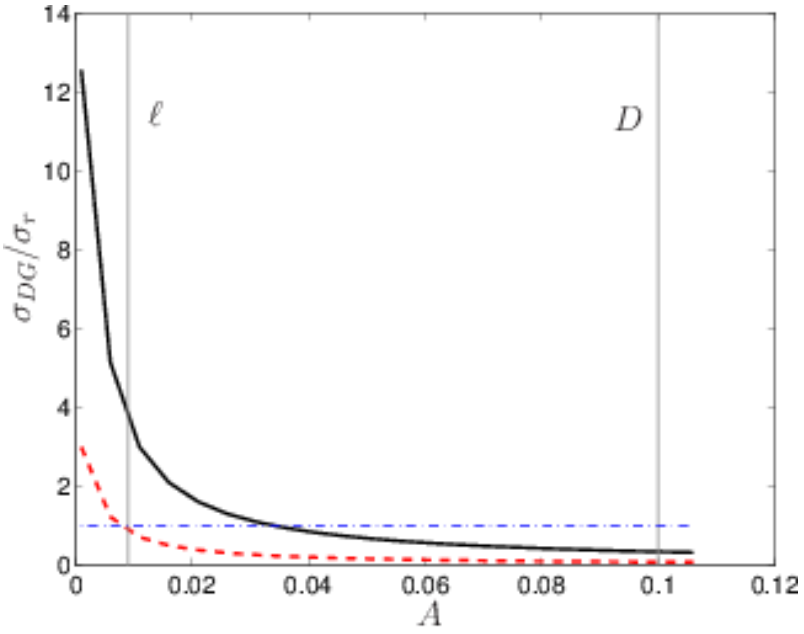


Figure 3.8: Plot of $\sigma_{DG}/\sigma_r$ (ratio of Donnelly-Glaberson and vortex reconnection frequencies) vs wave amplitude $A$ (cm), for thermally (dashed, red line) and mechanically (solid line) driven turbulence; the (blue) dot-dashed line represents $\sigma_{DG} = \sigma_r$.

Fig. 3.8 shows the ratio $\sigma_{DG}/\sigma_r$ vs wave amplitude $\mathcal{A}$ for the two simulations described above. We note a large contrast in the behaviour of the ratio of these two timescales when comparing the mechanically and thermally driven cases. For the latter one would estimate that the amplitude of perturbations along the vortices can grow to approximately the intervortex spacing before reconnections dominate the behaviour of the tangle. However, in the mechanically driven case $\sigma_{DG} \approx \sigma_r$ for $\mathcal{A} \approx D/3$ so that the large amplitude perturbations are able to grow, before reconnections randomise the tangle and introduce topological changes. Therefore the difference in the balance between these two competing timescales is likely to be partially responsible for the differences in the nature of the two turbulent systems.

## 3.5 Vortex reconnections

The existence of superfluid vortex bundles [Samuels, 1993; Barenghi *et al.*, 1997; Kivotides, 2006; Morris *et al.*, 2008], their dynamics [Alamri *et al.*, 2008] and their particular significance at very low temperatures [L'vov *et al.*, 2007; Kozik & Svistunov, 2008*a*] have been discussed in the literature, but so far there is no clear experimental evidence for them. It has been argued that the presence of bundles of locally almost parallel vortices (which we have demonstrated in the previous section for mechanically-induced turbulence) leads to a suppression of vortex reconnections [L'vov *et al.*, 2007; Kozik & Svistunov, 2008*a*].

In the vortex filament model, vortex reconnections are performed algorithmically; the details are described in Ref. [Baggaley, 2012]. Within the approximation, intrinsic to the model, it is instructive to study the distribution of the angles $\theta$ between reconnecting vortex lines at the level of discretisation which we use (which is necessarily much larger than $a_0$). The normalised distribution of values of $\theta$, PDF($\theta$), is shown in Fig. 3.9: the solid black line with black circles refers to mechanically-driven turbulence, and the solid red line with red squares to thermally driven turbulence. It is apparent that in thermally-induced turbulence the majority of vortex reconnections take place between vortex filaments which are nearly anti-parallel ($\theta \approx \pi$), whereas in mechanically-driven turbulence most reconnections are between vortices which are nearly parallel ($\theta < \pi/2$). Our results confirm that indeed the presence of organised bundles of vortices changes the typical geometry of reconnections.

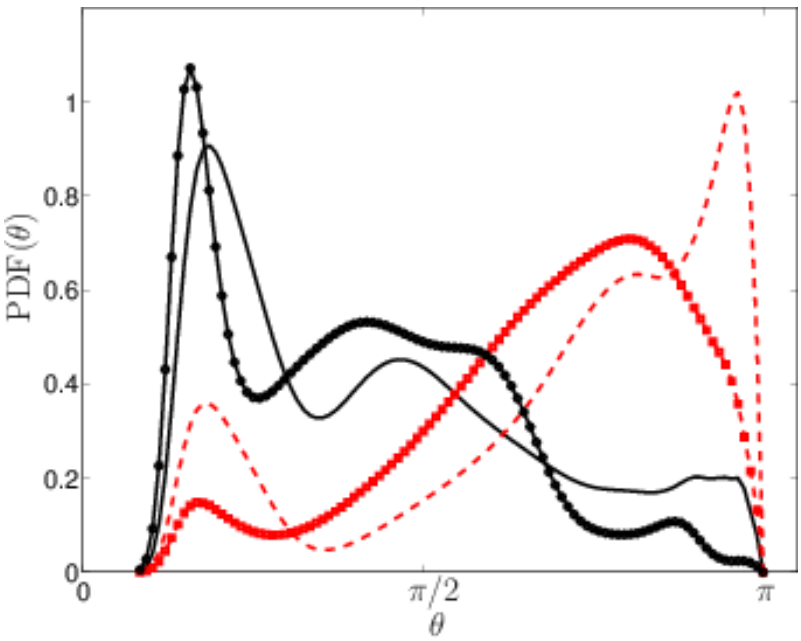


Figure 3.9: The probability density function (PDF) of the angle between reconnecting vortices, $\theta$. Thermally-driven turbulence: at $T = 2.1\ K$ (dashed red line) and at $T = 1.9\ K$ (solid red squares); mechanically-driven turbulence: at $T = 2.1\ K$ (solid black line) and at $T = 1.9\ K$ (solid black line with solid black circles). Note that for thermally-driven turbulence the distribution peaks at large $\theta$, whereas for mechanically-driven turbulence it peaks at small $\theta$.

To check the temperature dependence of the results we repeat our calculations at higher temperature, $T = 2.1\ K$. At this temperature the friction coefficients are larger ($\alpha = 1.21$ and $\alpha' = -0.3883$), therefore a more intense vortex tangle is generated at the same value of the drive; moreover, short Kelvin waves are damped out more quickly. We

check that at the higher temperature $T = 2.1\ K$ the same differences between thermally-driven and mechanically-driven turbulence are present, which we have described in the previous sections for $T = 1.9$ K in terms of energy spectrum, curvature and coherent structures. Fig. 3.9 shows that, qualitatively, the distribution of reconnecting angles is also temperature independent (the black solid line, which refers to mechanically-driven turbulence peaks at small $\theta$, the solid red line which refers to thermally-driven turbulence peaks at large $\theta$).

This result could be exploited to look for experimental evidence of superfluid vortex bundles in the following way. Using solid hydrogen tracer particles to visualise the vortex lines, Paoletti, Fisher and Lathrop *et al.* [Paoletti *et al.*, 2010] determined that the minimum distance $\delta(t)$ between vortex lines before and after a reconnection scales as

$$\delta(t) = A(\kappa|t - t_0|)^{1/2}(1 + c|t - t_0|), \tag{3.4}$$

where $t_0$ is the time at which the reconnection takes place, with fitting coefficients $A \approx 1.2$ and $c \approx 0$. We proceed in this way, monitoring vortex reconnections in our numerical calculations. Fig. 3.10 shows the probability density functions of our fitting parameters $A$ and $c$ obtained for 1107 reconnections in thermally-driven turbulence (average values $\langle A \rangle = 2.6$ and $\langle c \rangle = 1.6$) and 879 reconnections in mechanically-driven turbulence (average values $\langle A \rangle = 1.8$ and $\langle c \rangle = 0.7\,\mathrm{s}^{-1}$). Our fitting coefficients thus agree fairly well with the experimental findings of Ref. [Paoletti *et al.*, 2010] and with the numerical results of Tsubota and Adachi [Tsubota & Adachi, 2011] ($A \approx 3$ and $c \approx 0\,\mathrm{s}^{-1}$).

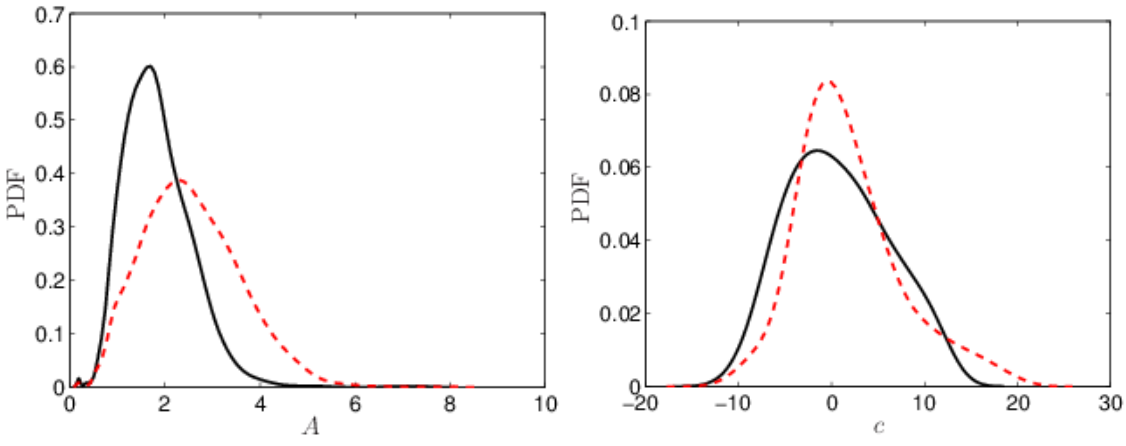


Figure 3.10: Probability density functions (PDF) of the fitting parameters $A$ (left) and $c$ ($\mathrm{s}^{-1}$) (right) of Eq. 3.4. Solid black line: mechanically-driven turbulence; dashed red line: thermally-driven turbulence.

Fig. 3.10 shows that the distribution of values of $A$ is different for thermally-driven

and mechanically-driven turbulence. The effect must arise from the different distributions of curvature and reconnecting angles $\theta$ for vortex bundles, which are present only in mechanically-driven turbulence. This is confirmed by Fig. 3.11, which displays scatter plots of the fitting parameters $A$ (top) and $c$ (middle). Fig. 3.11 also shows the angular dependence of the mean curvature $\bar{\mathcal{C}}_r$ (bottom) of the reconnecting vortex segments.

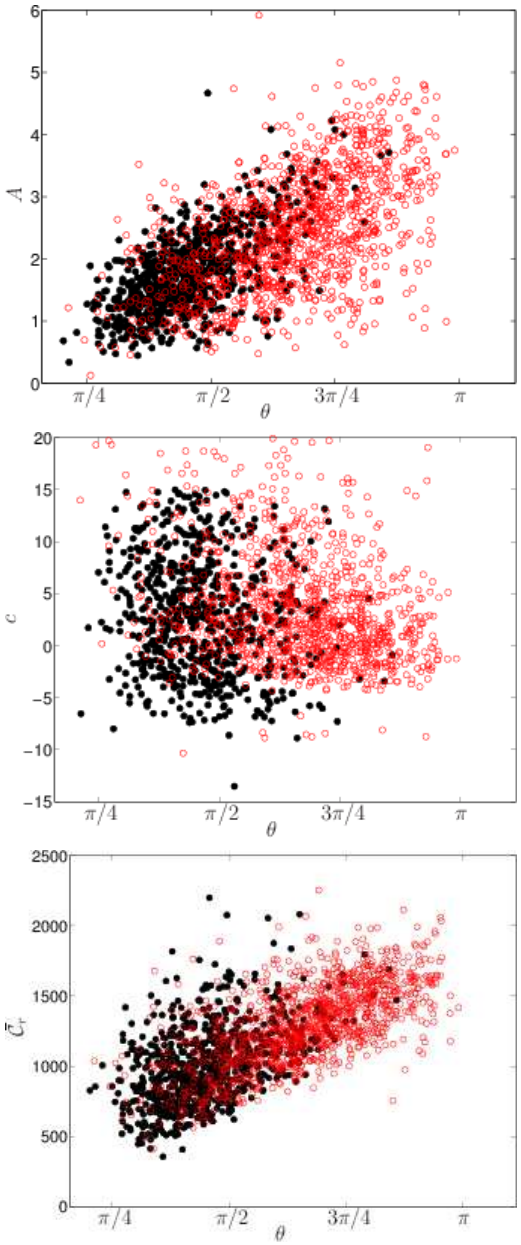


Figure 3.11: Scatter plots of the fitting parameters $A$ (top) and $c$ (middle) of Eq. 3.4 vs the angle, $\theta$, between the reconnecting vortices. The bottom figure shows the mean curvature $\bar{\mathcal{C}}_r$ of the reconnecting vortex segments vs the angle $\theta$. Solid black points: mechanically-driven turbulence; open red circles: thermally-driven turbulence.

It is clear that the curvature of the filaments after a reconnection is dependent on the angle of the reconnection. From inspection of the local induction approximation [Saffman, 1993] we would expect larger velocities (and thus $A$) with increased curvature, as we observe in the numerical simulations. These results suggest a possible experimental strategy to establish the existence of vortex bundles based on the careful analysis of the reconnection fitting parameter $A$.

## 3.6 Conclusions

In conclusion, we have addressed the question of the energy spectrum of thermally-induced counterflow turbulence, and found that it is unlike the spectrum of turbulence generated mechanically. More generally, we have found that the two forms of quantum turbulence which can be generated in superfluid helium are quite different. Counterflow turbulence, driven thermally by a constant normal fluid velocity, is uniform in physical space and the energy spectrum is concentrated at intermediate wavenumbers $k$. On the contrary, quantum turbulence driven mechanically by a turbulent normal fluid contains regions of concentrated coherent vorticity and vortex lines with larger radii of curvature; the energy is concentrated at the largest scales, exhibiting the same $k^{-5/3}$ scaling of ordinary turbulence which suggests the presence of an energy cascade. Our results prove that counterflow turbulence, a form of disordered heat transfer unique to liquid helium, lacks the multitude of interacting length scales which is perhaps the main property of ordinary turbulence. Vortex reconnections are affected by the presence of bundles of almost parallel vortices, suggesting an experimental technique to detect these bundles based on monitoring the vortex separation after reconnections.

# Chapter 4

# Local and nonlocal dynamics in superfluid turbulence

## 4.1 Aim and Methodology

Under certain conditions, it has been argued [Vinen & Niemela, 2002; Skrbek & Sreenivasan, 2012] that the turbulent tangle is characterised by a single length scale, the average distance $\ell$ between the vortex lines, which is inferred from the experimentally observed vortex line density $L$ (length of vortex line per unit volume) as $\ell \approx L^{-1/2}$. Models based on this property describe fairly well the pioneering experiments of Vinen 1957*a*, in which an applied heat flux drives the superfluid and the normal fluid in opposite directions (thermal counterflow). More recently, such 'Vinen' tangles were created at very low temperatures by short injections of ions [Walmsley & Golov, 2008], exhibiting the characteristic decay $L \sim t^{-1}$ predicted by Vinen [Baggaley *et al.*, 2012*a*].

Under different conditions, however, the experimental evidence is consistent with a more structured vortex tangle [Vinen & Niemela, 2002; Volovik, 2004], where the kinetic energy is distributed over a range of length scales according to the same Kolmogorov law which governs ordinary turbulence. 'Kolmogorov' tangles have been generated at high temperatures by stirring liquid helium with grids [Smith *et al.*, 1993] or propellers [Maurer & Tabeling, 1998; Salort *et al.*, 2010], and at very low temperatures also stirring with grids [Zmeev *et al.*, 2015] or by an intense injection of ions [Walmsley & Golov, 2008], exhibiting the decay $L \sim t^{-3/2}$ expected from the energy spectrum [Smith *et al.*, 1993; Baggaley *et al.*, 2012*a*].

The experimental evidence for these two forms of superfluid turbulence is only indirect and arises from macroscopic observables averaged over the experimental cell, such

as pressure [Maurer & Tabeling, 1998; Salort *et al.*, 2010] (for more detail see section 1.5.2) and vortex line density [Smith *et al.*, 1993], not from direct visualisation of vortex lines. In a recent paper [Baggaley *et al.*, 2012*d*], included as Chapter 3 of this thesis, we have characterised the energy spectrum of the two forms of turbulence, and shown that 'Kolmogorov' turbulence contains metastable, coherent vortex structures [Baggaley *et al.*, 2012*b*,*c*], similar perhaps to the 'worms' which are observed in ordinary turbulence [Frisch, 1995]. The aim of this chapter is to go a step further, and look for the dynamical origin of the reported spectral difference and coherent structures.

As discussed in section 2.2.1 it is well known [Saffman, 1993] that in an incompressible fluid the velocity field $\mathbf{v}$ is determined by the instantaneous distribution of vorticity $\boldsymbol{\omega}$ via the Biot-Savart law:

$$\mathbf{v}(\mathbf{x}) = \frac{1}{4\pi}\int \frac{\boldsymbol{\omega}(\mathbf{x}')\times(\mathbf{x}-\mathbf{x}')}{|\mathbf{x}-\mathbf{x}'|^3} d^3\mathbf{x}' \tag{4.1}$$

where the integral extends over the entire flow. The question which we address is whether the velocity at the point $\mathbf{x}$ is mainly determined by the (local) vorticity near $\mathbf{x}$ or by (non-local) contributions from further away. Since the quantisation of the circulation implies that the velocity field around a vortex line is strictly $1/r$, where $r$ is the radial distance from the line (see section 1.3 for more detail), from the predominance of local effects we would infer that the vorticity is randomly distributed and nonlocal effects cancel each other out; conversely, the predominance of nonlocal effects would suggest the existence of coherent structures.

If the vorticity were a continuous field, the distinction between local and nonlocal would involve an arbitrary distance, however in our problem the concentrated nature of vorticity introduces a natural distinction between local and nonlocal contributions, as we shall see.

Again following the numerical approach outlined in Chapter 2, we set up a series of simulations incorporating three types of normal fluid flow. All calculations are performed in a cubic periodic domain of size $D = 0.1$ cm using an Adams-Bashforth time-stepping method (with typical time step $\Delta t = 5 \times 10^{-5}$ s), a tree-method [Baggaley & Barenghi, 2012] with opening angle $\theta = 0.4$, and typical minimal resolution $\delta = 1.6 \times 10^{-3}$ cm. For example, an increase in the numerical resolution from $\delta = 0.0016$ cm to $\delta = 0.0008$ cm produces a small increase of 2.5% in the importance of the nonlocal contribution in Fig. (4.8). Moreover, the tests against experiments mentioned above [Baggaley & Barenghi, 2011*b*; Hanninen & Baggaley, 2014; Adachi *et al.*, 2010], guarantee that the numerical resolution is sufficient, and put the distinction between $\mathbf{v}_s^{loc}$ and $\mathbf{v}_s^{non}$ on solid ground.

We choose a temperature typical of experiments, $T = 1.9$ K (corresponding to $\alpha = 0.206$ and $\alpha' = 0.00834$). In all three cases, the initial condition consists of a few seeding vortex loops, which interact and reconnect, quickly generating a turbulent vortex tangle which appears independent of the initial condition.

We study the following three different regimes of superfluid turbulence, characterised by the following forms of the normal fluid's velocity field $\mathbf{v}_n^{ext}$:

1. **Uniform normal flow (fully detailed in section 2.7.1).** Firstly, to model turbulence generated by a small heat flux at the blocked end of a channel (thermal counterflow), we impose a uniform normal fluid velocity $\mathbf{v}_n^{ext} = V_n\hat{\mathbf{x}}$ in the x-direction (which we interpret as the direction of the channel) which is proportional to the applied heat flux; to conserve mass, we add a uniform superflow $\mathbf{v}_s^{ext} = -(\rho_n/\rho_s)V_n\hat{\mathbf{x}}$ in the opposite direction, where $\rho_n$ and $\rho_s$ are respectively the normal fluid and superfluid densities. Eqs. (2.1) and (2.25) are solved in the imposed superflow's reference frame.

2. **Synthetic turbulence (fully detailed in section 2.7.2).** To model turbulence generated by pushing helium through pipes or channels [Salort *et al.*, 2010] using plungers or bellows or by stirring it with grids [Smith *et al.*, 1993] or propellers [Maurer & Tabeling, 1998], we start from the observation that, due to liquid helium's small viscosity $\mu$, the normal fluid's Reynolds number $\mathrm{Re} = VD/\nu_n$ is usually large (where $V$ is the rms velocity and $\nu_n = \mu/\rho_n$ the kinematic viscosity), hence we expect the normal fluid to be turbulent. We assume $\mathbf{v}_s^{ext} = \mathbf{0}$ and [Osborne *et al.*, 2006]

$$\mathbf{v}_n^{ext}(\mathbf{s},t) = \sum_{m=1}^{M}(\mathbf{A}_m \times \mathbf{k}_m \cos\phi_m + \mathbf{B}_m \times \mathbf{k}_m \sin\phi_m), \tag{4.2}$$

where $\phi_m = \mathbf{k}_m \cdot \mathbf{s} + f_m t$, $\mathbf{k}_m$ are wavevectors and $f_m = \sqrt{k_m^3 E(k_m)}$ are angular frequencies. The random parameters $\mathbf{A}_m$, $\mathbf{B}_m$ and $\mathbf{k}_m$ are chosen so that the normal fluid's energy spectrum obeys Kolmogorov's scaling $E(k_m) \propto k_m^{-5/3}$ in the inertial range $k_1 < k < k_M$, where $k_1 \approx 2\pi/D$ and $k_M$ correspond to the outer scale of the turbulence and the dissipation length scale respectively. Then we define the Reynolds number via $\mathrm{Re} = (k_M/k_1)^{4/3}$. The synthetic turbulent flow defined by Eq. (4.2) is solenoidal, time-dependent, and compares well with Lagrangian statistics obtained in experiments and direct numerical simulations of the Navier-Stokes equation. It is therefore physically realistic and numerically convenient to model current experiments on grid or propeller generated superfluid turbulence.

3. **Frozen Navier-Stokes turbulence.** Synthetic turbulence, being essentially the superposition of random waves, lacks the intense regions of concentrated vorticity which are typical of classical turbulence [Frisch, 1995]. For this reason we consider a third model: a turbulent flow $\mathbf{v}_n^{ext}$ obtained by direct numerical simulation (DNS) of the classical Navier-Stokes equation in a periodic box with no mean flow. Since the simultaneous calculation of superfluid vortices and turbulent normal fluid would be prohibitively expensive, we limit ourselves to a time snapshot of $\mathbf{v}_n^{ext}$. In other words, we determine the vortex lines under a 'frozen' turbulent normal fluid. Our source for the DNS data is the John Hopkins Turbulence Database [Li *et al.*, 2008*a*,*b*], which consists of a velocity field on a $1024^3$ spatial mesh. The estimated Reynolds number is $\mathrm{Re} \approx (L_0/\eta_0)^{4/3} = 3205$ where $L_0$ is the integral scale and $\eta_0$ the Kolmogorov scale. Although $\mathrm{Re} = 3205$ is not a very large Reynolds number, at $T = 1.9\ K$ helium's viscosity is $\mu = 1.347 \times 10^{-5}$ g/(cm s), the normal fluid density is $\rho_n = 0.0611$ g/cm$^3$, the kinematic viscosity is $\nu_n = \mu/\rho_n = 0.22 \times 10^{-3}$ cm/s [Donnelly & Barenghi, 1998], and therefore $\mathrm{Re} = UD/\nu_n = 3205$ corresponds to the reasonable speed $U = 0.7$ cm/s in a typical $D = 1$ cm channel. To keep the resulting vortex line density of this model to a computationally practical value, we rescale the velocity components such that they are 60 percent of their original values, thus obtaining the vortex line density $L \approx 20,0000\ \mathrm{cm}^{-2}$. To obtain Fig. 4.11 the scaling factor is only 45 percent, yielding $L \approx 6,000\ \mathrm{cm}^{-2}$; because of the nonlinearity of the Navier-Stokes equation, this procedure is clearly an approximation but is sufficient for our aim of driving a less intense or more intense vortex tangle.

Fig. 4.1 shows the magnitude of the normal velocity field plotted (at a fixed time $t$) on the $xy$ plane at $z = 0$, corresponding to models 2 and 3 (we do not plot the normal fluid velocity for model 1 because it is uniform). It is apparent that models 1, 2 and 3 represent a progression of increasing complexity of the driving normal flow. In Fig. 4.1, note in particular the localised regions of strong velocity which appear in model 3.

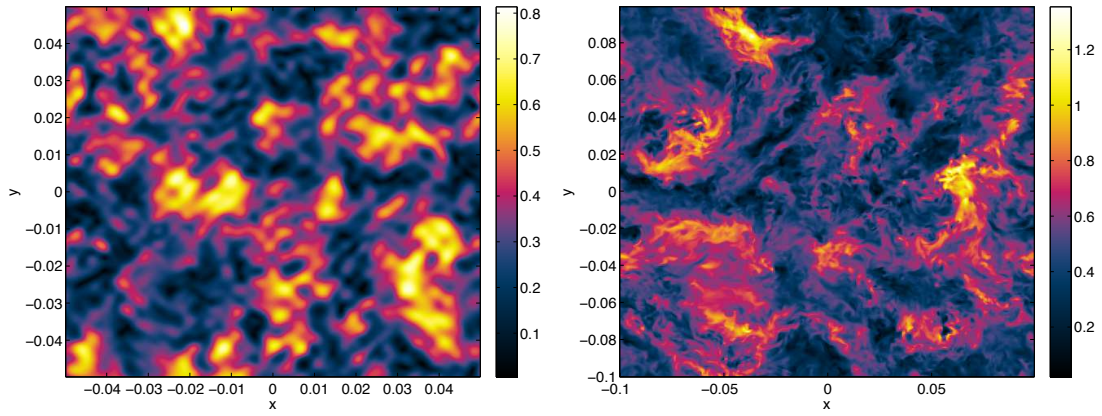


Figure 4.1: (color online). Magnitude of the driving normal fluid velocity field, $|\mathbf{v}_n^{ext}|$, plotted on the $xy$-plane at $z = 0$ corresponding to model 2 (synthetic normal flow turbulence, left) and model 3 (frozen Navier-Stokes turbulence, right). The velocity scales (cm/s) are shown at right of each panel. Note the more localised, more intense regions of velocity which are present in model 3.

## 4.2 Results

The intensity of the turbulence is measured by the vortex line density $L = \Lambda/V$ (where $\Lambda$ is the superfluid vortex length in the volume $V = D^3$), which we monitor for a sufficiently long time, such that the properties which we report, refer to a statistically steady state of turbulence fluctuating about a certain average $L$ (we choose parameters so that $L$ is typical of experiments).

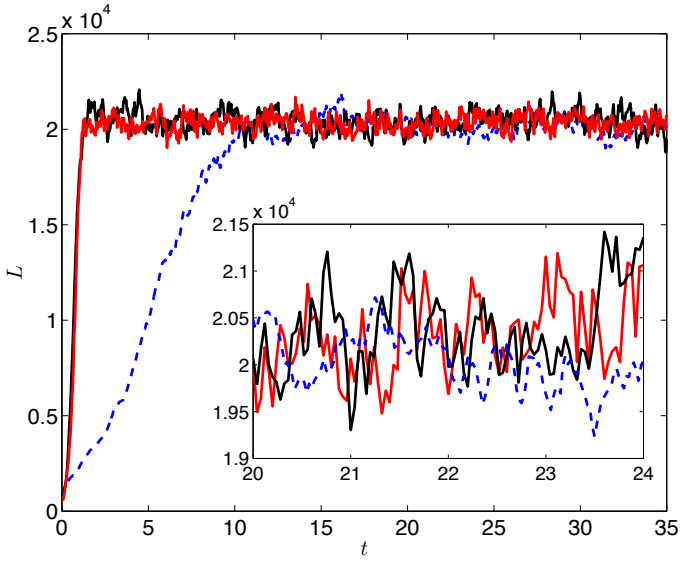


Figure 4.2: (color online). Evolution of the vortex line density $L$ (cm$^{-2}$) vs time $t$ (s) for model 1 (red line, uniform normal flow), model 2 (black line, synthetic normal fluid turbulence) and model 3 (dashed blue line, frozen Navier-Stokes turbulence). The inset displays the oscillations of $L$ vs $t$ in more detail. Parameters: temperature $T = 1.9$ K, $V_n = 1$ cm/s (for model 1), Re $= 79.44$ (for model 2), and Re $= 3025$ (for model 3).

Fig. 4.2 shows the initial transient of the vortex line density followed by the saturation to statistically steady-states of turbulence corresponding to model 1 (uniform normal flow), model 2 (synthetic normal flow turbulence) and model 3 (frozen Navier-Stokes turbulence). In all cases, the intensity of the drive is chosen to generate approximately the same vortex line density, $L \approx 20,000$ cm$^{-2}$.

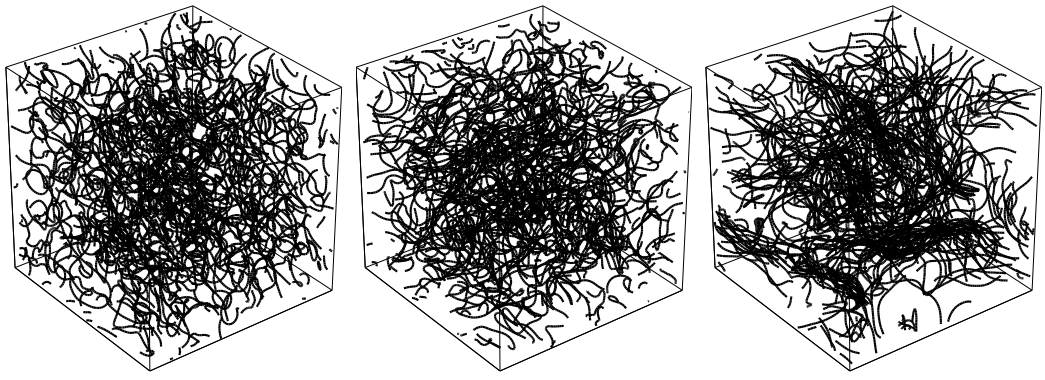

Figure 4.3: Snapshot of the vortex tangle for model 1 (uniform normal fluid, left), model 2 (synthetic turbulence, middle) and model 3 (frozen Navier-Stokes turbulence, right) at time $t = 20$ s (parameters as in Fig. (4.2).

Snapshots of the vortex tangles are shown in Fig. 4.3. The vortex tangle driven by

the uniform normal fluid (model 1, left) appears visually as the most homogeneous; the vortex tangle driven by the frozen Navier-Stokes turbulence (model 3, right) appears as the least homogeneous. What is not apparent in the figure is the mild anisotropy of the tangle driven by the uniform normal fluid. To quantify this anisotropy, we calculate the projected vortex lengths in the three Cartesian directions ($\Lambda_x$, $\Lambda_y$, $\Lambda_z$) and find $\Lambda_x/\Lambda = 0.34 < \Lambda_y/\Lambda = \Lambda_z/\Lambda = 0.54$ for model 1, confirming a small flattening of the vortices in the yz plane (this effect was discovered by the early investigations of Schwarz 1988). In comparison, models 2 and 3 are more isotropic: for model 2 (tangle driven by synthetic turbulence) we find $\Lambda_x/\Lambda = 0.50$, $\Lambda_y/\Lambda = 0.47$ and $\Lambda_z/\Lambda = 0.49$), and for model 3 (tangle driven by frozen Navier-Stokes turbulence) we obtain $\Lambda_x/\Lambda = 0.48$, $\Lambda_y/\Lambda = 0.50$, $\Lambda_z/\Lambda = 0.49$.

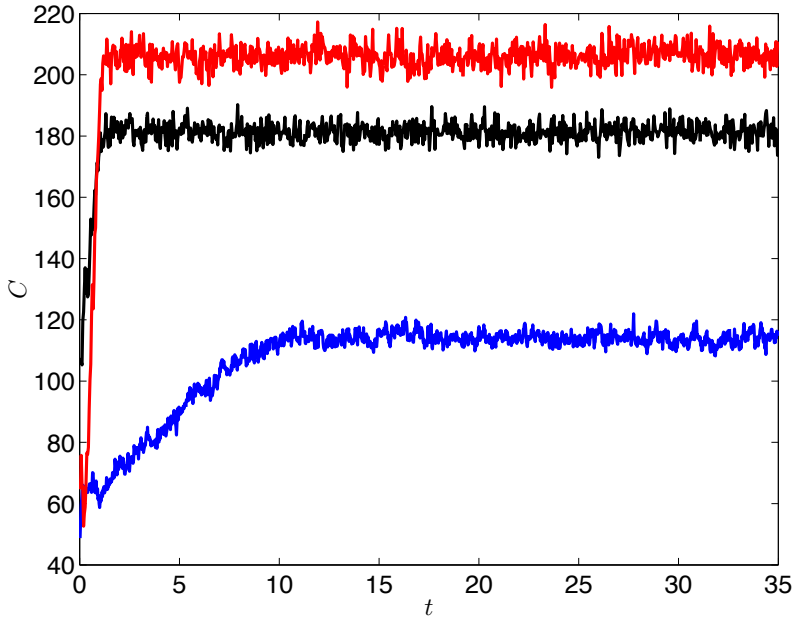


Figure 4.4: (color online). Average curvature $C$ (cm$^{-1}$) vs time $t$ (s) for model 1 (uniform normal flow, red line), model 2 (synthetic turbulence, black line) and model 3 (frozen Navier-Stokes turbulence, dashed blue line). Parameters as in Fig. (4.2).

Fig. 4.4 and 4.5 shows the average curvature $C =< C_j >$ (sampled over the discretisation points $j = 1, \cdots N$) and the distributions of local curvatures $C_j = |\mathbf{s}_j''|$. The tangle generated by model 3 (frozen Navier-Stokes turbulence) has the smallest average curvature: the presence of long lines (large radius of curvature $R = 1/|\mathbf{s}''|$) is indeed visible in Fig. 4.2. In terms of curvature, the tangles generated by models 1 and 2 are more similar to each other - the average curvature is almost twice as large as for model 3, indicating that the vortex lines are more in the form of small loops.

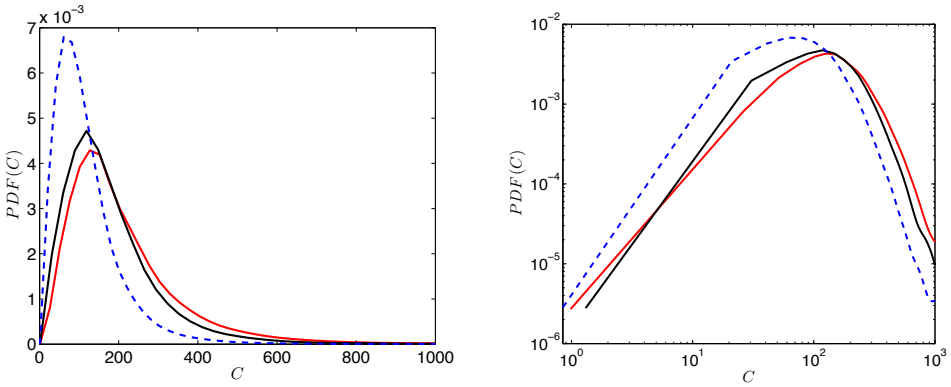


Figure 4.5: (color online). Left: Probability density function of the curvature, PDF($C$), vs curvature, $C$ (cm$^{-1}$), corresponding to model 1 (uniform normal flow, red line), model 2 (synthetic turbulence, black line) and model 3 (frozen Navier-Stokes turbulence, dashed blue line). Right: the same data plotted on a log log scale, where the matching slopes on the plot illustrate that we have the same Kelvin waves in all three models (because they are all at the same temperature). Parameters as in Fig. 4.2.

However, vortex line density (Fig. 4.2), visual inspection (Fig. 4.3) and curvature (Fig. 4.4 and 4.5) do not carry information about the *orientation* of the vortex lines, a crucial ingredient of the dynamics. Fig. 4.6 shows the energy spectrum $E_s(k)$, defined by

$$\frac{1}{V}\int_V \frac{1}{2}\mathbf{v}_s^2 dV = \int_0^\infty E_s(k)dk, \tag{4.3}$$

where $k$ is the magnitude of the three-dimensional wavevector. The energy spectrum describes the distribution of kinetic energy over the length scales. The spectra of the tangles generated by synthetic normal flow turbulence (model 2) and by the frozen Navier-Stokes turbulence (model 3) are consistent with the classical Kolmogorov scaling $E_s(k) \sim k^{-5/3}$ for $k < k_\ell = 2\pi/\ell$; the kinetic energy is clearly concentrated at the largest length scales (small $k$). In contrast, the spectrum of the tangle generated by the uniform normal fluid (model 1) peaks at the intermediate length scales, and at large wavenumbers is consistent with the shallower $k^{-1}$ dependence of individual vortex lines.

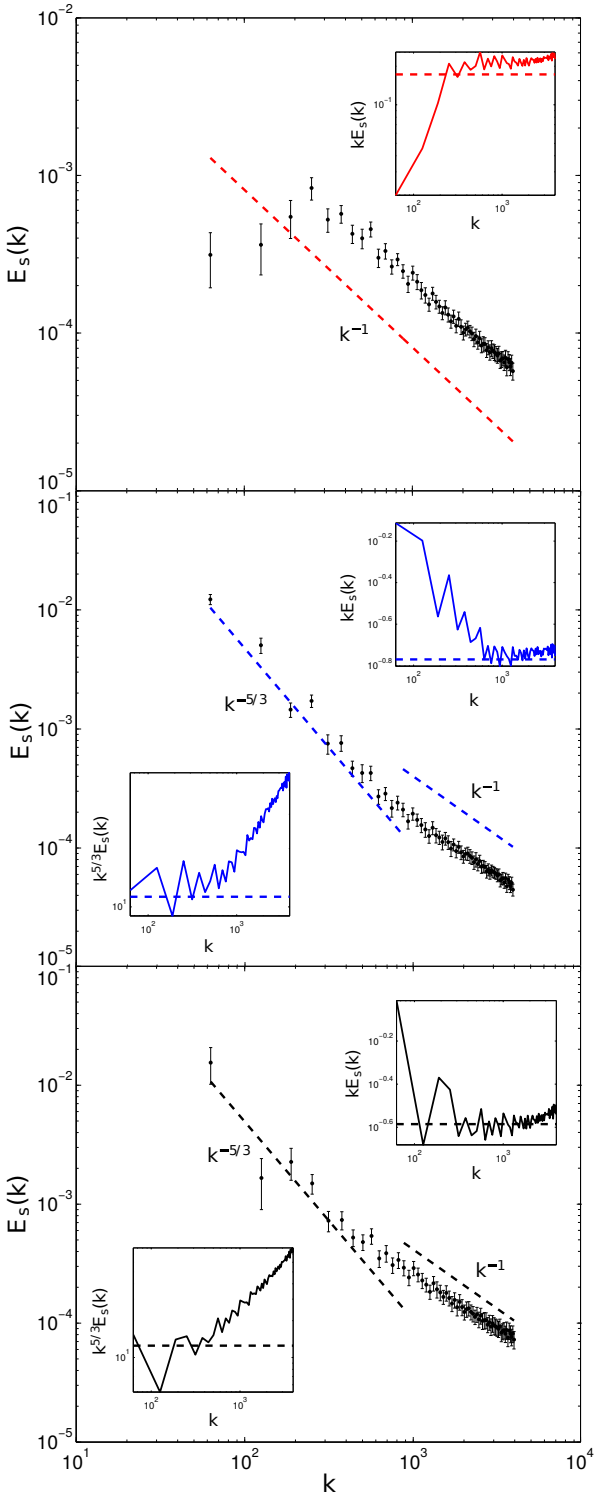


Figure 4.6: (color online). Energy spectrum $E(k)$ (arbitrary units) vs wavenumber $k$ (cm$^{-1}$) (time averaged over the saturated regime) corresponding to vortex tangles generated by uniform normal fluid (model 1, top), synthetic normal fluid turbulence (model 2, middle) and frozen Navier-Stokes turbulence (model 3, bottom). The dashed lines indicate the $k^{-1}$ (top) and the $k^{-5/3}$ dependence (middle and bottom), respectively. Parameters as in Fig. (4.2). The compensated spectra $kE_s(k)$ and $k^{5/3}E_s(k)$ in the insets show the regions of $k$–space where the approximate scalings $k^{-1}$ and $k^{-5/3}$ apply.

A natural question to ask is whether our results are affected by the particular vortex reconnection algorithm used. In principle, both the large $k$ region and the small $k$ region of the spectrum could be affected: the former, because vortex reconnections involve changes of the geometry of the vortices at small length scales, the latter because the energy flux may be affected. To rule out this possibility we have performed simulations using the reconnection algorithm of Kondaurova et al. [Kondaurova *et al.*, 2008], which tests whether vortex filaments would cross each others path during the next time step (for details, see also ref. [Baggaley, 2012]). Fig. (4.7) is very similar to Fig. (4.6), confirming that the shape of the energy spectra does not depend on the reconnection algorithm.

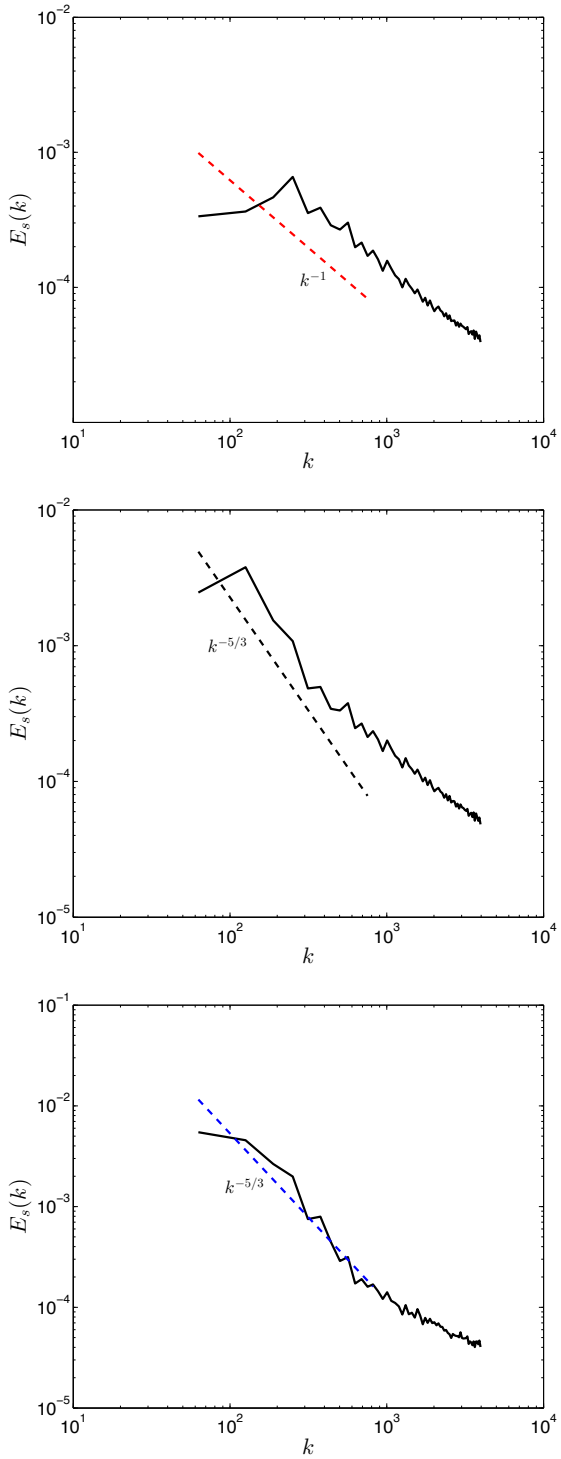


Figure 4.7: (color online). Energy spectrum $E(k)$ (arbitrary units) vs wavenumber $k$ (cm$^{-1}$) (time averaged over the saturated regime) as in Fig. (4.6), but the simulations are performed using the reconnection algorithm of Kondaurova et al. [Kondaurova *et al.*, 2008]. Note that there is no significant difference from spectra obtained using our standard algorithm, see Fig. (4.6). Vortex tangles generated by uniform normal fluid (model 1, top), synthetic normal fluid turbulence (model 2, middle) and frozen Navier-Stokes turbulence (model 3, bottom). The dashed lines indicate the $k^{-1}$ (top) and the $k^{-5/3}$ dependence (middle and bottom), respectively. Parameters: temperature $T = 1.9$ K, $V_n = 0.75$ cm/s (for model 1), Re = 81.59 (for model 2), and Re = 3025 (for model 3).

It is also instructive to examine the spatial distribution of the superfluid energy densities arising from the three normal fluid models: Fig. 4.8 displays the superfluid energy density $\epsilon_s = |\mathbf{v}_s|^2/2$ on the $xy$ plane averaged over $z$. The left panel (model 1, uniform normal flow) shows that $\epsilon_s$ is approximately constant, that is to say the vortex tangle is homogeneous; the middle and right panels (model 2 and 3 for synthetic normal flow turbulence and frozen Navier-Stokes turbulence) show that the energy density is increasingly nonhomogeneous, particularly model 3. The localised regions of large energy density correspond to vortex lines which are locally parallel to each other, reinforcing each other's velocity field rather than cancelling it out.

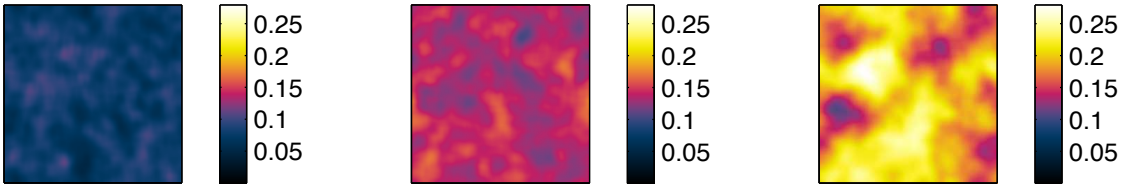


Figure 4.8: Superfluid energy density $\epsilon_s = |\mathbf{v}_s|^2/2$ smoothed over the average intervortex spacing $\ell$, plotted on the $xy$ plane and averaged over $z$. Left: model 1 (uniform normal fluid); middle: model 2 (synthetic turbulence); right: model 3 (frozen Navier-Stokes turbulence). Parameters as in Fig. (4.2).

The natural question which we ask is what is the cause of the spectral difference shown in Fig. 4.6. To answer the question we examine the local and nonlocal contributions to the superfluid velocity, defined according to Equation 2.25. Fig. 4.9 shows the fraction $v^{non}/v^{self}$ of the superfluid velocity which arises from nonlocal contributions, where $v^{non} =< |\mathbf{v}_{non}(\mathbf{s}_j)| >$ and $v^{self} =< |\mathbf{v}_{self}(\mathbf{s}_j)| >$ are sampled over the discretisation points $j = 1, \cdots N$ at a given time $t$. The difference is striking. Nonlocal effects are responsible for only 25 percent of the total superfluid velocity field in the tangle generated by the uniform normal fluid (model 1), for 45 percent in the tangle generated by synthetic normal flow turbulence (model 2), and for more than 60 percent in the tangle generated by frozen Navier-Stokes turbulence (model 3).

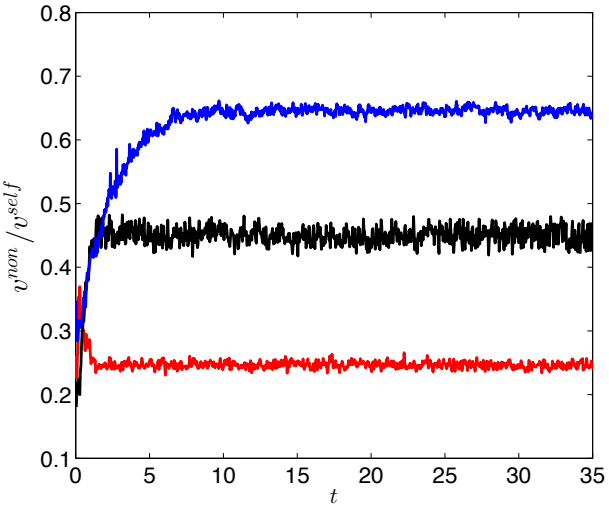


Figure 4.9: (colour online). Ratio of nonlocal to total self-induced velocity as a function of time $t$ (s) for tangles generated by uniform normal fluid (model 1, red line, bottom), synthetic normal fluid turbulence (model 2, black line, middle) and frozen Navier-Stokes turbulence (model 3, blue line, top). Parameters as in Fig. (4.2).

Finally, we explore the dependence of the result on the vortex line density $L$ by generating statistically steady states of turbulence driven by uniform normal fluid (model 1) and synthetic turbulence (model 2) with different values of $L$, see Fig. 4.10. Fig. 4.11 shows that for model 1 (uniform normal flow) the relative importance of nonlocal contributions remains constant at about 25 percent over a wide range of vortex line density, from $L \approx 6000$ to $L \approx 20,000$ cm$^{-2}$, whereas for model 2 (synthetic normal flow turbulence) and 3 (frozen Navier–Stokes turbulence), it increases with $L$.

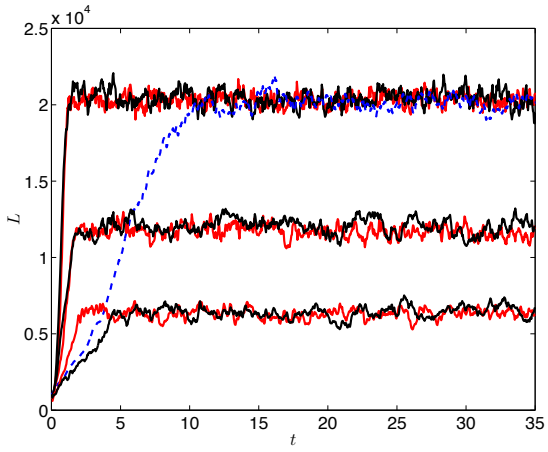


Figure 4.10: (color online). Evolution of the vortex line density $L$ (cm$^{-2}$) vs time $t$ (s) for model 1 (red line, uniform normal flow, respectively at $V_n = 1$ (cm/s) (top), $V_n = 0.75$ (cm/s) (middle) and $V_n = 0.55$ (cm/s) (bottom)), model 2 (black line, synthetic normal fluid turbulence, respectively at $Re = 79.44$ (top), $Re = 81.59$ (middle) and $Re = 83.86$ (bottom)), and model 3 (dashed blue line, frozen Navier-Stokes turbulence, at $Re = 3025$).

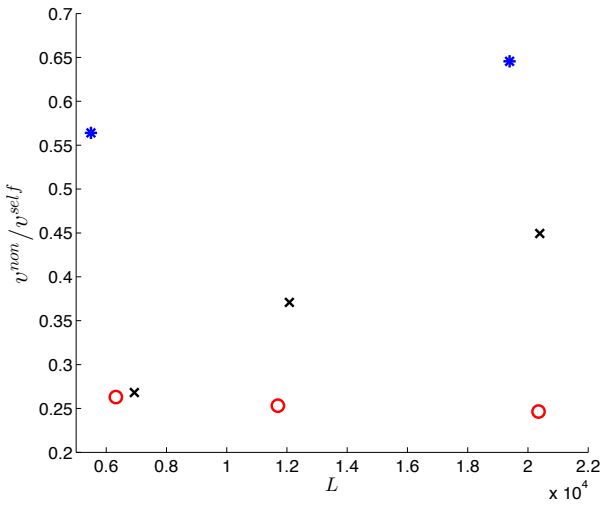


Figure 4.11: (color online). Ratio $v^{non}/v^{self}$ as a function of vortex line density $L$ (cm$^{-2}$) corresponding to model 1 (uniform normal flow, red circles), model 2 (synthetic normal flow turbulence, black crosses) and model 3 (frozen Navier-Stokes equation, blue stars).

## 4.3 Discussion

Turbulent vortex tangles can be produced in the laboratory using various means: by imposing a flux of heat, by pushing liquid helium II through pipes, or by stirring it with moving objects. The numerical experiments presented here show that reporting the vortex line density $L$ is not enough to characterise the nature of the superfluid turbulence

which can be generated in helium II. Vortex tangles with the same value of $L$ may have very different energy spectra, depending on the normal fluid flow which feeds energy into the vortex lines, as shown in Fig. 4.6. If the normal fluid is turbulent, energy is contained in the large eddies and is distributed over the length scales consistent with the classical $k^{-5/3}$ Kolmogorov law at large $k$, suggesting the presence of a Richardson cascade. If the normal fluid is uniform, most of the energy is contained at the intermediate length scales, and the energy spectrum scales consistently with $k^{-1}$ at large $k$. Using a terminology already in the literature, we identify these two forms of superfluid turbulence as 'Kolmogorov tangles' and 'Vinen tangles' respectively.

The superfluid velocity field is determined by the instantaneous configuration of vortex lines. Since the superfluid velocity field decays only as $1/r$ away from the axis of a quantum vortex line, the interaction between vortex lines is long-ranged, at least in principle. By examining the ratio of local and nonlocal contributions to the total velocity field, we have determined that in Vinen tangles far-field effects tend to cancel out ($v_s^{non}/v_s^{self} \approx 25\%$ independently of $L$), the motion of a vortex line is mainly determined by its local curvature, and the vortex tangle is homogeneous. In Kolmogorov tangles, on the contrary, nonlocal effects are dominant and increase with the vortex line density; this stronger vortex-vortex interaction leads to the clustering of vortex lines, for which the vortex tangle is much less homogeneous and contains coherent vorticity regions, in analogy to what happens in ordinary turbulence. The presence of intermittency effects such as coherent structures in the driving normal fluid, which we have explored with model 3, enhances the formation of superfluid vortex bundles, resulting in a more inhomogeneous superfluid energy and in larger nonlocal contributions to the vortex lines' dynamics.

Future work will explore the problem for turbulence with nonzero mean flow.

# Chapter 5

# Fluctuations of the vortex line density

## 5.1 Motivation

In 2011 Baggaley and Barenghi [Baggaley & Barenghi, 2011*b*] sought to numerically reproduce the findings of Roche et al. in 2007 [Roche *et al.*, 2007] where they measured the fluctuations of the vortex line density $L$ in turbulent $He^4$ and observed that the frequency spectrum scales as $f^{-5/3}$ (where $f$ is the frequency). This result was surprising as it appeared to contradict the common interpretation of $L$ as a measure of the superfluid vorticity $\omega = \kappa L$ [Vinen & Niemela, 2002; Skrbek & Sreenivasan, 2012; Stalp *et al.*, 1999].

Classically we would expect the enstrophy (the square of the vorticity) spectrum to scale as $k^2E(k)$ [Farge *et al.*, 2003], and hence naively one may expect the fluctuations of the vortex line density to scale as $f^{1/3}$. A resolution to this apparent paradox was put forward by Roche and Barenghi [Roche & Barenghi, 2008] who argued that the vortex line density could be decomposed into two parts, such that

$$L(\mathbf{x}, t) = L_{\times}(\mathbf{x}, t) + L_{\parallel}(\mathbf{x}, t), \tag{5.1}$$

where $L_{\parallel}$ represents 'structured' vortex line density, i.e. vortices organised into bundles which are responsible for the Kolmogorov scaling. In contrast $L_{\times}(\mathbf{x}, t)$ contributes to the vortex line density but not to the superfluid vorticity and reflects randomly oriented vortex lines. They then made the assumption that the velocity field is dominated by the velocity induced by the coherent vortex line density, and so in effect $L_{\times}$ acts like a passive vector field. It has been shown numerous times [Antonia *et al.*, 1998] that passive vectors (advected by a turbulent flow) have a power spectrum which obeys the Kolmogorov scaling law, and this formed the basis of their explanation of the observed power spectrum of the

vortex line density.

Baggaley and Barenghi studied the spectral properties of the volume integrated line density for quantum turbulence driven by a disordered normal fluid. In addition they also considered passive vortex lines (effectively setting $\kappa = 0$). Their results supported the argument put forward by Roche and Barenghi. However, in response to this publication Roche put forward an argument [Roche, 2012] that the good correlation of his results and those of Baggaley and Barenghi might have been influenced by a filtering effect induced when they interpreted the spectra of the volume integrated line density. Roche suggested the effect of this volume integration would tend to act as a low pass filter on the data and therefore small scale motions would be averaged out causing a steepening of the spectrum. Here we seek to address these issues and provide substantial numerical agreement with Roche.

## 5.2 Implementation

In order to establish whether this filtering effect existed and if it existed to what extent it impacted on a proper understanding of the results we use our numerical model as outlined in Chapter 2 and set up two types of simulation.

We conducted one run with a uniform normal fluid setup to simulate an experiment with counterflow where there would be a small heat flux applied at one end of the channel [Vinen, 1957*b*] and another where we set up a frozen Navier-Stokes normal fluid (fully detailed in Chapter 4) to simulate an experiment with a turbulent normal fluid such as turbulence generated by stirring the helium with grids [Smith *et al.*, 1993] or by using bellows or plungers to push the helium through pipes or channels [Salort *et al.*, 2010; Maurer & Tabeling, 1998].

For both simulations we conduct our numerics in a periodic box of size $D = 0.1$ cm with a numerical discretisation resolution of $\delta = 0.0016$ cm, at a temperature realistic for physical experiments of $T = 1.9$ K (which corresponds to the temperature dependent friction coefficients being $\alpha = 0.206$ and $\alpha = 0.00834$). We use an Adams-Bashforth time-stepping algorithm to move our vortices with a time step of $\Delta t = 5 \times 10^{-5}$ s and we deploy our tree algorithm to resolve the Biot-Savart integral with an opening angle of $\theta = 0.4$.

Our chosen model for counterflow turbulence is the most commonly used in the literature [Schwarz, 1988; Adachi *et al.*, 2010] and we impose a uniform normal fluid velocity of

the form $\mathbf{v}_n^{ext} = V_n\hat{\mathbf{x}}$ in the x-direction (which we take to be the direction of the channel) where $V_n = 1$ cm/s. To uphold the conservation of mass we add a uniform superflow of the form $\mathbf{v}_s = -(\rho_n/\rho_s)V_n\hat{\mathbf{x}}$ in the opposite direction. We then solve our equations of motion Eqs. (2.1) and (2.25) in the imposed superflows reference frame.

Our chosen model for a turbulent normal fluid is obtained by a direct numerical simulation (DNS) of the classical Navier-Stokes equation (see equation 1.1), however as the simultaneous calculation of the superfluid vortices and the turbulent normal flow would be computationally too expensive we choose to limit ourselves to a single time snapshot of $\mathbf{v}_n^{ext}$ the data for which was obtained from the John Hopkins Turbulence Database [Li *et al.*, 2008*a*,*b*] originally for the work done in Chapter 4. The Reynolds number of our normal fluid is $R_e = 3205$ which is estimated from the ratio of the integral scale $L_0$ and the Kolmogorov microscale $\eta_0$ as $R_e = (L_0/\eta_0)^{4/3}$. In order that the computational time be kept to a reasonable period we rescaled the velocity components of our DNS snapshot to about 60% of their original values. Note, this flow is no longer a solution to the Navier-Stokes Equation, but it is sufficient for our purposes.

To measure the intensity of our superfluid tangles we use the vortex line density $L$. We allow the model sufficient time to fully saturate (such that the line density achieved is of the order of $\bar{L} = 20,000\text{cm}^{-2}$) and choose a sufficiently long observation period over which to take our measurements. Figure 5.1 shows our line density developing over time with a fully saturated model for both achieved by $t = 10$ s. Once saturated we observe a mean line density with clear fluctuations about it.

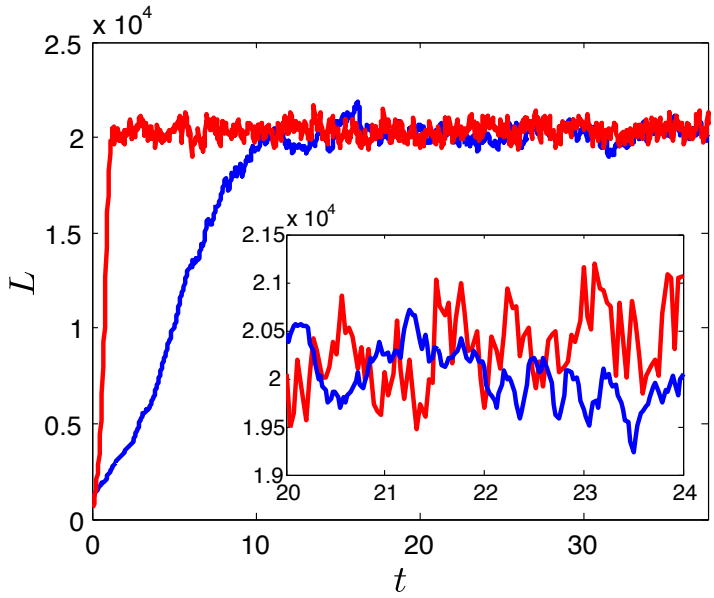


Figure 5.1: Vortex line density $L$ (cm$^{-2}$) plotted as a function of time $t$ ($s$) for counterflow turbulence (red line) and frozen Navier-Stokes turbulence (blue line). The inset highlights the fluctuations of $L$ vs $T$ in greater detail. Parameters: $V_n = 1$ cm/s for the counterflow simulation and $Re = 3025$ for the frozen Navier-Stokes simulation.

## 5.3 Results

To examine the distribution of the kinetic energy over the length scales within our flow we extract a three dimensional snapshot of the superfluid velocity $\mathbf{v}_s$ on a $1024^3$ mesh and use a Fourier-transform to compute the energy spectra $E_s(k)$ which for isotropic turbulence is defined by

$$\frac{1}{V}\int_V \frac{1}{2}\mathbf{v}_s^2 dV = \int_0^\infty E_s(k)dk, \tag{5.2}$$

where $V$ is the volume of our periodic cube, $k = |\mathbf{k}|$ and $|\mathbf{k}|$ is the three dimensional wavenumber. Figure 5.2 shows our results. It is clear that the spectrum from the frozen Navier-Stokes turbulence (on the RHS of Fig 5.2) demonstrates the classical Kolmogorov $k^{-5/3}$ scaling for $k < k_\ell$ (where $k_\ell = 2\pi/\ell$ is the wavenumber corresponding to the typical inter-vortex spacing $\ell$), and that the kinetic energy is concentrated at the largest scales in our flow i.e. at small $k$. The results for the spectrum generated using our uniform normal flow (shown on the LHS of Fig 5.2) do not demonstrate any Kolmogorov scaling, rather they show the shallower $k^{-1}$ dependence typical of individual vortex lines at large wave numbers. The concentration of the kinetic energy within the intermediate scales indicates that within this flow no large scale motions are being generated.

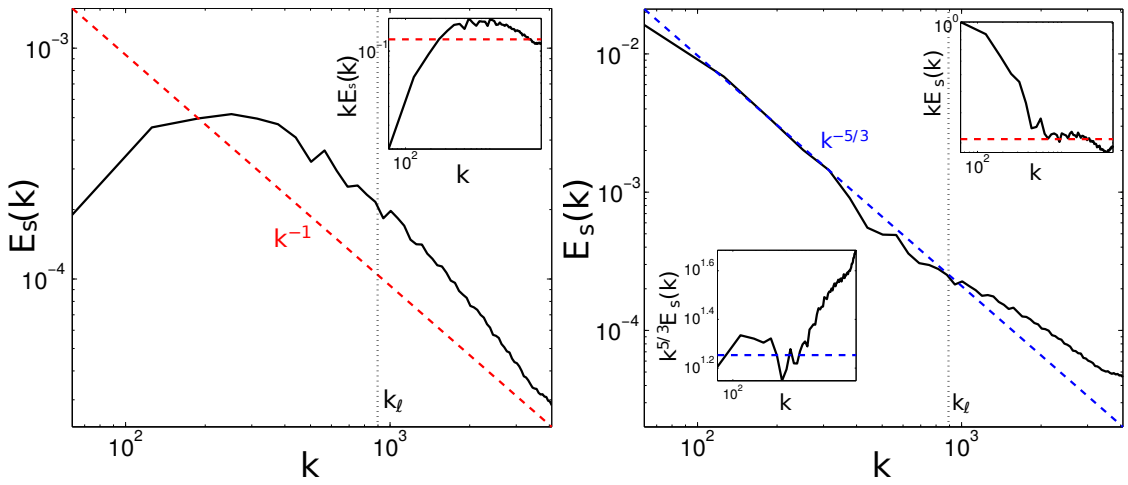


Figure 5.2: Energy spectrum $E(k)$ (arbitrary units) vs wavenumber $k$ (cm$^{-1}$) corresponding to vortex tangles generated by a counterflow (left) and frozen Navier-Stokes turbulence (right). The coloured dashed lines indicate the $k^{-1}$ (left) and the $k^{-5/3}$ dependence (right), respectively and the vertical dotted line marks $k_\ell = 2\pi/\ell$. Parameters as in Fig. (5.1). The compensated spectra $kE_s(k)$ and $k^{5/3}E_s(k)$ in the insets show the regions of $k$–space where the approximate scalings $k^{-1}$ and $k^{-5/3}$ apply.

In his experiment Roche used a newly devised micromachined second-sound probe to measure the spectrum of the fluctuations of the vortex line density in turbulent He$^4$ at a temperature of $T = 1.6$K. He did this by interpreting the attenuation of second-sound on the static 'no flow' frequency of the probe. The volume in which Roche took his measurements was estimated to be $V_c \simeq 1\text{mm} \times 1\text{mm} \times 250\mu\text{m} = 0.25$ mm$^3$ and the total turbulent flow approximately occupies the volume of $10^5$ mm$^3$ (in a cylinder with diameter 23mm and length 250mm), so clearly Roche's probe was measuring in a very much smaller volume than that of the total cylinder.

To produce our spectra of the fluctuations of the vortex line density we analyse four signals for each simulation, the first signal is measured over the entire periodic box which has length $d_1 = 0.1$. For the second signal we half the length of the box in which we take our measurements and so $d_2 = d_1/2 = 0.05$, and so on for the third signal where $d_3 = 0.025$ and the fourth signal where $d_4 = 0.0125$. We begin by measuring the total vortex line density within our cube (this was the approach of Baggaley and Barenghi in 2011) at over 1000 discrete and equal time-steps (this is actually the signal which is seen in Figure 5.1), we then discard the transient period of the vortex line density as our interest here is in the steady-state turbulence. Subsequently we measure the average vortex line density $\bar{L}$ and subtract this from our signal leaving us with only the fluctuations of the vortex line density. It is this signal which is then Fourier transformed to create our spectrum of the vortex line density fluctuations. As we increase the resolution of our probe by reducing

our measurement volume to one eighth of its previous volume, we repeat our measurement and analysis process. At each resolution of our probe we confirm that average vortex line density is consistent with that of the volume as a whole to establish that the resolution is not so fine as not to be representative of the flow in total. We plot these results in Figure 5.3.

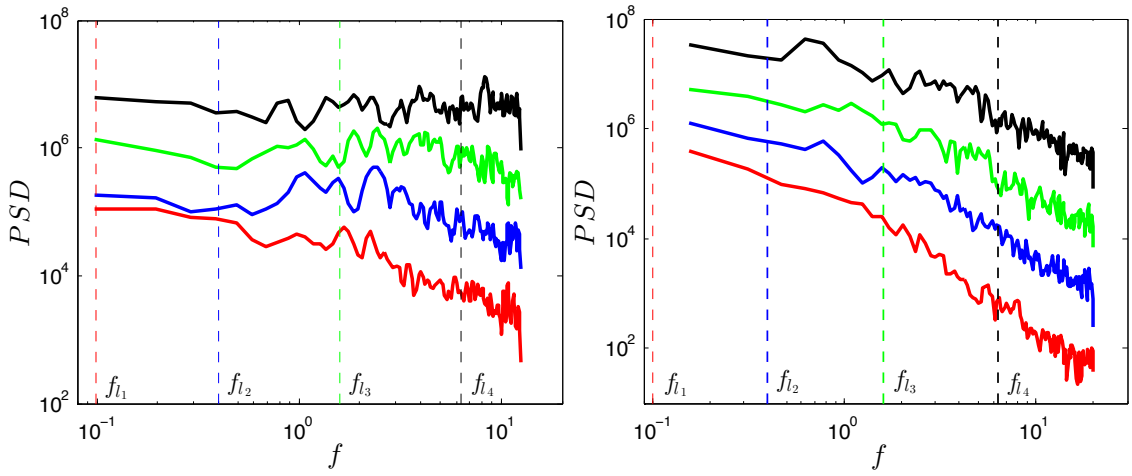


Figure 5.3: Power spectral density $PSD$ (arbitrary units) of the fluctuations of the total vortex line density $L$ for counterflow turbulence (left) and frozen Navier-Stokes turbulence (right), measured within box sizes ($d_i$) (from bottom to top): $d_1 = D = 0.1$ (red line), $d_2 = 0.05$ (blue line), $d_3 = 0.025$ (green line), $d_4 = 0.0125$ (black line). Dashed verticals are calculated as: $f_{\ell_i} = \kappa/d_i^2$

Examining Figure 5.3 it is clear that the volume in which the fluctuations signal is measured does indeed have an effect on the spectrum produced. Table 5.1 attempts to quantify the scale of the difference observed. We should note that the coloured dashed vertical lines marked $f_{\ell_i}$ refer only to their corresponding signal (e.g. the black vertical line $f_{\ell_4}$ should only be looked at in conjunction with the black signal for box size $d_4$).

| | Counterflow | Frozen Navier-Stokes |
|---|---|---|
| $\alpha_1$ | -1.6168 | -2.5263 |
| $\alpha_2$ | -1.1749 | -2.2076 |
| $\alpha_3$ | -0.51558 | -1.9269 |
| $\alpha_4$ | -0.085651 | -1.6053 |

Table 5.1: Measured values of the slopes, where $\alpha_i$ is the slope for signal $d_i$ from the point $f_{\ell_3}$ to the end point in figure 5.3.

When viewing the fluctuations spectrum for a particular box size $d_i$ we have thus areas to the right and to the left of the corresponding vertical $f_{\ell_i}$. We say that the scales to

the right, representing as they do motions which are smaller than the box size, are likely to be affected by any filtering whereas the scales to the left are unlikely to be affected by such filtering.

Shown on the LHS of figure 5.3 are the spectra for our uniform normal fluid simulation. If we were to only measure the signal over the entire volume of our periodic cube we would see a sloping spectrum (see the red trace) indicating behaviour within the flow. As we reduce our probe size moving through the blue and green traces we see that by the time our probe is reduced to around 0.2% of the original volume, as seen in the black trace, we have a flat, featureless spectrum.

Shown on the RHS of figure 5.3 are the spectra for our frozen Navier-Stokes normal fluid simulation. As we reduce our probe size moving again from the red trace through the blue and green traces to the black trace we maintain a slope albeit reduced in gradient. If we look at figure 5.4 which shows the compensated spectra we note that the black trace does flatten out and exhibit good agreement with the $f^{-5/3}$ spectrum seen by Roche.

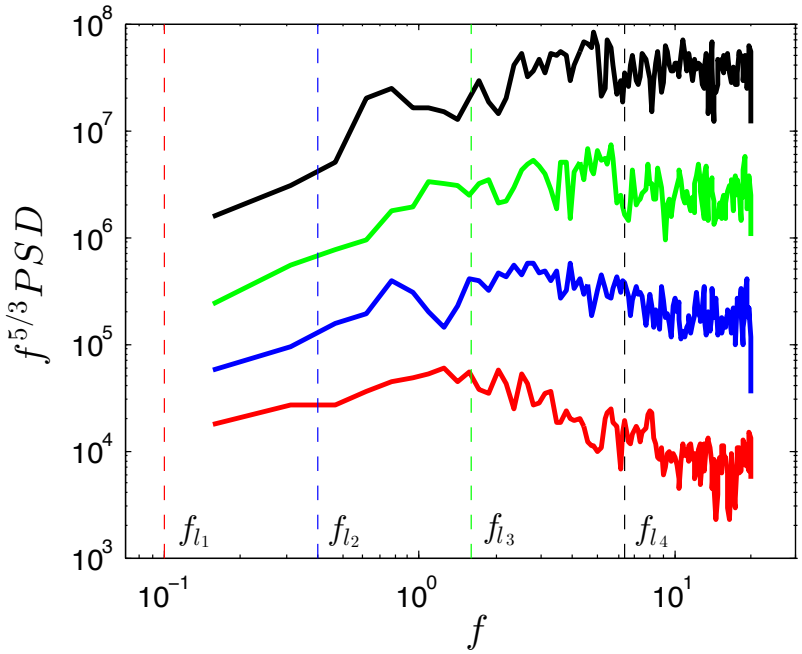


Figure 5.4: Compensated power spectral density $f^{5/3}PSD$ (arbitrary units) of the fluctuations of the total vortex line density $L$ for frozen Navier-Stokes turbulence. Parameters as in Fig. (5.3)

.

Given the very clear difficulty that physical experimentalists have in taking measurements at sufficiently varied spaces within their apparatus, in 1938 Taylor put forward his

hypothesis that makes the assumption that the advection contributed by the small scale eddies/fluctuations must be much less than that of the advection by the large scale mean flow (which is where the majority of the energy within the flow is contained) and therefore any advection of a turbulent field past a fixed point can be considered to be a consequence of the mean flow and not the fluctuations. This hypothesis, where applicable, allows experimentalists to infer information about their spatial structure based on time-series data measured in a single point. Thus it might be possible for an experimentalist, adopting Taylor's hypothesis to 'calculate' the total energy in their flow based on a time-series measurement of the velocity from a single probe at a single point in space.

It is a considerable benefit of the numerical modeller to have access to all elements and measurements of their data sets and this allows them to observe that which cannot (or cannot yet) be measured experimentally, as is the case with the Energy Spectrum $E_s(k)$. Our numerical modelling gives us access to simultaneous measurements of any output from our systems. Thus for example we can establish what the distribution of energy within the system is alongside determining the spectrum of the fluctuations of the vortex line density. By analysing these simultaneous results we can establish relationships and equivalence not available to the experimentalists. Thus it is, for example, we can say that there is a direct equivalence between the energy spectrum (not currently measured experimentally) and the spectrum of the fluctuations (which can be measured experimentally). Where we see an energy spectrum which exhibits a Kolmogorov $k^{-5/3}$ dependence we also see a fluctuations spectrum which shows a $f^{-5/3}$ dependence. Likewise, where we see an energy spectrum which exhibits a 'bump' at intermediate length scales followed by a $k^{-1}$ dependence at large wavenumbers we also see a flat and featureless fluctuations spectrum. Such information may assist the physical experimentalists in directing their work.

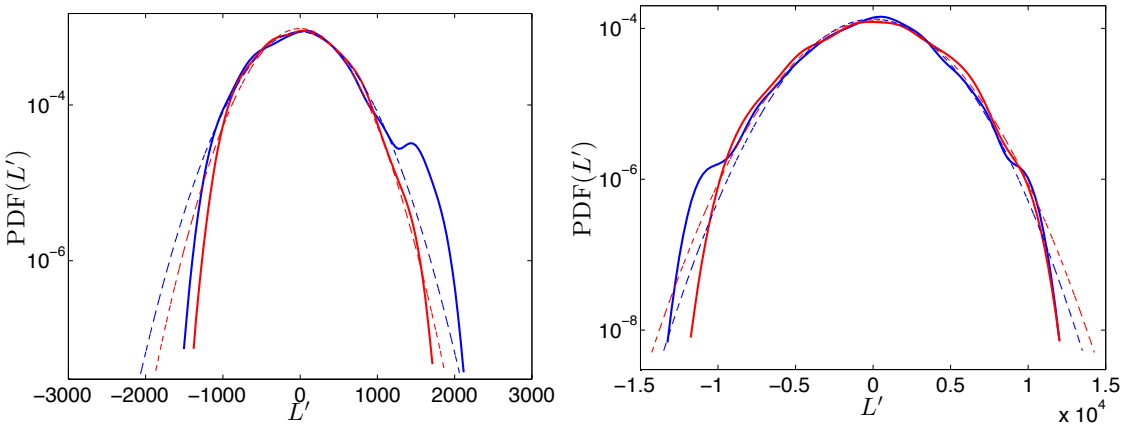


Figure 5.5: PDF's of vortex line density fluctuations for both the uniform normal fluid simulation (solid red lines) and the frozen Navier-Stokes simulation (solid blue lines), the dashed lines represent the theoretical normal distribution of the data. On the left is the PDF of the fluctuations signal taken over the whole cube for box length $d_1 = 0.1$ cm, where the standard deviations of the theoretical normals are $\sigma = 415.39$ for the uniform normal fluid and $\sigma = 459.15$ for the frozen Navier-Stokes normal fluid. The PDF on the right is taken from the signal measured in our cube representing around 1.6% of the entire volume where our box length is $d_3 = 0.025$ cm, the standard deviations of the theoretical normals are $\sigma = 3.2\times10^3$ for the uniform normal fluid and $\sigma = 3.0\times10^3$ for the frozen Navier-Stokes normal fluid.

Alongside examining the spectrum of the fluctuations of the vortex line density we also had a look at the PDF's of the fluctuations. Our results shown in Figure 5.5 demonstrate a clear normal distribution of the fluctuations. On the left of this figure we see the PDF for the fluctuations signal taken over the entire volume of our cube and on the right is the PDF of the less artificial fluctuations signal taken in a volume representing around 1.6% of the entire volume. We note that there is a much larger variance in the signal taken within the smaller volume and this is because we are no longer aggressively averaging over the 'true' fluctuation values.

## 5.4 Spatial structure of the vortex line density

So far we have been able to generate energy spectra from a time snapshot of our vortex tangles and we have been able to relate these to the spectra of the vortex line density fluctuations taken from a time-series signal (as they do experimentally). Ideally we would now like to obtain the spectra of the total vortex line density taken from an instantaneous snapshot of the vortex tangle as this would mean we would no longer be reliant on Taylor's frozen hypothesis. In order to do this we need the vortex line density $L$ as a continuous field. Unfortunately, despite using two different approaches we were not able to generate any meaningful spectra. We believe that the issue is a lack of scales between the largest scales in our computational box and the inter-vortex spacing $\ell$ and that the solution to

this problem will come only with the next generation of numerical models where 100 times as many vortex points may be feasible in a simulation. For completeness we set out below the approaches we took and such results as we were able to obtain, and although we were unable to make a giant leap forward, the data obtained and its analysis may provide a stepping-stone to further our understanding of the spatial distribution of the vortex line density.

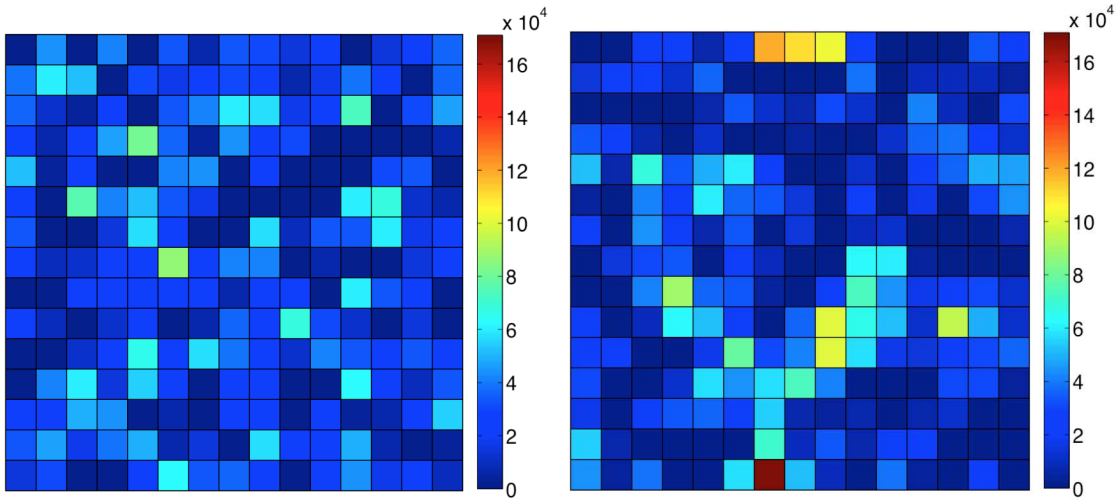


Figure 5.6: Vortex line density measured within a $16^3$ mesh, plotted on the $xy$-plane at $z = 0$ corresponding to counterflow turbulence (left) and frozen Navier-Stokes turbulence (right). The line density scales ($\mathrm{cm}^{-2}$) are shown at the right of each figure (plotted on the same scale for both left and right). Note the regions of much greater line density which are present in the frozen Navier-Stokes turbulence (right).

If we look at Figure 5.6 these are representations of our readings for the vortex line density taken across a slice of our computational cube. We obtain these density measurements by splitting our computational cube in to $16^3$ smaller cubes and measuring the total line length within each mini cube and dividing it by the volume of this mini cube. On the left of this figure we see the results for the counterflow turbulence and we can note that most of the values fall in the low density range with very few outliers in the mid-range. In contrast the illustration on the right which is taken from the frozen Navier-Stokes turbulence is populated with values from the lowest to the highest values and exhibits visual clustering. The visual cues from the counterflow turbulence figure (left) suggest a high number of relatively low density points evenly distributed throughout the system whereas the Navier-Stokes turbulence illustration (right) suggests contrasting regions of high and low density juxtaposed suggestive of bundling of the vortex lines.

We could view this data as a probability density function (PDF). This format would

allow us to capture more data by measuring over all z-values and not just a slice as in Figure 5.6. The PDF where all $16^3$ cubes in our computational box have been sampled is shown in Figure 5.7. We can readily see the maximum density obtained in the counterflow simulation (red line), where no values in excess of $10^5$ exist; in contrast the frozen Navier-Stokes simulation (blue line) has a higher and longer tail which tells us that there are more high-value densities found within this flow which is consistent with what we can see in Figure 5.6.

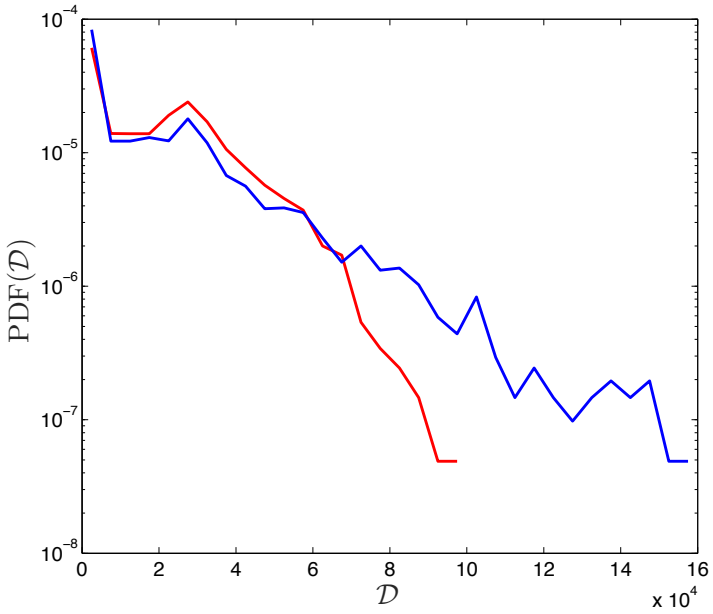


Figure 5.7: PDF of the vortex line density measured within a $16^3$ mesh for all $x$, $y$, $z$. $\mathcal{D}$ here represents the vortex line density measured in each of the 4096 mini cubes within the mesh.

Figure 5.6 represents a slice through our box which has been divided up in to 4096 ($16^3$) equal cubes, we can dramatically increase the resolution of our measurements by dividing the box in to a greater number of cubes. However when we do this with the 'standard' coarse-graining, the data is very noisy. An alternative is to use a more sophisticated technique to compute the smoothed line density $\langle L \rangle$. Dividing our computational box in to $128^3$ cubes and following a similar process to that used by Baggaley and Laurie [Baggaley *et al.*, 2012*c*] (which is one commonly employed in the smoothed particle hydrodynamics literature [Monaghan, 1992]) we define a smoothed line density field $\langle L \rangle$ at the discretisation points $\mathbf{s}_j$ using a kernel density smoothing:

$$\langle L(\mathbf{x})\rangle = \frac{1}{V}\sum_{j=1}^{N} W(r_j, h)\Delta\xi_j, \tag{5.3}$$

where $r_j = |\mathbf{x} - \mathbf{s}_j|$, $\Delta\xi_j = |\mathbf{s}_{j+1} - \mathbf{s}_j|$, $W(r,h) = g(r/h)/(\pi h^3)$, $h$ is a characteristic length scale and

$$g(q) = \begin{cases} 1 - \frac{3}{2}q^2 + \frac{3}{4}q^3, & 0 \le q < 1; \\ \frac{1}{4}(2-q)^3, & 1 \le q < 2; \\ 0, & q \ge 2. \end{cases} \tag{5.4}$$

Setting $h = \ell$, the smoothed line density field only takes in to account the contribution of discretisation points within a radius $2\ell$ from each point $\mathbf{x}$. Figure 5.8 (bottom row) represents our smoothed vortex line density $\langle L\rangle$ plotted at an isosurface level $\langle L\rangle > 2.5L_{rms}$ where $L_{rms} = \sqrt{\frac{1}{N}\sum_{i=1}^{N}|\langle L\rangle|^2}$.

The two illustrations on the top of Figure 5.8 represent the same snapshot plotted more traditionally as vortex lines. Although the illustrations at the top row of Figure 5.8 are clearly different they are not obviously hugely dissimilar. In contrast following our smoothing technique the illustrations on the bottom row make it very clear that in the counterflow turbulence (on the left) we have an evenly distributed, random topology, whereas for the frozen Navier-Stokes we have a very obvious well defined bundling of the vortices.

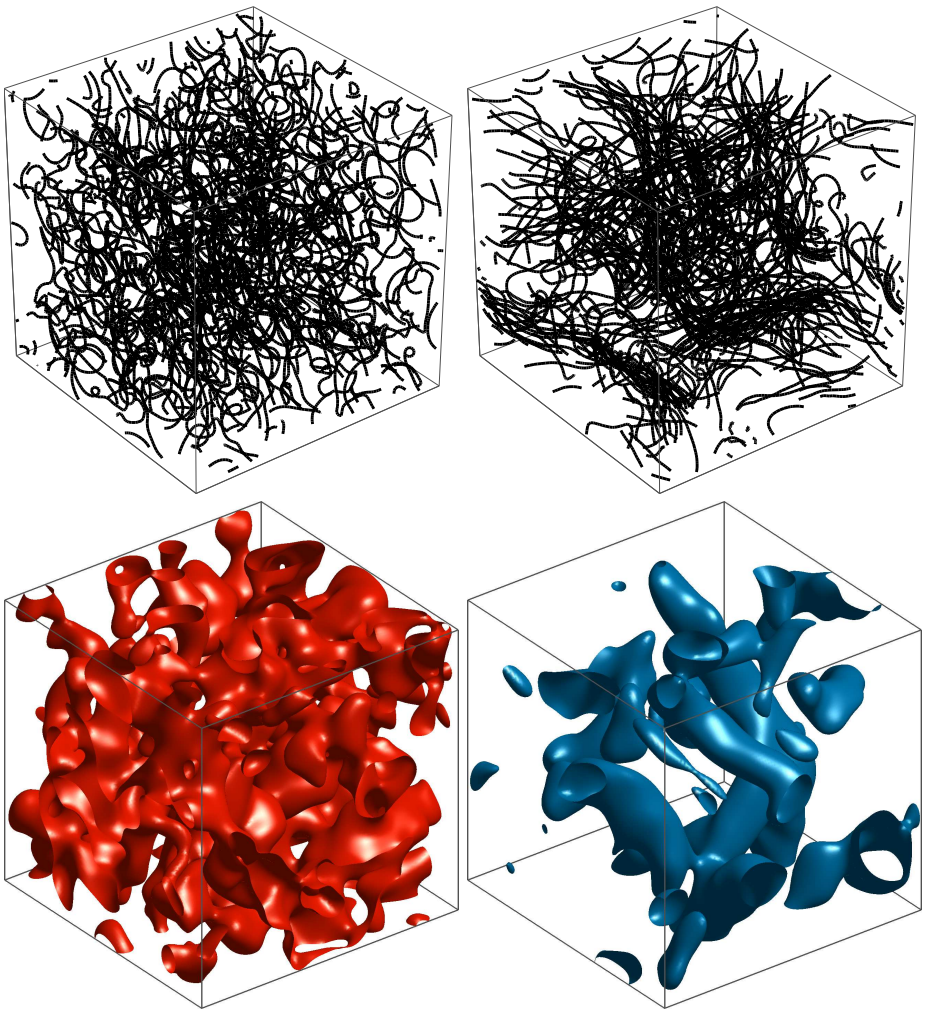

Figure 5.8: Top: Snapshot of the vortex configuration for counterflow turbulence (left) and frozen Navier-Stokes turbulence (right) taken once the simulations are in a statistically steady state. Bottom: Smoothed line density sustained by counterflow turbulence (left) and frozen Navier-Stokes turbulence (right). All four snapshots are taken from the same perspective at the same time.

## 5.5 Summary

This work has provided very strong support for Roche's experimental work where he quite unexpectedly found an $f^{-5/3}$ scaling in the spectrum of the vortex line density fluctuations. Roche's reluctance to accept the initial results of Baggaley and Barenghi lead us to further work on the modelling of his experiment, and revealed the 'filtering' effect which he suspected might be operating on the data. This filtering effect which has become apparent through our work and which is attributed to the finite size of the probe, is new to the field and has not been taken in to account in the previous experimental and theoretical literature.

As a by-product of our work to test and ultimately validate Roche's initial findings, we have found further evidence of differences in the Kolmogorov (or Quasi-classical) turbulence and Vinen (or Ultra-quantum) turbulence of helium II.

Where we have Kolmogorov turbulence as evidenced by the Kolmogorov scaling of the energy spectrum, we have found a $f^{-5/3}$ dependence in the spectrum of the fluctuations of the vortex line density. This confirms the idea of Roche and Barenghi [Roche & Barenghi, 2008] which was supported by Baggaley and Laurie [Baggaley *et al.*, 2012*c*] that the vortex line density behaves like a classical passive vector field which is known to have a power spectrum which exhibits the $f^{-5/3}$ scaling [Ohkitani, 2002]. We have also observed perhaps our clearest visual evidence yet for bundling within the superfluid turbulence.

Where we have observed Vinen turbulence as evidenced by the $k^{-1}$ scaling of the energy spectrum at high $k$ with a clear peak at the intermediate scales, we have found a flat, featureless spectrum of the fluctuations along with clear visuals of a randomly orientated, and 'evenly' distributed vortex tangle.

# Chapter 6

# Conclusions

No matter how we set about measuring it and no matter the initial setup and apparatus, our superfluid turbulence manifests itself in two distinct forms.

Perhaps the most accessible and understandable of these is what we term Quasiclassical or Kolmogorov turbulence. This has characteristics that, if not the same as, are certainly analogous to those found in classical turbulence and hence the name. Less accessible and perhaps therefore all the more intriguing is the other form of superfluid turbulence namely, Ultraquantum turbulence, sometimes referred to as Vinen turbulence.

My studies have for the most part concentrated on relatively high temperatures for the field, but have consistently demonstrated the presence of these two types of turbulence. We have 'lifted the fingerprints' of turbulence in many different scenarios and the evidence for the existence of the two forms of turbulence is irrefutable.

In our simulations where we seek to replicate experiments performed with either grids or propellors we generate our quasiclasscial turbulence which we promote by using either a synthetic turbulence (KS flow) or a frozen DNS (spatially varying but fixed in time DNS simulation) to model the normal fluid drive. In doing this we observe a distinctly structured tangle with dense bundles of near parallel vortices and we have found that non-local effects are very important in helping to generate these bundles. We have observed a 'Kolmogorov' energy spectrum implying a cascade of energy from large to small scales.

In contrast, when we replicate thermal counterflow experiments (in a T1 state) by using a uniform normal fluid to drive our simulations, we generate ultraquantum turbulence. Here we observe properties which accord very well with Vinen's original intuition. We find disordered, random tangles, where nonlocal effects play very little role and hence

no bundles are generated. Without these bundles we do not find energy at the largest scales and we observe an energy spectrum with a distinct 'bump'. From this we can infer that there is no cascade of the energy from the large to small scales.

Our main investigative tool for the identification of our two forms of superfluid turbulence has been the energy spectrum. Work at lower temperatures carried out in 2008 in Manchester by Walmsley and Golov [Walmsley & Golov, 2008] used a different approach to this type of investigation in actual physical experiments. Here they chose to measure the rate of decay of their tangles. Perhaps unsurprisingly, but certainly reassuringly, they too found evidence of the two distinct forms of turbulence we encounter.

Walmsley and Golov created their turbulence by injecting ions into the helium II, where each induces a vortex ring which eventually interacts with others to form tangles. For a prolonged period of initial ion injection ($> 30s$), tested at temperatures above $0.7K$ these tangles are quasiclassical and identical to those produced mechanically. For much shorter periods of ion injection (typically between $0.1 - 1s$) at temperatures below $0.5K$ the generated tangles are ultraquantum in nature. In measuring the decay of these tangles they found both the $t^{-3/2}$ fingerprint associated with quasiclassical turbulence and the $t^{-1}$ fingerprint of ultraquantum turbulence.

A useful piece of work published by Baggaley et al. [Baggaley *et al.*, 2012*a*] in 2012 nicely demonstrates the link between Walmsley's tangle decay rates and the energy spectra which have been the principal focus of this work. Baggaley simulates Walmsley and Golov's experiments and obtains the same decay that Walmsley saw but he was also able to see the energy spectrum, something not available to Walmsley. Where Baggaley observed the $t^{-1}$ decay of Walmsley, he also observed the same energy spectrum with a 'bump' obtained in our work. Similarly, where Baggaley observed the $t^{-3/2}$ decay of Walmsley, he also observed the same 'Kolmogorov' energy spectrum obtained in our work.

Given the close match between our energy spectra and those obtained by Baggaley in mirroring Walmsley's work, it is reasonable to conclude that we are all observing one and the same thing. It seems highly likely that our T1 counterflow simulations, driven as they are by an anisotropic normal fluid, are themselves then an anisotropic form of the Ultraquantum/Vinen turbulence observed by Walmsley and in general the energy dissipation of Walmsley's turbulence at very low temperatures has the same fingerprint as our turbulence at much higher temperatures. Given the absence of any friction forces at low temperature to assist energy decay it is perhaps surprising that the fingerprints match.

# Appendix A

# Biot-Savart derivation

We begin with vorticity, $\boldsymbol{\omega} = \nabla \times \mathbf{v}$.
We want to get $\mathbf{v}$ from $\boldsymbol{\omega}$:
For an incompressible flow we have $\nabla \cdot \mathbf{v} = 0$.
This means we can say $\mathbf{v} = \nabla \times \mathbf{a}$ (where $\mathbf{a}$ is the vector potential)
($\mathbf{a}$ can be chosen such that $\nabla \cdot \mathbf{a} = 0$).
Thus:

$$\begin{aligned}
\boldsymbol{\omega} &= \nabla \times \mathbf{v} \\
&= \nabla \times (\nabla \times \mathbf{a}) \\
&= \nabla(\nabla \cdot \mathbf{a}) - \nabla^2 \mathbf{a} \qquad \text{(we chose } \mathbf{a} \text{ such that } \nabla \cdot \mathbf{a} = 0) \\
\boldsymbol{\omega} &= -\nabla^2 \mathbf{a}.
\end{aligned}$$

This is a Poisson equation for $\mathbf{a}$ which has a well known solution given by a Greens Function, which is...

$$\mathbf{a} = -\frac{1}{4\pi} \int_V \frac{\boldsymbol{\omega}(\mathbf{s})}{|\mathbf{r} - \mathbf{s}|} dV,$$

(where $\mathbf{r} = (x, y, z)$ and $\mathbf{s}$ is a point on a space curve of infinitesimal thickness used to approximate a vortex line.)
Then since vorticity is just along $\mathbf{s}$ we can transform this in to a line integral, so $\boldsymbol{\omega}(\mathbf{s})dV = \kappa d\boldsymbol{\ell}$ where $\kappa$ is the circulation.
Thus we now have:

$$\mathbf{a} = -\frac{\kappa}{4\pi} \oint \frac{d\boldsymbol{\ell}}{|\mathbf{r} - \mathbf{s}|}.$$

Then,

$$\frac{d\mathbf{a}}{d\mathbf{r}} = -\frac{\kappa}{4\pi} \quad \frac{d\boldsymbol{\ell}}{|\mathbf{r} - \mathbf{s}|}.$$

If we now take the curl of this we obtain,

$$\begin{aligned}
\nabla \times \frac{d\mathbf{a}}{d\mathbf{r}} &= -\frac{\kappa}{4\pi} \quad \nabla \times \left( \frac{d\boldsymbol{\ell}}{|\mathbf{r}-\mathbf{s}|} \right), \\
\frac{d\ \nabla \times \mathbf{a}}{d\mathbf{r}} &= -\frac{\kappa}{4\pi} \quad \nabla \times \left( \frac{d\boldsymbol{\ell}}{|\mathbf{r}-\mathbf{s}|} \right), \\
\frac{d\mathbf{v}}{d\mathbf{r}} &= -\frac{\kappa}{4\pi} \left\{ \nabla \frac{1}{|\mathbf{r}-\mathbf{s}|} \times d\boldsymbol{\ell} + \frac{1}{|\mathbf{r}-\mathbf{s}|} \nabla \times d\boldsymbol{\ell} \right\}, \qquad \text{(using: } \nabla \times (\phi\psi) = \nabla\phi \times \psi + \phi \nabla \times \psi\text{)} \\
\mathbf{v} &= \oint -\frac{\kappa}{4\pi} \quad \nabla \frac{1}{|\mathbf{r}-\mathbf{s}|} \times d\boldsymbol{\ell}.
\end{aligned}$$

Aside: $\nabla |\mathbf{r}-\mathbf{s}|^{-1} = -|\mathbf{r}-\mathbf{s}|^{-2} \nabla |\mathbf{r}-\mathbf{s}| = -|\mathbf{r}-\mathbf{s}|^{-2} (\mathbf{r}-\mathbf{s})/|\mathbf{r}-\mathbf{s}| = -(\mathbf{r}-\mathbf{s})/|\mathbf{r}-\mathbf{s}|^{-3}$

Hence we have;

$$\begin{aligned}
\mathbf{v} &= \oint -\frac{\kappa}{4\pi} \quad \nabla |\mathbf{r}-\mathbf{s}|^{-1} \times d\boldsymbol{\ell}, \\
&= \oint -\frac{\kappa}{4\pi} \cdot \frac{-(\mathbf{r}-\mathbf{s})}{|\mathbf{r}-\mathbf{s}|^3} \times d\boldsymbol{\ell},
\end{aligned}$$

and finally we obtain the Biot-Savart Law which is:

$$\mathbf{v} = \frac{\kappa}{4\pi} \oint \frac{(\mathbf{r}-\mathbf{s})}{|\mathbf{r}-\mathbf{s}|^3} \times d\boldsymbol{\ell}.$$

# Appendix B

# Local induction approximation derivation

We begin with the Biot-Savart Law to describe the self-induced velocity ($\mathbf{v}$) of a vortex, where $\mathbf{s} = \mathbf{s}(\xi)$ is a curve which is used to represent a vortex filament, $\mathbf{r}$ represents a point on the curve, $\xi$ is the arclength between $\mathbf{s}$ and $\mathbf{r}$ and $\kappa$ is the circulation of the vortex. Integrating over $\ell$ means integrating over all the space curves.

$$\mathbf{v} = \frac{\kappa}{4\pi} \oint_{\ell} \frac{(\mathbf{s} - \mathbf{r})}{|\mathbf{s} - \mathbf{r}|^{\mathbf{3}}} \times d\mathbf{s}.$$

We then form a Taylor Series Expansion for $\mathbf{s}$ about the point $\mathbf{r}$ giving:

$$\mathbf{s} \simeq \mathbf{r} + \xi\mathbf{s}' + \frac{1}{2}\xi^2\mathbf{s}'' + ..., \tag{B.1}$$

differentiating this we obtain,

$$\frac{d\mathbf{s}}{d\xi} \simeq \mathbf{s}' + \xi\mathbf{s}'' + ... \Rightarrow d\mathbf{s} \simeq (\mathbf{s}' + \xi\mathbf{s}'' + ...)d\xi. \tag{B.2}$$

I can then rewrite equation B.1 as

$$\mathbf{s} - \mathbf{r} \simeq \xi\mathbf{s}' + \frac{1}{2}\xi^2\mathbf{s}'' + ..., \tag{B.3}$$

substituting equations B.2 and B.3 into the Biot-Savart Law gives:

$$\mathbf{v} \simeq \frac{\kappa}{4\pi} \oint_{\ell} \frac{(\xi\mathbf{s}' + \frac{1}{2}\xi^2\mathbf{s}'' + ...) \times (\mathbf{s}' + \xi\mathbf{s}'' + ...)}{|\xi\mathbf{s}' + \frac{1}{2}\xi^2\mathbf{s}'' + ...|^3} d\xi. \tag{B.4}$$

Aside: using the fact that $\mathbf{a}\times\mathbf{b} = -\mathbf{b}\times\mathbf{a}$ and that $\mathbf{a}\times\mathbf{a} = \mathbf{0} \Rightarrow$

$$\begin{aligned}(\xi\mathbf{s}' + \frac{1}{2}\xi^2\mathbf{s}'' + ...)\times(\mathbf{s}' + \xi\mathbf{s}'' + ...) &= \xi\mathbf{s}'\times\mathbf{s}' + \xi^2\mathbf{s}'\times\mathbf{s}'' + 1/2\xi^2\mathbf{s}''\times\mathbf{s}' + 1/2\xi^3\mathbf{s}''\times\mathbf{s}'' \\ &= 0 + \xi^2\mathbf{s}'\times\mathbf{s}'' - 1/2\xi^2\mathbf{s}'\times\mathbf{s}'' + 0 \\ &= 1/2\xi^2\mathbf{s}'\times\mathbf{s}''.\end{aligned}$$

We can now substitute the above back into equation B.4 to obtain,

$$\mathbf{v} \simeq \frac{\kappa}{8\pi}\mathbf{s}'\times\mathbf{s}''\oint_\ell \frac{\xi^2}{|\xi\mathbf{s}' + \frac{1}{2}\xi^2\mathbf{s}'' + ...|^3}d\xi. \tag{B.5}$$

Now using $|ab| = |a||b|$ we obtain,

$$\mathbf{v} \simeq \frac{\kappa}{8\pi}\mathbf{s}'\times\mathbf{s}''\oint_\ell \frac{\xi^2}{|\xi|^3|\mathbf{s}' + \frac{1}{2}\xi\mathbf{s}'' + ...|^3}d\xi. \tag{B.6}$$

Now we need to use $\mathbf{a}\cdot\mathbf{a} = |\mathbf{a}|^2 \Rightarrow |\mathbf{a}| = (\mathbf{a}\cdot\mathbf{a})^{1/2} \Rightarrow |\mathbf{a}|^3 = (\mathbf{a}\cdot\mathbf{a})^{3/2}$

$$\mathbf{v} \simeq \frac{\kappa}{8\pi}\mathbf{s}'\times\mathbf{s}''\oint_\ell \frac{|\xi|^{-1}}{((\mathbf{s}' + \frac{1}{2}\xi\mathbf{s}'' + ...)\cdot(\mathbf{s}' + \frac{1}{2}\xi\mathbf{s}'' + ...))^{3/2}}d\xi. \tag{B.7}$$

Then since

$$\begin{aligned}(\mathbf{s}' + \frac{1}{2}\xi\mathbf{s}'' + ...)\cdot(\mathbf{s}' + \frac{1}{2}\xi\mathbf{s}'' + ...) &= \mathbf{s}'\cdot\mathbf{s}' + \xi\mathbf{s}'\cdot\mathbf{s}'' + \frac{1}{4}\xi^2\mathbf{s}''\cdot\mathbf{s}'' \\ &= |\mathbf{s}'|^2 + \frac{1}{4}\xi^2|\mathbf{s}''|^2 \qquad \text{(using the fact that } \mathbf{s}' \text{ and } \mathbf{s}'' \text{ are orthogonal)} \\ &= 1 + \frac{\xi^2}{4R^2}, \qquad \text{(using } |\mathbf{s}'| = 1 \text{ and } |\mathbf{s}''| = R^{-1})\end{aligned}$$

This gives

$$\mathbf{v} \simeq \frac{\kappa}{8\pi}\mathbf{s}'\times\mathbf{s}''\oint_\ell |\xi|^{-1}(1 + \frac{\xi^2}{4R^2})^{-3/2}d\xi. \tag{B.8}$$

We can now use a negative binomial series expansion of the form $(1+x)^{-n} = 1 - nx + 1/2n(n+1)x^2 - ...$ to get

$$\begin{aligned}(1 + \frac{\xi^2}{4R^2})^{-3/2} &= 1 - \frac{3}{2}\frac{\xi^2}{4R^2} + \frac{1}{2}\frac{3}{2}\frac{5}{2}\frac{\xi^4}{16R^4} - ... \\ &= 1 - \frac{3\xi^2}{8R^2} + \frac{15\xi^4}{128R^4} - ...,\end{aligned}$$

Substituting this back into the integral gives

$$\begin{aligned}
\mathbf{v} &\simeq \frac{\kappa}{8\pi}\mathbf{s}' \times \mathbf{s}'' \oint_{\ell} |\xi|^{-1}(1 + O(\xi^2))d\xi \qquad \text{neglecting } O(\xi^2) \text{ terms} \\
\mathbf{v} &\simeq \frac{\kappa}{8\pi}\mathbf{s}' \times \mathbf{s}'' \oint_{\ell} |\xi|^{-1} d\xi \\
\mathbf{v} &\simeq \frac{\kappa}{8\pi}\mathbf{s}' \times \mathbf{s}'' \oint_{-\infty}^{\infty} \frac{1}{|\xi|} d\xi \\
\mathbf{v} &\simeq \frac{\kappa}{4\pi}\mathbf{s}' \times \mathbf{s}'' \oint_{0}^{\infty} \frac{1}{|\xi|} d\xi. \qquad \text{since } 1/|\xi| \text{ is an even function}
\end{aligned}$$

I need to create upper and lower limit cut-offs for this integral as it would produce $ln(0)$ and $ln(\infty)$ neither of which can happen so it makes more sense to use the core width $a_0$ as the lower limit and the radius of curvature $R$ as an upper limit. This gives...

$$\begin{aligned}
\mathbf{v} &\simeq \frac{\kappa}{4\pi}\mathbf{s}' \times \mathbf{s}'' \oint_{a_0}^{R} \frac{1}{|\xi|} d\xi \\
\mathbf{v} &\simeq \frac{\kappa}{4\pi}\mathbf{s}' \times \mathbf{s}'' \ln\left(\frac{R}{a_0}\right),
\end{aligned}$$

which is the local induction approximation.

# Bibliography


Aarts, R. 1993 A numerical study of quantized vortices in He II. PhD thesis.

Adachi, H., Fujiyama, S. & Tsubota, M. 2010 Steady-state counterflow quantum turbulence: Simulation of vortex filaments using the full biot-savart law. *Phys. Rev. B* **81**, 104511.

Alamri, S. Z., Youd, A. J. & Barenghi, C. F. 2008 Reconnection of superfluid vortex bundles. *Phys. Rev. Lett.* **101**, 215302.

Antonia, R. A., Zhou, T. & Zhu, Y. 1998 Three-component vorticity measurements in a turbulent grid flow. *Journal of Fluid Mechanics* **374**, 29–57.

Araki, T., Tsubota, M. & Nemirovskii, S. K. 2002 Energy spectrum of superfluid turbulence with no normal-fluid component. *Phys. Rev. Lett.* **89**, 145301.

Baggaley, A. 2012 The sensitivity of the vortex filament method to different reconnection models. *Journal of Low Temperature Physics* **168** (1-2), 18–30.

Baggaley, A. & Barenghi, C. 2012 Tree method for quantum vortex dynamics. *Journal of Low Temperature Physics* **166** (1-2), 3–20.

Baggaley, A. W. 2009 Flux rope dynamo. PhD thesis.

Baggaley, A. W. & Barenghi, C. F. 2011*a* Quantum turbulent velocity statistics and quasiclassical limit. *Phys. Rev. E* **84**, 067301.

Baggaley, A. W. & Barenghi, C. F. 2011*b* Vortex-density fluctuations in quantum turbulence. *Phys. Rev. B* **84**, 020504.

Baggaley, A. W., Barenghi, C. F. & Sergeev, Y. A. 2012*a* Quasiclassical and ultraquantum decay of superfluid turbulence. *Phys. Rev. B* **85**, 060501.

Baggaley, A. W., Barenghi, C. F., Shukurov, A. & Sergeev, Y. A. 2012*b* Coherent vortex structures in quantum turbulence. *EPL (Europhysics Letters)* **98** (2), 26002.

Baggaley, A. W. & Laurie, J. 2015 Thermal counterflow in a periodic channel with solid boundaries. *Journal of Low Temperature Physics* **178** (1), 35–52.

Baggaley, A. W., Laurie, J. & Barenghi, C. F. 2012*c* Vortex-density fluctuations, energy spectra, and vortical regions in superfluid turbulence. *Phys. Rev. Lett.* **109**, 205304.

Baggaley, A. W., Sherwin, L. K., Barenghi, C. F. & Sergeev, Y. A. 2012*d* Thermally and mechanically driven quantum turbulence in helium II. *Phys. Rev. B* **86**, 104501.

Barenghi, C., Donnelly, R. & Vinen, W. 1983 Friction on quantized vortices in helium II. A review. *Journal of Low Temperature Physics* **52** (3-4), 189–247.

Barenghi, C. & Samuels, D. 2004 Scaling laws of vortex reconnections. *Journal of Low Temperature Physics* **136** (5-6), 281–293.

Barenghi, C. F. & Donnelly, R. J. 2009 Vortex rings in classical and quantum systems. *Fluid Dynamics Research* **41** (5), 051401.

Barenghi, C. F., Donnelly, R. J. & Vinen, W. F. 1985 Thermal excitation of waves on quantized vortices. *Physics of Fluids* **28** (2), 498–504.

Barenghi, C. F., Samuels, D. C., Bauer, G. H. & Donnelly, R. J. 1997 Superfluid vortex lines in a model of turbulent flow. *Physics of Fluids (1994-present)* **9** (9), 2631–2643.

Barnes, J. & Hut, P. 1986 A hierarchical o(n log n) force-calculation algorithm. *Nature* **324** (6096), 446–449.

Bellows, A. 2014 Absolute zero. http://www.damninteresting.com/absolute-zero-is-0k, accessed: August 2015.

Benderskii, A. V., Zadoyan, R., Schwentner, N. & Apkarian, V. A. 1999 Photodynamics in superfluid helium: Femtosecond laser-induced ionization, charge recombination, and preparation of molecular rydberg states. *The Journal of Chemical Physics* **110** (3), 1542–1557.

Bewley, G. P., Lathrop, D. P. & Sreenivasan, K. R. 2006 Superfluid helium: Visualization of quantized vortices. *Nature* **441** (7093), 588–588.

Bradley, D. I., Fisher, S. N., Guenault, A. M., Haley, R. P., Pickett, G. R., Potts, D. & Tsepelin, V. 2011 Direct measurement of the energy dissipated by quantum turbulence. *Nat Phys* **7** (6), 473–476.

Childers, R. K. & Tough, J. T. 1976 Helium II thermal counterflow: Temperature- and pressure-difference data and analysis in terms of the Vinen theory. *Phys. Rev. B* **13**, 1040–1055.

Codoluto, D. & Dykhoff, D. 2014 Temperature Dependence of Second Sound in He-II. https://wiki.umn.edu/MXP/S14SpeedofSecondSound, accessed: August 2015.

Donnelly, P. H. R. R. J. 1970 Dynamics of vortex rings. *Physics Letters A* **31** (3), 137–138.

Donnelly, R. J. 1991 Quantized Vortices in Helium II. **346**.

Donnelly, R. J. 1999 Cryogenic fluid dynamics. *Journal of Physics: Condensed Matter* **11** (40), 7783.

Donnelly, R. J. & Barenghi, C. F. 1998 The observed properties of liquid helium at the saturated vapor pressure. *Journal of Physical and Chemical Reference Data* **27** (6), 1217–1274.

Faraday, M. 1823 On hydrate of chlorine. *Quarterly Journal of Science* **15** (71).

Farge, M., Schneider, K., Pellegrino, G., Wray, A. A. & Rogallo, R. S. 2003 Coherent vortex extraction in three-dimensional homogeneous turbulence: Comparison between cvs-wavelet and pod-fourier decompositions. *Physics of Fluids* **15** (10), 2886–2896.

Feynman, R. 1955*a* Chapter {II} application of quantum mechanics to liquid helium. *Progress in Low Temperature Physics*, vol. 1, pp. 17 – 53. Elsevier.

Feynman, R., Leighton, R. & Sands, M. 1964 *The Feynman Lectures on Physics: Mainly electromagnetism and matter. Volume 2*. Addison-Wesley Publishing Company.

Feynman, R. P. 1955*b* Application of quantum mechanics to liquid helium. *Progress in Low Temperature Physics* **1**, 17–53.

Frisch, U. 1995 *Turbulence: The Legacy of A. N. Kolmogorov.*. Cambridge University Press.

Fung, J. C. H., Hunt, J. C. R., Malik, N. A. & Perkins, R. J. 1992 Kinematic simulation of homogeneous turbulence by unsteady random fourier modes. *Journal of Fluid Mechanics* **236**, 281–318.

Fung, J. C. H. & Vassilicos, J. C. 1998 Two-particle dispersion in turbulentlike flows. *Phys. Rev. E* **57**, 1677–1690.

Gamet, L., Ducros, F., Nicoud, F. & Poinsot, T. 1999 Compact finite difference schemes on non-uniform meshes. application to direct numerical simulations of compressible flows. *International Journal for Numerical Methods in Fluids* **29** (2), 159–191.

Gnedin, N. Y., Glover, S. C. O., Klessen, R. S. & Springel, V. 2015 *Star Formation in Galaxy Evolution: Connecting Numerical Models to Reality*. Springer-Verlag Berlin Heidelberg.

Guo, W., Cahn, S. B., Nikkel, J. A., Vinen, W. F. & McKinsey, D. N. 2010 Visualization study of counterflow in superfluid $^4$He using metastable helium molecules. *Phys. Rev. Lett.* **105**, 045301.

Guo, W., La Mantia, M., Lathrop, D. P. & Van Sciver, S. W. 2014 Visualization of two-fluid flows of superfluid helium-4. *Proceedings of the National Academy of Sciences of the United States of America* **111**, 4653–4658.

Hall, H. E. & Vinen, W. F. 1956 The Rotation of Liquid Helium II. The Theory of Mutual Friction in Uniformly Rotating Helium II. *Proceedings of the Royal Society of London A: Mathematical, Physical and Engineering Sciences* **238** (1213), 215–234.

Hanninen, R. & Baggaley, A. W. 2014 Vortex filament method as a tool for computational visualization of quantum turbulence. *Proceedings of the National Academy of Sciences* **111** (Supplement 1), 4667–4674.

Kerr, R. M. 2011 Vortex stretching as a mechanism for quantum kinetic energy decay. *Phys. Rev. Lett.* **106**, 224501.

Kivotides, D. 2006 Coherent structure formation in turbulent thermal superfluids. *Phys. Rev. Lett.* **96**, 175301.

Kivotides, D. 2011 Spreading of superfluid vorticity clouds in normal-fluid turbulence. *Journal of Fluid Mechanics* **668**, 58–75.

Kivotides, D. 2015 Decay of finite temperature superfluid helium-4 turbulence. *Journal of Low Temperature Physics* **181** (1), 68–76.

Kivotides, D., Barenghi, C. F. & Samuels, D. C. 2000 Triple Vortex Ring Structure in Superfluid Helium II. *Science* **290** (5492), 777–779.

Kobayashi, M. & Tsubota, M. 2005 Kolmogorov spectrum of superfluid turbulence: Numerical analysis of the gross-pitaevskii equation with a small-scale dissipation. *Phys. Rev. Lett.* **94**, 065302.

Kolmogorov, A. 1941 The Local Structure of Turbulence in Incompressible Viscous Fluid for Very Large Reynolds' Numbers. *Akademiia Nauk SSSR Doklady* **30**, 301–305.

Kondaurova, L., Andryuschenko, V. & Nemirovskii, S. 2008 Numerical simulations of superfluid turbulence under periodic conditions. *Journal of Low Temperature Physics* **150** (3-4), 415–419.

Koplik, J. & Levine, H. 1993 Vortex reconnection in superfluid helium. *Phys. Rev. Lett.* **71**, 1375–1378.

Kozik, E. & Svistunov, B. 2004 Kelvin-wave cascade and decay of superfluid turbulence. *Phys. Rev. Lett.* **92**, 035301.

Kozik, E. & Svistunov, B. 2005 Scale-separation scheme for simulating superfluid turbulence: Kelvin-wave cascade. *Phys. Rev. Lett.* **94**, 025301.

Kozik, E. & Svistunov, B. 2008*a* Kolmogorov and kelvin-wave cascades of superfluid turbulence at $t = 0$: What lies between. *Phys. Rev. B* **77**, 060502.

Kozik, E. & Svistunov, B. 2008*b* Scanning superfluid-turbulence cascade by its low-temperature cutoff. *Phys. Rev. Lett.* **100**, 195302.

Kozik, E. V. & Svistunov, B. V. 2009 Theory of decay of superfluid turbulence inthelow-temperature limit. *Journal of Low Temperature Physics* **156** (3), 215–267.

Kursa, M., Bajer, K. & Lipniacki, T. 2011 Cascade of vortex loops initiated by a single reconnection of quantum vortices. *Phys. Rev. B* **83**, 014515.

La Mantia, M., Chagovets, T. V., Rotter, M. & Skrbek, L. 2012 Testing the performance of a cryogenic visualization system on thermal counterflow by using hydrogen and deuterium solid tracers. *Review of Scientific Instruments* **83** (5).

La Mantia, M., Duda, D., Rotter, M. & Skrbek, L. 2013 Lagrangian accelerations of particles in superfluid turbulence. *Journal of Fluid Mechanics* **717**, R9 (11 pages).

La Mantia, M. & Skrbek, L. 2014 Quantum turbulence visualized by particle dynamics. *Phys. Rev. B* **90**, 014519.

Lamb, H. 1945 *Hydrodynamics*. Dover Publications.

Landau, L. D. 1941 *J. Phys. USSR* **5**, 71.

Leadbeater, M., Winiecki, T., Samuels, D. C., Barenghi, C. F. & Adams, C. S. 2001 Sound emission due to superfluid vortex reconnections. *Phys. Rev. Lett.* **86**, 1410–1413.

Leonard, A. 1980 *Journal of Computational Physics* **37**, 289.

Li, Y., Perlman, E., Wan, M., Yang, Y., Meneveau, C., Burns, R., Chen, S., Szalay, A. & Eyink, G. 2008*a* A public turbulence database cluster and applications to study lagrangian evolution of velocity increments in turbulence. http://turbulence.pha.jhu.edu, accessed: November 2013.

Li, Y., Perlman, E., Wan, M., Yang, Y., Meneveau, C., Burns, R., Chen, S., Szalay, A. & Eyink, G. 2008*b* A public turbulence database cluster and applications to study lagrangian evolution of velocity increments in turbulence. *Journal of Turbulence* **9**, N31.

L'vov, V. S., Nazarenko, S. V. & Rudenko, O. 2007 Bottleneck crossover between classical and quantum superfluid turbulence. *Phys. Rev. B* **76**, 024520.

Lvov, V., Nazarenko, S. & Skrbek, L. 2006 Energy spectra of developed turbulence in helium superfluids. *Journal of Low Temperature Physics* **145** (1-4), 125–142.

Malik, N. A. & Vassilicos, J. C. 1999 A lagrangian model for turbulent dispersion with turbulent-like flow structure: Comparison with direct numerical simulation for two-particle statistics. *Physics of Fluids* **11** (6), 1572–1580.

Maurer, J. & Tabeling, P. 1998 Local investigation of superfluid turbulence. *EPL (Europhysics Letters)* **43** (1), 29.

Melotte, D. J. & Barenghi, C. F. 1998 Transition to Normal Fluid Turbulence in Helium II. *Phys. Rev. Lett.* **80**, 4181–4184.

Monaghan, J. J. 1992 Smoothed particle hydrodynamics. *Annual Review of Astronomy and Astrophysics* **30**, 543–574.

Morris, K., Koplik, J. & Rouson, D. W. I. 2008 Vortex locking in direct numerical simulations of quantum turbulence. *Phys. Rev. Lett.* **101**, 015301.

Navier, C. L. M. H. 1822 *Mem. Acad. Sci. Inst. France* **6** (389).

Nazarenko, S. 2011 *Wave Turbulence*. Heidelberg ; New York : Springer Verlag.

Nemirovskii, S. K. 2008 Kinetics of a network of vortex loops in He II and a theory of superfluid turbulence. *Phys. Rev. B* **77**, 214509.

Nemirovskii, S. K., Tsubota, M. & Araki, T. 2002 Energy Spectrum of the Random Velocity Field Induced by a Gaussian Vortex Tangle in He II. *Journal of Low Temperature Physics* **126** (5-6), 1535–1540.

Nore, C., Abid, M. & Brachet, M. E. 1997 Kolmogorov turbulence in low-temperature superflows. *Phys. Rev. Lett.* **78**, 3896–3899.

Ohkitani, K. 2002 Numerical study of comparison of vorticity and passive vectors in turbulence and inviscid flows. *Phys. Rev. E* **65**, 046304.

Onsager, L. 1948 Unpublished: Remark given at the Low Temperature Physics conference at Shelter Island.

Osborne, D. R., Vassilicos, J. C., Sung, K. & Haigh, J. D. 2006 Fundamentals of pair diffusion in kinematic simulations of turbulence. *Phys. Rev. E* **74**, 036309.

Packard, R. E. 1972 Pulsar Speedups Related to Metastability of the Superfluid Neutron-Star Core. *Physical Review Letters* **28**, 1080–1082.

Paoletti, M., Fisher, M. E. & Lathrop, D. 2010 Reconnection dynamics for quantized vortices. *Physica D: Nonlinear Phenomena* **239** (14), 1367 – 1377, at the boundaries of nonlinear physics, fluid mechanics and turbulence: where do we stand? Special issue in celebration of the 60th birthday of K.R. Sreenivasan.

Paoletti, M. S. & Lathrop, D. P. 2011 Quantum turbulence. *Annual Review of Condensed Matter Physics* **2** (1), 213–234.

Richardson, L. 1922 *Weather Prediction by Numerical Process*. Cambridge University Press.

Roche, P.-E. 2012 Private communication.

Roche, P.-E. & Barenghi, C. F. 2008 Vortex spectrum in superfluid turbulence: Interpretation of a recent experiment. *EPL (Europhysics Letters)* **81** (3), 36002.

Roche, P.-E., Diribarne, P., Didelot, T., Franais, O., Rousseau, L. & Willaime, H. 2007 Vortex density spectrum of quantum turbulence. *EPL (Europhysics Letters)* **77** (6), 66002.

Saffman, P. G. 1970 The velocity of viscous vortex rings. *Studies in Applied Mathematics* **49** (4), 371–380.

Saffman, P. G. 1993 *Vortex Dynamics*. Cambridge University Press, cambridge Books Online.

Saint-Michel, B., Herbert, E., Salort, J., Baudet, C., Bon Mardion, M., Bonnay, P., Bourgoin, M., Castaing, B., Chevillard, L., Daviaud, F., Diribarne, P., Dubrulle, B., Gagne, Y., Gibert, M., Girard, A., Hbral, B., Lehner, T.,

Rousset, B. & Collaboration, S. 2014 Probing quantum and classical turbulence analogy in von karman liquid helium, nitrogen, and water experiments. *Physics of Fluids* **26** (12).

Salort, J., Baudet, C., Castaing, B., Chabaud, B., Daviaud, F., Didelot, T., Diribarne, P., Dubrulle, B., Gagne, Y., Gauthier, F., Girard, A., Habral, B., Rousset, B., Thibault, P. & Roche, P.-E. 2010 Turbulent velocity spectra in superfluid flows. *Physics of Fluids (1994-present)* **22** (12), –.

Samuels, D. C. 1993 Response of superfluid vortex filaments to concentrated normal-fluid vorticity. *Phys. Rev. B* **47**, 1107–1110.

Sasa, N., Kano, T., Machida, M., L'vov, V. S., Rudenko, O. & Tsubota, M. 2011 Energy spectra of quantum turbulence: Large-scale simulation and modeling. *Phys. Rev. B* **84**, 054525.

Schwarz, K. & Smith, C. 1981 Pulsed-ion study of ultrasonically generated turbulence in superfluid 4he. *Physics Letters A* **82** (5), 251 – 254.

Schwarz, K. W. 1985 Three-dimensional vortex dynamics in superfluid $^4$He: Line-line and line-boundary interactions. *Phys. Rev. B* **31**, 5782–5804.

Schwarz, K. W. 1988 Three-dimensional vortex dynamics in superfluid $^4$He: Homogeneous superfluid turbulence. *Phys. Rev. B* **38**, 2398–2417.

Sherwin-Robson, L. K., Barenghi, C. F. & Baggaley, A. W. 2015 Local and nonlocal dynamics in superfluid turbulence. *Phys. Rev. B* **91**, 104517.

Skrbek, L., Niemela, J. J. & Donnelly, R. J. 2000 Four Regimes of Decaying Grid Turbulence in a Finite Channel. *Physical Review Letters* **85**, 2973–2976.

Skrbek, L. & Sreenivasan, K. R. 2012 Developed quantum turbulence and its decaya). *Physics of Fluids (1994-present)* **24** (1), –.

Smith, M. R., Donnelly, R. J., Goldenfeld, N. & Vinen, W. F. 1993 Decay of vorticity in homogeneous turbulence. *Phys. Rev. Lett.* **71**, 2583–2586.

Springel, V., White, S. D. M., Jenkins, A., Frenk, C. S., Yoshida, N., Gao, L., Navarro, J., Thacker, R., Croton, D., Helly, J., Peacock, J. A., Cole, S., Thomas, P., Couchman, H., Evrard, A., Colberg, J. & Pearce, F. 2005 Simulations of the formation, evolution and clustering of galaxies and quasars. *Nature* **435** (7042), 629–636.

Stalp, S. R., Skrbek, L. & Donnelly, R. J. 1999 Decay of grid turbulence in a finite channel. *Phys. Rev. Lett.* **82**, 4831–4834.

Stokes, G. G. 1845 On the theories of the internal friction of fluids in motion, and of the equilibrium and motion of elastic solids. *Trans. Cambridge Philos. Soc.* **8**, 287–305.

Tebbs, R., Youd, A. J. & Barenghi, C. F. 2011 The approach to vortex reconnection. *Journal of Low Temperature Physics* **162** (3), 314–321.

Tisza, L. 1938 Transport Phenomena in Helium II. *Nature* **141**, 913.

Tough, J. 1982 Chapter 3: Superfluid turbulence*. *Progress in Low Temperature Physics*, vol. 8, pp. 133 – 219. Elsevier.

Tsubota, M. & Adachi, H. 2011 Simulation of counterflow turbulence byvortex filaments. *Journal of Low Temperature Physics* **162** (3-4), 367–374.

Tsubota, M., Barenghi, C. F., Araki, T. & Mitani, A. 2004 Instability of vortex array and transitions to turbulence in rotating helium II. *Phys. Rev. B* **69**, 134515.

Tsubota, M. & Halperin, W., ed. 2009 *Progress in Low Temperature Physics*, vol. 16. Elsevier.

Vinen, W. & Niemela, J. 2002 Quantum turbulence. *Journal of Low Temperature Physics* **128** (5-6), 167–231.

Vinen, W. F. 1957*a* Mutual Friction in a Heat Current in Liquid Helium II. I. Experiments on Steady Heat Currents. *Proceedings of the Royal Society of London A: Mathematical, Physical and Engineering Sciences* **240** (1220), 114–127.

Vinen, W. F. 1957*b* Mutual Friction in a Heat Current in Liquid Helium II. II. Experiments on Transient Effects. *Proceedings of the Royal Society of London A: Mathematical, Physical and Engineering Sciences* **240** (1220), 128–143.

Vinen, W. F. 1957*c* Mutual Friction in a Heat Current in Liquid Helium II. III. Theory of the Mutual Friction. *Proceedings of the Royal Society of London A: Mathematical, Physical and Engineering Sciences* **242** (1231), 493–515.

Vinen, W. F. 1958 Mutual Friction in a Heat Current in Liquid Helium II. IV. Critical Heat Currents in Wide Channels. *Proceedings of the Royal Society of London A: Mathematical, Physical and Engineering Sciences* **243** (1234), 400–413.

Vinen, W. F. 1961 The Detection of Single Quanta of Circulation in Liquid Helium II. *Proceedings of the Royal Society of London A: Mathematical, Physical and Engineering Sciences* **260** (1301), 218–236.

Vinen, W. F. 2006 An introduction to quantum turbulence. *Journal of Low Temperature Physics* **145** (1), 7–24.

Volovik, G. 2004 On developed superfluid turbulence. *Journal of Low Temperature Physics* **136** (5-6), 309–327.

Walmsley, P. M. & Golov, A. I. 2008 Quantum and quasiclassical types of superfluid turbulence. *Phys. Rev. Lett.* **100**, 245301.

Walstrom, P., II, J. W., Maddocks, J. & Sciver, S. V. 1988 Turbulent flow pressure drop in various He {II} transfer system components. *Cryogenics* **28** (2), 101 – 109.

Yui, S. & Tsubota, M. 2014 Counterflow quantum turbulence in a square channel under the normal fluid with a poiseuille flow. *Journal of Physics: Conference Series* **568** (1), 012028.

Zhang, T., Celik, D. & Van Sciver, S. W. 2004 Tracer particles for application to piv studies of liquid helium. *Journal of Low Temperature Physics* **134** (3), 985–1000.

Zhang, T. & Van Sciver, S. W. 2005*a* Large-scale turbulent flow around a cylinder in counterflow superfluid4He (He (II)). *Nat Phys* **1** (1), 36–38.

Zhang, T. & Van Sciver, W. S. 2005*b* The motion of micron-sized particles in He II counterflow as observed by the PIV technique. *Journal of Low Temperature Physics* **138** (3), 865–870.

Zmeev, D. E., Walmsley, P. M., Golov, A. I., McClintock, P. V. E., Fisher, S. N. & Vinen, W. F. 2015 Dissipation of quasiclassical turbulence in superfluid $^4$He. *Phys. Rev. Lett.* **115**, 155303.